# Computation of Higher-Order Hydrodynamic Forces on Ships and Offshore Structures in Waves

by

Yonghwan Kim

BS in Naval Architecture and Marine Engineering, Seoul National University, 1987
MS in Naval Architecture and Marine Engineering, Seoul National University, 1989

Submitted to the Department of Ocean Engineering
in partial fulfillment of the requirements for the degree of

Doctor of Philosophy in Hydrodynamics

at the

MASSACHUSETTS INSTITUTE OF TECHNOLOGY

February 1999



Author .....
Department of Ocean Engineering
October, 1998

Certified by .....
Paul D. Sclavounos
Professor of Naval Architecture
Thesis Supervisor

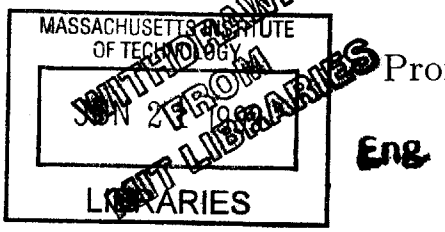


Eng.

Accepted by .....
J. Kim Vandiver
Chairman, Departmental Committee on Graduate Students

# Computation of Higher-Order Hydrodynamic Forces on Ships and Offshore Structures in Waves

by

Yonghwan Kim

Submitted to the Department of Ocean Engineering
on October, 1998, in partial fulfillment of the
requirements for the degree of
Doctor of Philosophy in Hydrodynamics

## Abstract

This thesis concentrates on the computation of hydrodynamic forces on ships and offshore structures. The specific topic of this thesis is the higher-order forces and moment. This thesis consists of two parts.

The aim of the first part is the development of a finite-depth unified theory for ship motions and its extension to the computation of the second-order mean-drift forces and moment. The mathematical background of the finite-depth unified theory is introduced, and an associated computer program is developed to verify this theory. The accuracy is checked from the comparison with the result of a three-dimensional panel code, and the nice agreement is shown. The theory is extended to the computation of the second-order quantities. The mean forces and moment are computed using the far-field formulae, and the wave drift damping matrix is obtained by Aranha's formula. Based on the present study, slender-body theory is shown to be a useful design tool for a floating ship, like an FPSO.

The second part develops a model and a corresponding computational program for the prediction of nonlinear wave effects. The primary interest is the second-order high-frequency effect which induces flexural body responses. The Rankine panel method using the bi-quadratic B-spline basis function is adopted as a method of solution. The theoretical aspects of the numerical scheme are described to verify the consistency and stability of the method, and a thorough parametric study is carried out. The computational result includes linear and nonlinear run-up and wave loads up to the second order. Based in this numerical method, the sum-frequency wave loads are obtained for a monochromatic wave and multi-frequency waves. Good agreement is shown with existing numerical and experimental data.

Thesis Supervisor: Paul D. Sclavounos
Title: Professor of Naval Architecture

# Acknowledgements

I would like to gratitude to everyone who supported my studies. First of all, my deep appreciation must be directed to Prof. Sclavounos. I am always impressed by his sharpness and professional excellence. I have been blessed by the opportunity to study under his support. I am also greatly thankful to Prof. Yue and Prof. Makris, who served on my thesis committee and gave me good advice and fresh ideas.

This thesis is dedicated to my family. During almost two decades, my wife, Soo-jeong, has been always on my side with love. She is the only woman in my life, and her unconditional support led me up to this point. Soyeon and Ryan are my future. Their existence gave me strength when I was tired. I have an unpayable debt to my mother. Her sacrifice to my life cannot be more than anyone else, and it is always in my mind.

I wish to thank all crews of our laboratory and the faculty of department. I cannot forget the help and friendship of Dave, Yifeng, Alex, ..... . I hope they and their family have good luck and happiness in their lives. I also deeply appreciate Dr. Lee, C.H., who gave me advice in many respect. Also I will not forget the time spent with Korean 'gang'.

I acknowledge the financial support provided by Amoco, Aker, Conoco, DnV, Exxon, Norsk Hydro, Saga, Statoil, and ONR.

# Contents

# List of Figures

# PART I

# SLENDER-BODY THEORY

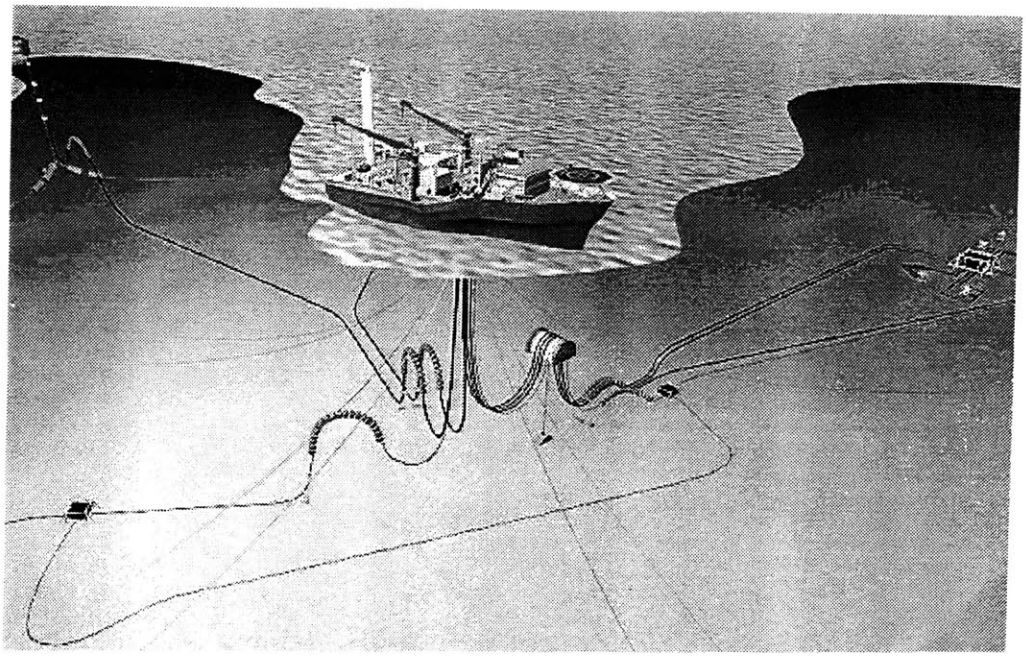

# Chapter 1

# Introduction

During the last decade, most studies in marine hydrodynamics are based on numerical methods and the complete three-dimensional problems have been of interest. From today's point of view, slender-body theory may be too simplified or too mathematical to be used as a design tool. However, it cannot be overlooked that strip theory has been the most popular tool for the analysis of seakeeping performance over past two decades. The reason of this popularity is partly its reasonable accuracy. In spite of the fact that strip theory is a low-order theory, its accuracy is quite reasonable for the linear seakeeping analysis. Furthermore unified theory provides better accuracy comparable with three-dimensional method. More significant merit is its computing effort. A unified theory code supplies almost instant answer using very little memory. An another important but hidden reason is the simplicity of input data, in particular the treatment of the hull form. Slender-body theory requires the offset data on ship sections, so called, stations.

Recently second-order quantities have become important in the design of FPSO (floating production, storage, offloading ship) or shuttle tanker. One of the important issues in the design of these vessels is the slow drift motion, which is related to the design of a dynamic positioning system and/or mooring lines. Strip theory has been used to compute the added resistance which is a second-order quantity, but it doesn't provide accurate results for such quantities. Since the second-order quantities are very

sensitive to the accuracy of the linear solution, a method more accurate than strip theory is required even for the linear problem. In this sense, the three-dimensional panel code, like WAMIT or SWAN, is desirable for the computation of second-order quantities.

Unified theory bridges the gap between strip theory and a three-dimensional panel method. Unified theory has an advantage that sectional offset data are sufficient for the representation of the hull geometry. Furthermore the accuracy of unified theory is comparable with that of the three-dimensional method since it introduces a three-dimensional correction to strip theory. In addition the computation code requires much less CPU time than any three-dimensional panel code. Therefore unified theory may be an effective design tool which has all the advantages of strip theory and of a three-dimensional panel code.

The most pioneering work for ship motion using slender-body theory was done by Korvin-Kroukovsky and Jacobs [40]. Their method is based on the assumption of a long slender body and short waves, not taking into account the interaction between sections. Correcting Timman-Newman relation in their method, many refinements were introduced. The most popular strip theory may be the method used by Faltinsen, Tuck and Salvesen in 1970. A further development from strip theory was done by Newman [54] and Sclavounos [64] who gave an excellent exposition of the state of the art in this field. They presented a theoretical foundation perturbing from the strip theory approach, to extend the region of whole frequencies.

There are not many studies of the finite-depth seakeeping problem. Even though the shallow-depth effect on two-dimensional sections has been studied many times, few applications of the finite-depth strip theory exist. Kim [26] has shown the result of the finite-depth strip theory, and Tuck [75] introduced a theory which assumes that the depth is shallow and the wavelength is comparable with the ship length. Borresen [6] has tried to extend unified theory to finite depth when the ship has forward speed. He derived the far- and near-field solutions of the velocity potential, and an integral equation was proposed. However, he didn't show any meaningful results since the

kernel of his integral equation involves double-integral terms which are difficult to compute.

The present study is on the line of Borresen's work, in particular for a zero-speed case. When there is no forward speed, the kernel of the integral equation can be simplified using a contour integral, and it can be written as a series form that makes the integral equation easy to solve. Unified theory is based on the matched asymptotic expansion method, and an integral equation is derived from matching the inner expansion of the far-field solution with the outer expansion of the near-field solution. Solving the integral equation, both the far- and near-field solutions can be completed. The present work introduces the far- and near-field behavior of the velocity potential around a slender ship in finite depth, and a new kernel is derived for the motion of the body with no forward speed.

Based on the present theory, a computer code has been developed for the heave and pitch motion of a slender ship. Since the solution of strip theory is necessary for unified theory, a strip theory code must be developed first. In the present study, NIIRID [68], a computer code developed for two-dimensional sections, was used for the strip theory code, and it was extended to the finite-depth problem. The series form is used for the two-dimensional finite-depth Green function. The unified theory code for the heave and pitch motions is extended from this strip theory code. Using the strip theory solution, the three-dimensional corrections are computed by solving the integral equations of unified theory. Numerical computations were carried out for a few typical slender ships. The hydrodynamic coefficients and motion RAOs are compared with WAMIT for validation.

The present study is extended to the computation of the second-order quantities. Since the accuracy of unified theory is comparable with that of three-dimensional panel method, the computation of the second-order mean forces and moment was carried out using the linear solution in unified theory. The accuracy of these quantities depends on the accuracy of Kochin function, i.e. the velocity potential and the motion RAOs. For the deep water problem, Kim & Sclavounos [33] applied the deep-water

unified theory (heave, pitch) and strip theory(sway, roll, yaw) to the computation of second-order quantities, and they showed a favorable agreement with WAMIT. The present study introduces the results for finite depth.

This study includes the wave drift damping for infinite depth. Aranha [2] suggested a formula for the wave drift damping coefficients in surge and sway. More recently he extended his formula to the yaw-motion component [3]. Although there is some doubt about its accuracy, particularly in the radiation problem, his formula has an advantage that it requires just the drift forces at zero speed. Computations were carried out for a mathematical hull, Ship1, which Finne and Grue [19] considered. The damping coefficients with Aranha's formula are compared with the result of the three-dimensional panel method obtained by Finne and Grue.

This part consists of five chapters including this introduction. In chapter 2 the boundary value problem is formulated with the fundamental assumptions. The theoretical approach of the boundary value problem is described in chapter 3. In the far field, the velocity potential is written as the line distribution of a three-dimensional wave sources, while the near-field solution can be obtained by solving the two-dimensional boundary value problem formulated using the slender-body assumption. From matching two solutions, a new integral equation is derived. In chapter 4, the formulae for the second-order quantities are summarized. Using the linear solutions, the mean-drift forces and moment can be obtained using far-field formulae. The wave drift damping coefficients are also computed using the mean forces and moment at zero speed, and Aranha's formula is applied. The computational results based on the present theory are introduced in chapter 5. The hydrodynamic forces, motion RAOs and second-order quantities are computed for a few typical slender ships and the results are compared with WAMIT and other existing data.

# Chapter 2

# Boundary Value Problem

Consider a Cartesian coordinate system fixed in space with the free surface taken at $z = 0$. As shown in Figure 2-1, the center-plane of the ship is at $y = 0$ and the positive $x$ axis points towards the bow. Assume that the ship undergoes small harmonic oscillatory motions in a monochromatic linear wave with frequency $\omega$.

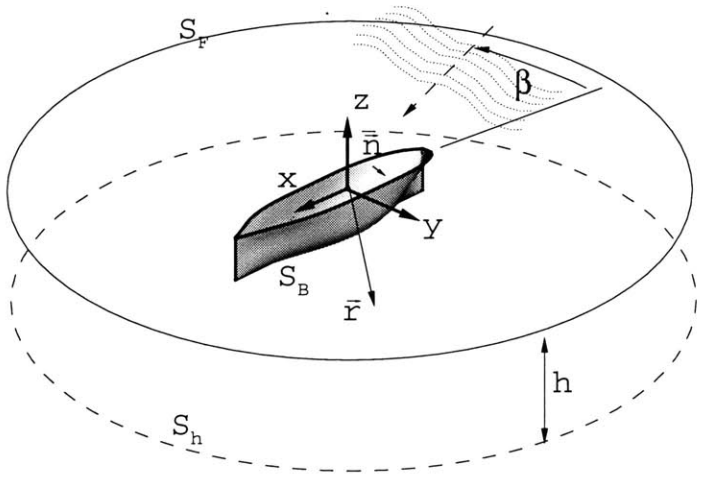


Figure 2-1: Coordinate System

If an ideal fluid and the irrotational flow are assumed, using complex notation,

the linear velocity potential, $\Phi$, is defined by

$$\Phi(x,y,z,t) = \Re\{\phi(x,y,z)e^{i\omega t}\} \tag{2.1}$$

where

$$\phi(x,y,z) = \Re\{\phi_I + \phi_7 + \sum_{j=1}^{6} \xi_j \phi_j(x,y,z)\}. \tag{2.2}$$

The subscript $j$ means the direction of motion, and $\xi_j$ is the complex motion amplitude. $j = 1,2,3$ and $j = 4,5,6$ correspond to the translational and rotational motions. $\phi_7$ denotes the diffraction potential and $\phi_I$ is the incident wave potential given by

$$\phi_I = \frac{igA}{\omega} \frac{\cosh\{k(z+h)\}}{\cosh kh} e^{-ik(x\cos\beta + y\sin\beta)}. \tag{2.3}$$

$A$ is the wave amplitude and $\beta$ is the angle of the incident wave, with $\beta = 180^o$ for head waves. $k$ is the wave number.

The linearized boundary value problem for $\phi_j(x,y,z)$ can be written as follows :

- Fluid domain,

$$\nabla^2 \phi_j = 0 \tag{2.4}$$

- Free surface, $S_F(z=0)$,

$$\frac{\partial \phi_j}{\partial z} - \frac{\omega^2}{g}\phi_j = 0 \tag{2.5}$$

- Body surface, $S_B$,

$$\vec{n} \cdot \nabla \phi_j = \begin{cases} i\omega n_j & j = 1...6 \\ -\vec{n} \cdot \nabla \phi_I & j = 7 \end{cases} \tag{2.6}$$

- Bottom surface, $S_h(z = -h)$,

$$\frac{\partial \phi_j}{\partial z} = 0 \tag{2.7}$$

$\vec{n} = (n_1, n_2, n_3)$ is the unit normal vector pointing inside the body surface with $n_5 = -xn_3 + zn_1$. This boundary value problem requires an additional radiation condition to become well posed.

In the present study, unified theory for the heave and pitch motions are considered.

# Chapter 3

# A Finite-Depth Unified Theory

Unified theory is based on the matched asymptotic expansion method. Two distinct solutions at the far and near field around a ship are described in the following sections. Their inner and outer expansions are major interests in order to match two solutions in the overlapping zone. The two leading terms are considered in the inner and outer expansions. The first term is a strip theory contribution, and the other term is a three-dimensional correction. The matching conditions produce an integral equation, which is a key of unified theory. In order to develop the present theory, the ship is assumed slender so that the longitudinal flow gradient near the ship hull can be assumed to be much smaller than the transverse flow gradients.

## 3.1 The Far-Field Solution

The velocity potential doesn't feel the detailed body shape in the far field, located at a radial distance comparable to or greater than the ship length. If a body is slender, the velocity potential can be expressed as a line distribution of three-dimensional finite-depth wave sources,

$$\phi_j(x,y,z) = \int_L d\xi \; q_j(\xi) G(\xi - x, y, z) \tag{3.1}$$

where $q_j(\xi)$ is the strength of the Green function, $G(x,y,z)$. Using the convolution theorem, $\phi_j(x,y,z)$, can be rewritten in the Fourier domain as

$$\phi_j(x,y,z) = \frac{1}{2\pi}\int_{-\infty}^{\infty} du\ e^{iux} q^*(u) G^*(u;y,z). \tag{3.2}$$

The superscript $*$ denotes the Fourier transformation.

$G^*(u;y,z)$ can be obtained by solving the boundary value problem for a line distribution of wave Green functions, and the details are described in Appendix A. $G^*(u;y,z)$ is written as follows :

$$\begin{aligned} G^*(u;y,z) &= -\frac{1}{2\pi}\int_{-\infty}^{\infty} dv\ e^{ivy} \times \\ &\quad \frac{1}{\cosh\{\sqrt{u^2+v^2}h\}} \frac{\cosh\{\sqrt{u^2+v^2}(z+h)\}}{[\sqrt{u^2+v^2}\tanh\{\sqrt{u^2+v^2}h\} - \nu]} \end{aligned} \tag{3.3}$$

where $\nu = \omega^2/g$.

Equation (3.3) recovers the result of Ogilvie and Tuck [58] when $h \to \infty$,

$$G^*(u;y,z) \to -\frac{1}{2\pi}\int_{-\infty}^{\infty} dv e^{ivy} \frac{e^{\sqrt{u^2+v^2}z}}{\sqrt{u^2+v^2}-\nu}. \tag{3.4}$$

Let's define a Fourier-transformed function, $f^*(u;y,z)$, such that

$$f^*(u;y,z) = G^*(u;y,z) - G^*(0;y,z) \tag{3.5}$$

Notice that $G^*(0;y,z) = G_{2D}(y,z)$ where $G_{2D}(y,z)$ is the two-dimensional Green function which satisfies the linearized free-surface boundary condition and the radiation condition. Then the velocity potential can be rewritten as

$$\phi_j(x,y,z) = G_{2D}(y,z)q_j(x) + \int_L q_j(\xi) f(\xi - x, y, z) d\xi. \tag{3.6}$$

The adoption of $f(x,y,z)$ leads the decomposition of the far-field solution with two terms, two-dimensional and three-dimensional contributions. As mentioned later,

the near-field solution is supposed to be written as the same form.

Now consider the inner expansion of the far-field solution. The inner expansion can be obtained using the Taylor series expansion of the integral term in equation (3.6) for small $y$ and $z$. The Taylor series expansion is applicable when a function is not singular at its expansion point. In this case, the expansion is applied to the integral. The integral of $f(\xi - x, y, z)$ doesn't have a singularity at $(\xi - x, y, z) = (0, 0, 0)$, and the details are explained in Appendix B. Then, the inner expansion is written as

$$\begin{aligned}\phi_j(x,y,z) &= q_j(x)G_{2D}(y,z) + \int_L q_j(\xi)f(\xi - x, 0, 0)d\xi \\ &\quad + y\frac{\partial}{\partial y}\int_L q_j(\xi)f(\xi - x, y, z)d\xi|_{y=z=0} \\ &\quad + z\frac{\partial}{\partial z}\int_L q_j(\xi)f(\xi - x, y, z)d\xi|_{y=z=0} + O(y^2, z^2) \end{aligned} \tag{3.7}$$

For the heave and pitch motion, the second integral term vanishes because of symmetry. The third integral term remains as long as $z$ is not zero.

## 3.2 The Near-Field Solution

At transverse distances of the order of the ship beam, the details of the ship geometry should be considered. In particular the relative orders of the flow gradients are dictated by the relative orders of the body surface gradients. If the body is slender for the $y$ and $z$ coordinates to be of $O(\epsilon)$, the gradients in the longitudinal and transverse directions can be written as

$$\frac{\partial}{\partial x} = O(1) \ << \ \frac{\partial}{\partial y}, \frac{\partial}{\partial z} = O(\frac{1}{\epsilon}). \tag{3.8}$$

Then the boundary value problem is reduced to the two-dimensional problem at a certain section of the body.

Notice that the body boundary condition is pure imaginary. If there is a term which is pure real and satisfied with other conditions, it will be a homogeneous

solution. Then the general solution of the near field consists of a particular solution $\phi_P$ and a homogeneous solution $\phi_H$,

$$\phi_j(x,y,z) = \phi_{j,P}(x,y,z) + C_j(x)\phi_{j,H}(x,y,z) \tag{3.9}$$

$C_j(x)$ is an arbitrary function of $x$ which will be determined from the matching with the inner expansion of the far-field solution. The particular solution is the strip theory solution, say $\psi_j(x,y,z)$ which satisfies the pure imaginary body boundary condition. The homogeneous solution can be regarded as a free wave potential which is a pure real potential, and $\psi_j(x,y,z) + \bar{\psi}_j(x,y,z)$ can be a homogeneous solution where $\bar{\psi}_j$ is the complex conjugate of $\psi_j$. Thus we can rewrite as

$$\phi_j(x,y,z) = \{1 + C_j(x)\}\psi_j(x,y,z) + C_j(x)\bar{\psi}_j(x,y,z) \tag{3.10}$$

The outer expansion of this solution is of interest in order to match with the inner expansion of the far-field solution. At a large distance from the body, the particular solution has a point-source behavior. Then it can be written as

$$\psi_j(x,y,z) = \sigma_j(x)G_{2D}(y,z) \tag{3.11}$$

where $\sigma_j(x)$ is the strength of the two-dimensional wave source, $G_{2D}$, placed at the center of the section. Therefore the outer expansion of the near-field solution is written as

$$\begin{aligned} \phi_j(x,y,z) &= [\sigma_j(x) + C_j(x)\{\sigma_j(x) + \bar{\sigma}_j(x)\}]G_{2D}(y,z) \\ &\quad - C_j(x)\bar{\sigma}(x)(G_{2D}(y,z) - \bar{G}_{2D}(y,z)) \end{aligned} \tag{3.12}$$

with

$$G_{2D}(y,z) - \bar{G}_{2D}(y,z) = -2i\ Im(G_{2D})$$

$$= 2i \frac{\cosh\{m_o(z+h)\}}{\cosh(m_o h)} \frac{m_o h}{\nu h + (\frac{m_o h}{\cosh(m_o h)})^2} \cos(m_o y) + O(\frac{1}{y}) \tag{3.13}$$

and $m_o = k$, such that

$$\nu = m_o \tanh(m_o h) \tag{3.14}$$

$G_{2D} - \bar{G}_{2D}$ contains the three-dimensional effects in the near-field solution. The physical description of this term is a free wave contribution. When $y$ becomes large, the local waves decay exponentially. In consequence the free wave contribution is dominant in $G_{2D} - \bar{G}_{2D}$. Newman [54] showed the deep water case,

$$G_{2D}(y,z) - \bar{G}_{2D}(y,z) \rightarrow 2i(1+\nu z)\cos(\nu y) \tag{3.15}$$

when $h \rightarrow \infty$. This limit case is proven using

$$\frac{\cosh\{m_o(z+h)\}}{\cosh(m_o h)} \rightarrow e^{m_o z} = 1 + m_o z + (m_o z)^2 + ... \tag{3.16}$$

$$\frac{1}{\nu h + (\frac{m_o h}{\cosh(m_o h)})^2} \rightarrow \frac{1}{\nu h} \tag{3.17}$$

and $\nu = m_o$.

## 3.3 Matching Conditions

At a transverse distance greater than the body beam but less than the body length, the inner expansion of the far-field solution should be the same with the outer expansion of the inner-field solution.

Both equations (3.7) and (3.12) are decomposed with two terms, and the comparison of each term leads two matching conditions. However, unfortunately, both equations include the $z$-coordinate. In order to circumvent the difficulty of treating

the $z$-coordinate terms, consider the matching conditions at $z = 0$. That is to say, matching can be carried out on $z = 0$ and extended to $z < 0$ by analytic continuation.

If the far- and near-field solutions should be the same, the coefficients of the two-dimensional Green function should be the same,

$$q_j(x) = \sigma_j(x) + C_j(x)\{\sigma_j(x) + \bar{\sigma}_j(x)\}. \tag{3.18}$$

The same applies to the three-dimensional correction terms,

$$\begin{aligned} F(q_j) &\equiv \int_L q_j(\xi) f(\xi - x, 0, 0) d\xi \\ &= -2iC_j(x)\bar{\sigma}(x) \frac{m_o h}{\nu h + (\frac{m_o h}{\cosh(m_o h)})^2}. \end{aligned} \tag{3.19}$$

The unknown parameter in the far-field solution is $q_j(x)$, while $C_j(x)$ is unknown in the near field. Therefore the above two equations will supply the solutions of the two unknown parameters. The elimination of $C_j(x)$ from the above equations leads to the integral equation for $q_j(x)$,

$$q_j(x) + \frac{\nu h + (\frac{m_o h}{\cosh(m_o h)})^2}{2im_o h}\{1 + \frac{\sigma_j(x)}{\bar{\sigma}_j(x)}\}F(q_j) = \sigma_j(x). \tag{3.20}$$

The solution of the integral equation determines the far-field solution and also the complete near-field solution in the form

$$\phi_j(x, y, z) = \psi_j(x, y, z) + \frac{q_j(x) - \sigma_j(x)}{\sigma_j(x) + \bar{\sigma}_j(x)}\{\psi_j(x, y, z) + \bar{\psi}_j(x, y, z)\}. \tag{3.21}$$

Equation (3.20) has to approach the deep water case when $h \to \infty$,

$$q_j(x) - \frac{1}{2\pi i}(\frac{\sigma}{\bar{\sigma}} + 1)L(q_j) = \sigma_j(x) \tag{3.22}$$

where

$$L(q) = q(x)\ (\gamma + i\pi) + \int_L d\xi\ \{\ \frac{1}{2} sgn(x-\xi)\ ln(2\nu|x-\xi|)\ \frac{d}{d\xi} q(\xi) - \frac{\pi\nu}{4}\ K[\nu(x-\xi)]\ q(\xi)\ \} \tag{3.23}$$

and

$$K(x) = Y_o(|x|) + 2iJ_o(|x|) + H_o(|x|) \tag{3.24}$$

Here, $J_o(x), Y_o(x)$ are Bessel functions of zero-th order and $H_o(x)$ is Struve function of zero-th order. Besides, $\gamma$ is the Euler constant.

$F(q_j)$ must approach $L(q_j)$ as $h \to \infty$. Since equation (3.13) approaches equation (3.15), the limiting case can be proved by observing the kernel.

## 3.4 The Kernel of the Integral Equation

The computation of the kernel is the key in unified theory since the success of solving equation (3.20) depends on the computation of kernel. Borresen obtained the kernel in the Fourier domain in which the double numerical integration has to be carried out. In consequence, the triple numerical integration should be treated to solve this integral equation.

If the ship has no forward speed, a more simple form of the kernel can be derived. Consider the Fourier-transformed kernel,

$$f^*(u;y,z) = -\frac{1}{2\pi}\int_{-\infty}^{\infty} dv\ e^{ivy} \times \left[\frac{\cosh\{\sqrt{u^2+v^2}(z+h)\}}{\cosh\{\sqrt{u^2+v^2}h\}[\sqrt{u^2+v^2}\tanh\{\sqrt{u^2+v^2}h\} - \nu]} - \frac{\cosh\{|v|(z+h)\}}{\cosh(|v|h)[|v|\tanh(|v|h) - \nu]}\right]. \tag{3.25}$$

This equation can be simplified using a contour integral. In a complex $v$-domain,

there are two poles on the $\Re(v)$ axis which contribute to the free wave. The poles on the $Im(v)$ axis contribute to the local waves near a source singularity. When $y = z = 0$,

$$\begin{aligned} f^*(u;0,0) &= i\frac{m_o}{m_o^2 h - \nu^2 h + \nu}\left(\frac{m_o}{\sqrt{m_o^2 - u^2}} - 1\right) \\ &\quad - \sum_{n=1}^{\infty} \frac{m_n}{m_n^2 h + \nu^2 h - \nu}\left(\frac{m_n}{\sqrt{m_n^2 + u^2}} - 1\right) \end{aligned} \tag{3.26}$$

where

$$m_n \tan(m_n h) = -\nu \tag{3.27}$$

which is the dispersion relation of the local waves.

Using

$$\int_{-\infty}^{\infty} du\, e^{-iux} \frac{m}{\sqrt{m^2 - u^2}} = -\pi i Y_o(mx) + \pi J_o(mx) \tag{3.28}$$

$$\int_{-\infty}^{\infty} du\, e^{-iux} \frac{m}{\sqrt{m^2 + u^2}} = -2K_o(mx), \tag{3.29}$$

the kernel in the physical domain is written as

$$\begin{aligned} f(x,0,0) &= \frac{1}{2\pi}\int_{-\infty}^{\infty} f^*(u;0,0)e^{iux}du \\ &= \frac{1}{2}\frac{m_o^2}{m_o^2 h - \nu^2 h + \nu}\{-iY_o(m_o x) + J_o(m_o x) - \frac{2}{m_o}\delta(x)\} \\ &\quad - \sum_{n=1}^{\infty} \frac{m_n^2}{m_n^2 h + \nu^2 h - \nu}\{\frac{1}{\pi}K_o(m_n x) - \frac{1}{m_n}\delta(x)\} \end{aligned} \tag{3.30}$$

where $K_o(x)$ is the modified Bessel function of zero-th order.

Now, the kernel is written in a series form. In fact, this result is consistent with the series forms of the two- and three-dimensional Green functions derived by John [25] and rewritten by Wehausen and Laitone [79].

A detailed investigation on the singularities of the kernel and its integral is re-

quired. When $y$ and $z$ approach zero, the two-dimensional Green function has a logarithmic singularity and the three-dimensional Green function has the logarithmic and $1/r$ singularities. However, these singularities can be integrated. Furthermore the $1/r$ singularity is canceled out with the two-dimensional logarithmic singularity when it is integrated. The details are described in Appendix B.

Figure 3-1 shows the Fourier-transformed kernel, $f^*(u;0,0)$, for finite and infinite depth. When $h \to \infty$, the kernel has to recover the infinite depth case. $f^*(u;0,0)$ of the infinite-depth kernel takes the form :

$$\begin{aligned} \lim_{h\to\infty} f^*(u;0,0) &= ln(\frac{2\nu}{|u|}) + \pi i - \frac{1}{\sqrt{|1-\frac{u^2}{\nu^2}|}} \\ &\quad - \left\{ \begin{array}{ll} i\pi + \cosh^{-1}(\frac{\nu}{|u|}) & \text{if } \nu \geq |u| \\ -\pi + \cos^{-1}(\frac{\nu}{|u|}) & \text{if } \nu < |u| \end{array} \right\} \end{aligned} \tag{3.31}$$

The finite-depth kernel approaches the infinite depth limit as $h$ becomes large.

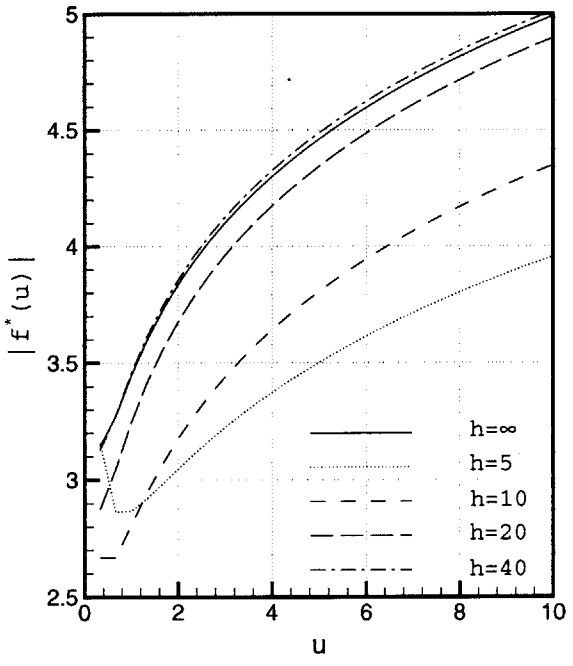


Figure 3-1: Comparison of the finite and infinite depth kernel, $\omega = 1.0$

## 3.5 Hydrodynamic Forces

The added mass $a_{ij}$ and damping coefficient $b_{ij}$ can be obtained from the inner solution by integrating the linearized pressure over the body surface.

$$\omega^2 a_{ij} - i\omega b_{ij} = -i\omega\rho \int\int n_i \phi_j ds \tag{3.32}$$

where $\rho$ is the water density.

Since the near-field solution can be decomposed with two separate terms, it follows that

$$-i\omega\rho \int\int n_i \phi_j ds = H_1 + H_2 \tag{3.33}$$

where

$$H_1 = -i\omega\rho \int\int n_i \psi_j ds \tag{3.34}$$

$$H_2 = -i\omega\rho \int\int n_i C_j(x)(\psi + \bar{\psi}_j) ds \tag{3.35}$$

$H_1$ is the contribution from strip theory, and $H_2$ is the three-dimensional correction due to unified theory. Hence strip theory holds only $H_1$. In the deep water problem, when $\nu \to \infty$, $C_j(x) \to 0$ so that strip theory is recovered. The same is valid for the finite depth case.

The other quantities of interest for the evaluation of ship motions are the wave excitation force and moment. Since the radiation potential is known, the Haskind relation is applicable. Combining the body boundary condition, the near-field Haskind relation is written as

$$X_i = -\rho A \int\int_{S_B} (i\omega n_i \phi_I - \phi_i \frac{\partial \phi_I}{\partial n}) ds. \tag{3.36}$$

Based on the Green's theorem, Sclavounos [67] derived the far-field Haskind relation,

$$X_i = \frac{i\rho g A}{2\omega} \int_L q_j(x) e^{-i\nu x \cos\beta} dx \tag{3.37}$$

According to the study of Kim & Sclavounos [33], the far-field formula provides a more accurate result in slender-body theory.

## 3.6 The Equation of Motion

Assuming that linear surge mode of motion couples weakly with heave and pitch for slender ships, the classical equations of motion follow in the form :

- Coupled Heave-Pitch Equations of Motion

$$\begin{aligned} &[\ -\omega^2(M + a_{33}) + i\omega b_{33} + C_{33}\ ]\xi_3 \quad + \\ &\qquad [\ -\omega^2(M_{35} + a_{35}) + i\omega b_{35} + C_{35}\ ]\xi_5 \ = \ X_3 \end{aligned} \tag{3.38}$$

$$\begin{aligned} &[\ -\omega^2(M_{53} + a_{53}) + i\omega b_{53} + C_{53}\ ]\xi_3 \quad + \\ &\qquad [\ -\omega^2(I_{55} + a_{55}) + i\omega b_{55} + C_{55}\ ]\xi_5 \ = \ X_5 \end{aligned} \tag{3.39}$$

- Coupled Sway-Roll-Yaw Equations of Motion

$$\begin{aligned} &[\ -\omega^2(M + a_{22}) + i\omega b_{22} + C_{22}\ ]\xi_2 \quad + \\ &\quad [\ -\omega^2(M_{24} + a_{24}) + i\omega b_{24} + C_{24}\ ]\xi_4 \quad + \\ &\qquad [\ -\omega^2(M_{26} + a_{26}) + i\omega b_{26} + C_{26}\ ]\xi_6 \ = \ X_2 \end{aligned} \tag{3.40}$$

$$[\ -\omega^2(M + a_{42}) + i\omega b_{42} + C_{42}\ ]\xi_2 \ +$$
$$[\ -\omega^2(I_{44} + a_{44}) + i\omega b_{44} + C_{44}\ ]\xi_4 \ +$$
$$[\ -\omega^2(M_{46} + a_{46}) + i\omega b_{46} + C_{46}\ ]\xi_6 \ = \ X_4 \qquad (3.41)$$

$$[\ -\omega^2(M + a_{62}) + i\omega b_{62} + C_{62}\ ]\xi_2 \ +$$
$$[\ -\omega^2(M_{64} + a_{64}) + i\omega b_{64} + C_{64}\ ]\xi_4 \ +$$
$$[\ -\omega^2(I_{66} + a_{66}) + i\omega b_{66} + C_{66}\ ]\xi_6 \ = \ X_6 \qquad (3.42)$$

$M, I_{ij}$ are the mass and moment of inertia of ship. $C_{ij}$ means the restoring term. $C_{D,eq}$ is an equivalent coefficient of roll viscous damping.

The added masses and damping coefficients for sway, yaw and roll are obtained by strip theory suggested by Salvesen, Tuck and Faltinsen [62]. Also all other quantities which unified theory is not available are computed using their method.

The roll motion is greatly affected by fluid viscosity which has a nonlinear behavior. The state of the art of roll damping mechanisms is described in the report of Himeno [22]. In the present study, the concept of equivalent drag coefficient is applied. The equivalent linear damping can be obtained by preserving the energy loss by viscous effects, and it can be written as

$$C_{D,eq} = \frac{8}{3\pi} C_D \xi_4 \omega \qquad (3.43)$$

where $C_D$ is the quadratic viscous damping coefficient. Note that $C_{D,eq}$ is a function of motion frequency and amplitude. Hence, at a given frequency, an iterative scheme is applied to get the amplitude of roll motion.

# Chapter 4

# Second-Order Quantities

## 4.1 The Mean Drift Forces & Moment

The slow drift forces and responses are important factors for the design of an offshore structure and a floating ship, like an FPSO. The accurate prediction of drift force is essential to design a mooring and/or dynamic positioning system. In the simulation of the slow drift motion, the mean force and moment are the most important quantities. They may be obtained using only the linear solution.

For deep water, the surge and sway mean forces can be obtained by the far-field equations suggested by Maruo [46].

$$\bar{F}_x = \frac{\rho\nu^2}{8\pi}\int_0^{2\pi} |H(\theta)|^2 \cos\theta d\theta + \frac{1}{2}\rho\omega A \cos\beta\, \Re\{H(\pi+\beta)\} \tag{4.1}$$

$$\bar{F}_y = \frac{\rho\nu^2}{8\pi}\int_0^{2\pi} |H(\theta)|^2 \sin\theta d\theta + \frac{1}{2}\rho\omega A \sin\beta\, \Re\{H(\pi+\beta)\} \tag{4.2}$$

where $H(\theta)$ is the infinite-depth Kochin function defined as

$$H(\theta) = \int\int_{S_B} (\frac{\partial}{\partial n}\phi - \phi\frac{\partial}{\partial n}) e^{\nu(z - ix\cos\theta - iy\sin\theta)} dS \tag{4.3}$$

In particular, when there is no work done by external forces, these equations can

be rewritten in the following forms :

$$\bar{F}_x = \frac{\rho\nu^2}{8\pi}\int_0^{2\pi} |H(\theta)|^2(\cos\theta + \cos\beta)d\theta \tag{4.4}$$

$$\bar{F}_y = \frac{\rho\nu^2}{8\pi}\int_0^{2\pi} |H(\theta)|^2(\sin\theta + \sin\beta)d\theta \tag{4.5}$$

The yaw moment, $\bar{M}_z$ can be obtained using the equation derived by Newman [52].

$$\bar{M}_z = -\frac{\rho\nu}{8\pi} Im\int_0^{2\pi} \bar{H}(\theta)\frac{\partial H}{\partial\theta}(\theta)d\theta - \frac{1}{2}\frac{\rho\omega A}{\nu}\, Im\{\frac{\partial H}{\partial\theta}(\pi+\beta)\} \tag{4.6}$$

where $\bar{H}(\theta)$ means the complex conjugate of $H(\theta)$.

In finite depth, the far-field momentum formula is written as (C.C.Mei [47])

$$\bar{F}_x = -\frac{\rho g A^2}{m_o}\frac{C_g}{C}\,[\,\frac{1}{4\pi}Z^2\int_0^{2\pi}|H_h(\theta)|^2\cos\theta d\theta + Z\cos\beta\; Im\{H_h(\pi+\beta)\}\,] \tag{4.7}$$

$$\bar{F}_y = -\frac{\rho g A^2}{m_o}\frac{C_g}{C}\,[\,\frac{1}{4\pi}Z^2\int_0^{2\pi}|H_h(\theta)|^2\sin\theta d\theta + Z\sin\beta\;\; Im\{H_h(\pi+\beta)\}\,] \tag{4.8}$$

$$\bar{M}_z = -\frac{\rho g A^2}{m_o^2}\frac{C_g}{C}\times [\,\frac{1}{4\pi}Z^2\;\; Im\{\int_0^{2\pi}\bar{H}_h(\theta)\frac{\partial H_h(\theta)}{\partial\theta}d\theta\} - \frac{1}{2}\,\Re\{\frac{\partial H_h(\pi+\beta)}{\partial\theta}\}] \tag{4.9}$$

where

$$Z = \frac{m_o^2-\nu^2}{\nu^2 h - m_o^2 h - \nu}\cosh^2(m_o h) \tag{4.10}$$

$$\frac{C_g}{C} = \frac{1}{2}\{1+\frac{2m_o h}{\sinh(2m_o h)}\} \tag{4.11}$$

and $H_h(\theta)$ is the finite-depth Kochin function, defined as

$$H_h(\theta) = \int\int_{S_B}(\frac{\partial\phi}{\partial n} - \phi\frac{\partial}{\partial n})\; e^{-im_o(x\cos\theta + y\sin\theta)}\frac{\cosh\{m_o(z+h)\}}{\cosh(m_o h)}ds. \tag{4.12}$$

Particularly when there is no external work done to the ship,

$$\bar{F}_x = -\frac{\rho g A^2}{m_o}\frac{C_g}{C} \times [\ \frac{1}{4\pi} Z^2 \int_0^{2\pi} |H_h(\theta)|^2(\cos\theta + \cos\beta)d\theta\ ] \tag{4.13}$$

$$\bar{F}_y = -\frac{\rho g A^2}{m_o}\frac{C_g}{C} \times [\ \frac{1}{4\pi} Z^2 \int_0^{2\pi} |H_h(\theta)|^2(\sin\theta + \sin\beta)d\theta\ ]. \tag{4.14}$$

The diffraction velocity potential is also required to compute the Kochin function. In the present study, the diffraction potential is replaced with the velocity potential of an equivalent two-dimensional wave-maker problem. At first, the diffraction problem based on strip theory is solved. Then the integral equation, equation (3.20), is solved using the strip theory solution. Since equation (3.20) applies to the radiation problem, this method can be considered as the wave-maker problem of a snake-like vessel. That is to say, the ship is set to an equivalent wave maker with a wavelength of $2\pi/\nu\cos\beta$. So the diffraction potential is corrected approximately based on this idea.

## 4.2 Wave Drift Damping : Deep Water

The wave drift damping coefficients can be computed using Aranha's formula which is based entirely upon the knowledge of the drift forces at zero speed. Aranha's formula is valid only in deep water. In the present work, a wave drift damping matrix is obtained using the mean drift forces and moment by unified theory for deep water.

The wave drift damping coefficient, $B_{ij}$, is defined in the drift matrix equation for a ship with small forward speed.

$$\begin{Bmatrix} \bar{F}_{x,U}(\omega,\beta) \\ \bar{F}_{y,U}(\omega,\beta) \\ \bar{M}_{z,U}(\omega,\beta) \end{Bmatrix} = \begin{Bmatrix} \bar{F}_x(\omega,\beta) \\ \bar{F}_y(\omega,\beta) \\ \bar{M}_z(\omega,\beta) \end{Bmatrix}$$

$$
- \begin{bmatrix} B_{11}(\omega,\beta) & B_{12}(\omega,\beta) & B_{16}(\omega,\beta) \\ B_{21}(\omega,\beta) & B_{22}(\omega,\beta) & B_{26}(\omega,\beta) \\ B_{61}(\omega,\beta) & B_{62}(\omega,\beta) & B_{66}(\omega,\beta) \end{bmatrix} \begin{Bmatrix} U_x \\ U_y \\ \Omega_z \end{Bmatrix} \quad (4.15)
$$

where $\bar{F}_{x,U}, \bar{F}_{y,U}, \bar{M}_{z,U}$ are the drift forces and moment when the ship has a steady speed, $U_x, U_y$, and $\Omega_z$. Aranha's formula [2] provides that

$$
\begin{aligned}
B_{11}(\omega,\beta) &= \frac{\omega}{g}[\cos\beta\,\omega\frac{\partial\bar{F}_x}{\partial\omega} - 2\sin\beta\,\frac{\partial\bar{F}_x}{\partial\beta} + 4\cos\beta\,\bar{F}_x] \\
B_{12}(\omega,\beta) &= \frac{\omega}{g}[\sin\beta\,\omega\frac{\partial\bar{F}_x}{\partial\omega} + 2\cos\beta\,\frac{\partial\bar{F}_x}{\partial\beta} + 4\sin\beta\,\bar{F}_x] \\
B_{21}(\omega,\beta) &= \frac{\omega}{g}[\cos\beta\,\omega\frac{\partial\bar{F}_y}{\partial\omega} - 2\sin\beta\,\frac{\partial\bar{F}_y}{\partial\beta} + 4\cos\beta\,\bar{F}_y] \\
B_{22}(\omega,\beta) &= \frac{\omega}{g}[\sin\beta\,\omega\frac{\partial\bar{F}_y}{\partial\omega} + 2\cos\beta\,\frac{\partial\bar{F}_y}{\partial\beta} + 4\sin\beta\,\bar{F}_y] \\
B_{61}(\omega,\beta) &= \frac{\omega}{g}[\cos\beta\,\omega\frac{\partial\bar{M}_z}{\partial\omega} - 2\sin\beta\,\frac{\partial\bar{M}_z}{\partial\beta} + 4\cos\beta\,\bar{M}_z] \\
B_{62}(\omega,\beta) &= \frac{\omega}{g}[\sin\beta\,\omega\frac{\partial\bar{M}_z}{\partial\omega} + 2\cos\beta\,\frac{\partial\bar{M}_z}{\partial\beta} + 4\sin\beta\,\bar{M}_z]
\end{aligned} \quad (4.16)
$$

The first differential terms consider the change of wave frequency caused by the forward speed and the second terms consider the change of wave angle. There are two differential terms in equation (4.16), and these are obtained using a central difference formula.

The third column of the drift damping matrix, $B_{i6}$, can be obtained by the recent Aranha's formula [3] which is based on the slender-body approximation.

$$
\begin{aligned}
B_{16}(\omega,\beta) &\approx B_{26}(\omega,\beta-\frac{\pi}{2}) \\
B_{26}(\omega,\beta) &\approx B_{62}(\omega,\beta) \\
B_{66}(\omega,\beta) &\approx \Gamma B_{22}(\omega,\beta)
\end{aligned} \quad (4.17)
$$

where

$$\Gamma = \frac{\int_L \xi^2 \{1 - (\frac{\partial b(\xi)}{\partial \xi})^2\} d\xi}{\int_L \{1 - (\frac{\partial b(\xi)}{\partial \xi})^2\} d\xi} \tag{4.18}$$

$b(x)$ is the water-line profile of the ship.

Even though Aranha's formula is not conclusively proven to be exact, especially for the radiation problem, it has been found to provide quite accurate predictions of the drift damping coefficients for offshore structures.

# Chapter 5

# Computational Results & Discussion

In order to develop a computer code of unified theory, a strip theory code is essential. For the present computation, the strip theory code developed at MIT for deep water was extended for finite depth. The infinite-depth code is based on NIIRID for the evaluation of the sectional added mass and damping coefficient. NIIRID solves the complete boundary value problem for an arbitrary two-dimensional section. In the computation of the finite-depth problem, the subroutine of NIIRID, which computes the Green function, is extended to finite depth. The finite-depth Green function was evaluated using a series form. The details about the extension are described in Appendix C.

Numerical computations were carried out for a few slender ships. A mathematical hull and a Series 60 hull are considered for the linear and mean drift quantities. The mathematical hull is of parabolic shape, like the Wigley hull, with beam(B)/length(L)=0.15 and draft(T)/length(L)=0.1. The Series 60 hull has the block coefficient ($C_B$) of 0.7, and a parent model is considered. For the wave drift damping coefficients, computations were performed for the mathematical ship used by Finne and Grue [19]. This hull, called Ship1, is expressed by the 4-th order polynomial equation for the beam and a half-circle for the sections.

## 5.1 Solution Grid and Its Dependency

Since unified theory is a slender-body theory, sectional offsets are only necessary for the description of the hull geometry. Figure 5-1 shows the stations for slender-body theory and the three-dimensional mesh for WAMIT on the Series 60 hull. Figure 5-2 shows the distribution of grid nodes on the parabolic hull.

Figure 5-3 shows the dependency of section number on the heave added mass and damping coefficient for the parabolic hull. In this case, the number of nodes on each section is fixed. Figure 5-4 shows the effect of node number with the fixed number of sections. Both results show the insensitivity of solution grid for linear quantities. Table 1 compares the values for one specific case, $\omega\sqrt{L/g} = 2.0$. It is surprising that the result with 5 stations and 3 nodes on each section is not much different with the that of 40 stations and 20 nodes. Even for a mathematical hull form, this result is quite encouraging.

| station | node | $a_{33}$ | $b_{33}$ |
|---|---|---|---|
| 5 | 3 | 3.1767739E-03 | 5.7931738E-03 |
| | 5 | 3.1702337E-03 | 5.7432665E-03 |
| | 10 | 3.1910257E-03 | 5.7664076E-03 |
| 10 | 5 | 3.1650849E-03 | 5.8484091E-03 |
| | 10 | 3.1855819E-03 | 5.8818124E-03 |
| | 15 | 3.1951349E-03 | 5.8921375E-03 |
| 20 | 5 | 3.1638728E-03 | 5.8937315E-03 |
| | 10 | 3.1846275E-03 | 5.9162732E-03 |
| | 15 | 3.1943801E-03 | 5.9264624E-03 |
| 30 | 5 | 3.1635107E-03 | 5.9003350E-03 |
| | 10 | 3.1850706E-03 | 5.9226453E-03 |
| | 15 | 3.1948064E-03 | 5.9333052E-03 |
| 40 | 10 | 3.1848375E-03 | 5.9254845E-03 |
| | 15 | 3.1948953E-03 | 5.9358547E-03 |
| | 20 | 3.1997717E-03 | 5.9412871E-03 |

Table 5.1: The heave added mass ($a_{33}$) and damping coefficient($b_{33}$) for different grids (half domain) ; parabolic hull, $h/L = 0.2, \omega(L/g)^{1/2} = 2.0$

The grid dependency on the second-order quantities has to be observed since these has a shorter length scale than the linear quantities. Figure 5-5 shows the convergence of the longitudinal mean force on the parabolic hull. The results shows more sensitivity on the number of station. However, the grid dependency on the second-order quantities are not serious so that usually more than 20 stations provides a nice convergence.

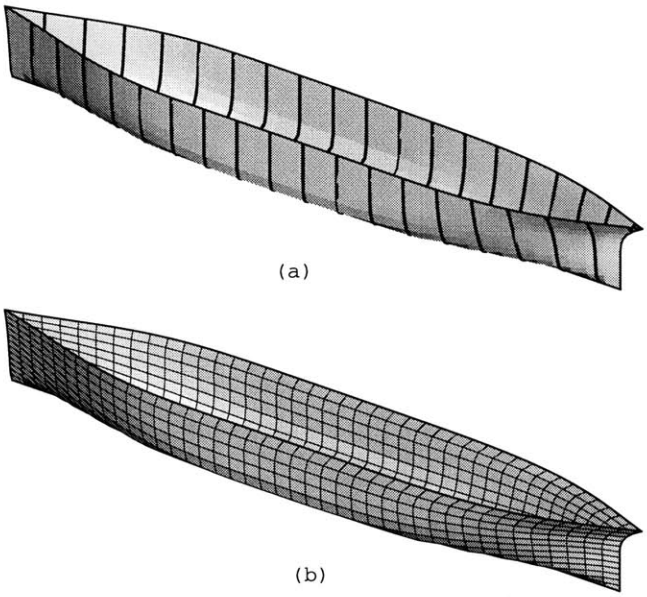


Figure 5-1: Solution grid for the Series 60 hull : (a) for unified theory, (b) for WAMIT

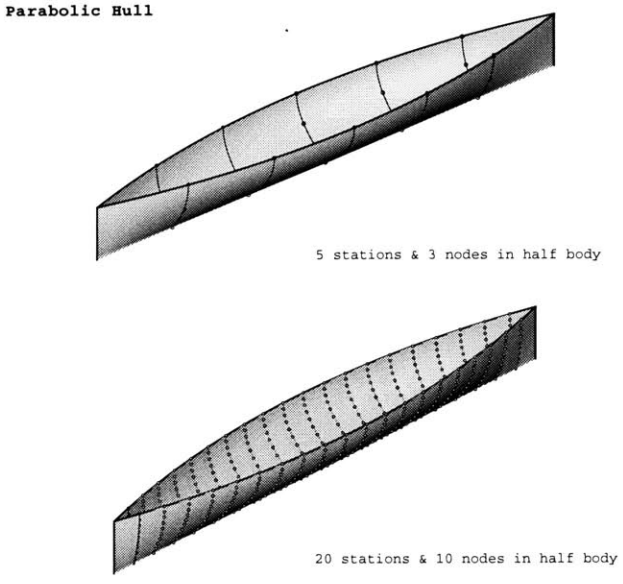


Figure 5-2: Distribution of grid nodes on the parabolic Hull

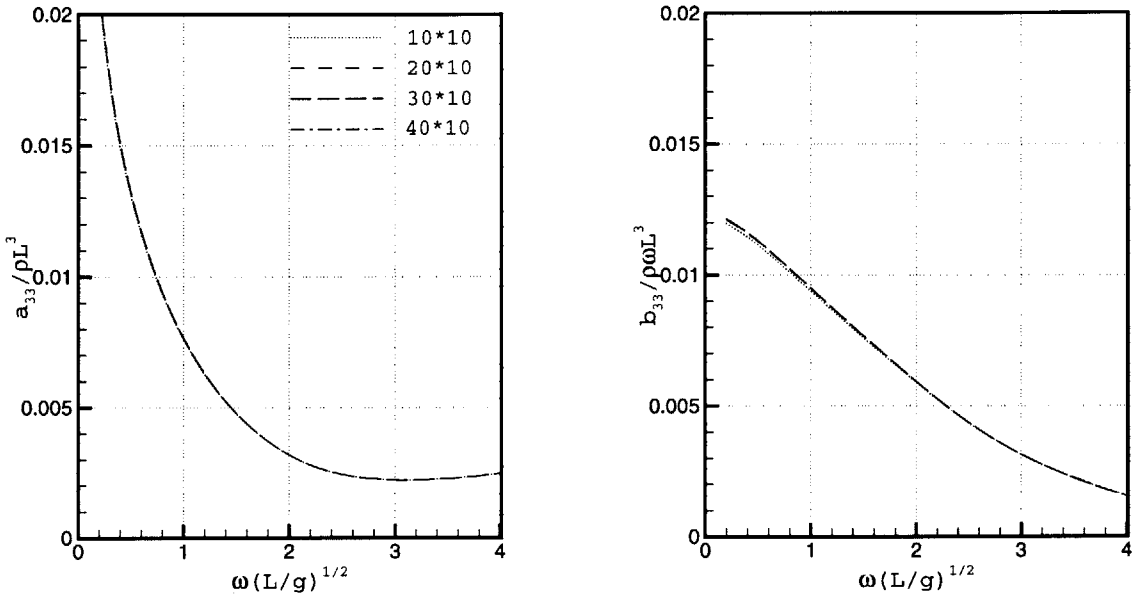


Figure 5-3: Grid dependency on the heave added mass and damping coefficient : different number of sections, parabolic hull, $h/L = 0.2$

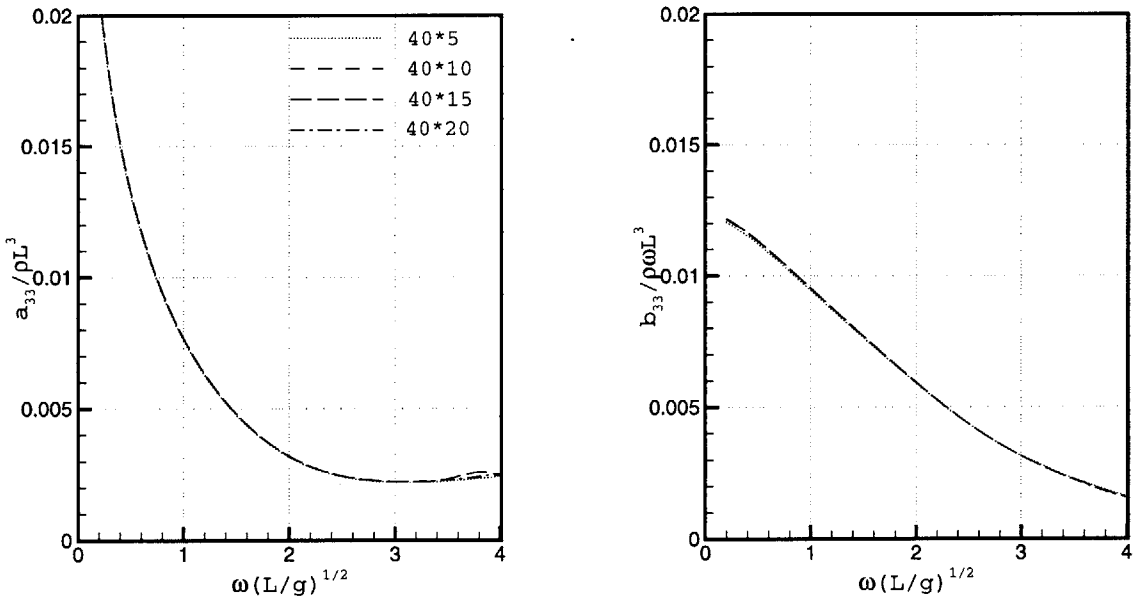


Figure 5-4: Grid dependency on the heave added mass and damping coefficient : different number of nodes, parabolic hull, $h/L = 0.2$

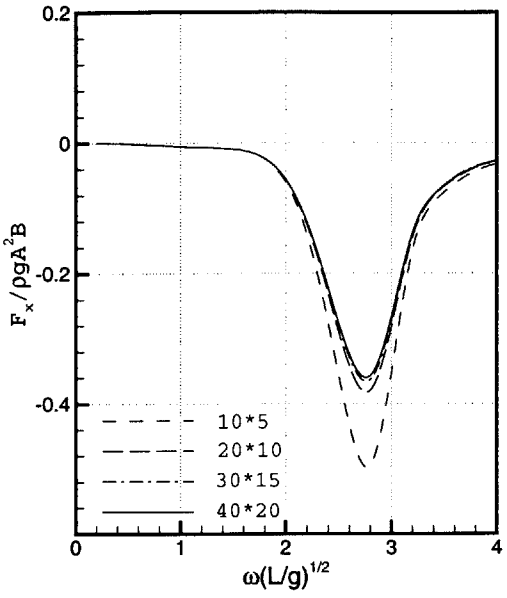


Figure 5-5: Grid dependency on the second-order mean force : parabolic hull, $h/L = 0.2, \beta = 180^o$

## 5.2 Hydrodynamic Forces

The accuracy of the hydrodynamic forces depends on that of velocity potential. Since the computation of the hydrodynamic forces requires the surface integration of the velocity potential on ship sections, the accurate velocity potential guarantees the accurate hydrodynamic forces. The accuracy of the velocity potential is also related with the second-order quantities, and it will be mentioned later.

Figure 5-6 plots $a_{33}$ and $b_{33}$ for deep water, and these are compared with the results of strip theory and WAMIT. It is obvious that strip theory is not suitable at low frequencies.

Figure 5-7 and 5-8 compare the heave and pitch added mass and damping coefficients. It is obvious that the present unified theory provides an accuracy as good as the deep water case. In particular, at low frequency, the strip theory solution shows a large discrepancy with those of WAMIT and unified theory.

Strip theory is valid in the high frequency range. When the wave length is large compared with the ship length, the three-dimensional effect becomes more significant so that strip theory is not good as much as in the high frequency range. These results show clearly the weak point of strip theory. The same trend can be observed in Figure 5-9 for the heave-pitch cross coupling terms.

Depth effects on the heave added mass and damping coefficient are shown in Figure 5-10 and 5-11. At low frequencies, the hydrodynamic coefficients are very sensitive to depth.

The hydrodynamic coefficients of other motions are shown in Figure 5-12 and 5-13. These results are by strip theory, and there is some discrepancies in both motions.

Figure 5-14 and 5-15 shows the wave excitation forces and moment in head waves. These results are for deep water, and the far-field Haskind formula is applied in this computation. The same accuracy is found in the finite depth problem. As expected, unified theory shows a good agreement with WAMIT. For the motions where unified

theory is not available, $\sigma_j$ can be used instead of $q_j$.

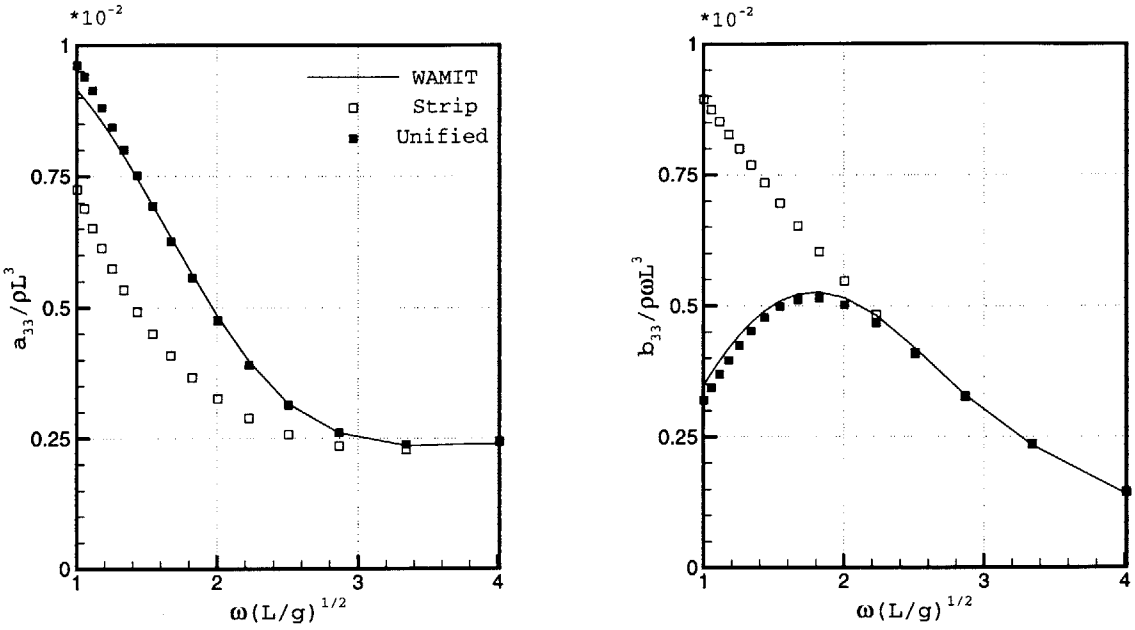


Figure 5-6: The heave added mass and damping coefficient : parabolic hull, infinite depth

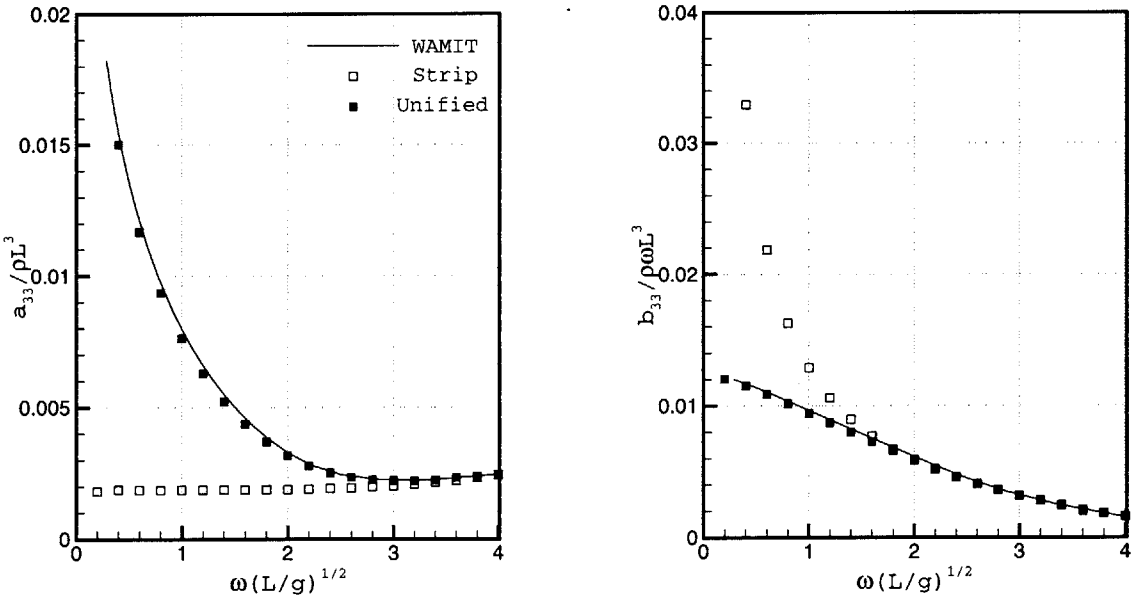


Figure 5-7: The heave added mass and damping coefficient : parabolic hull, $h/L = 0.2$

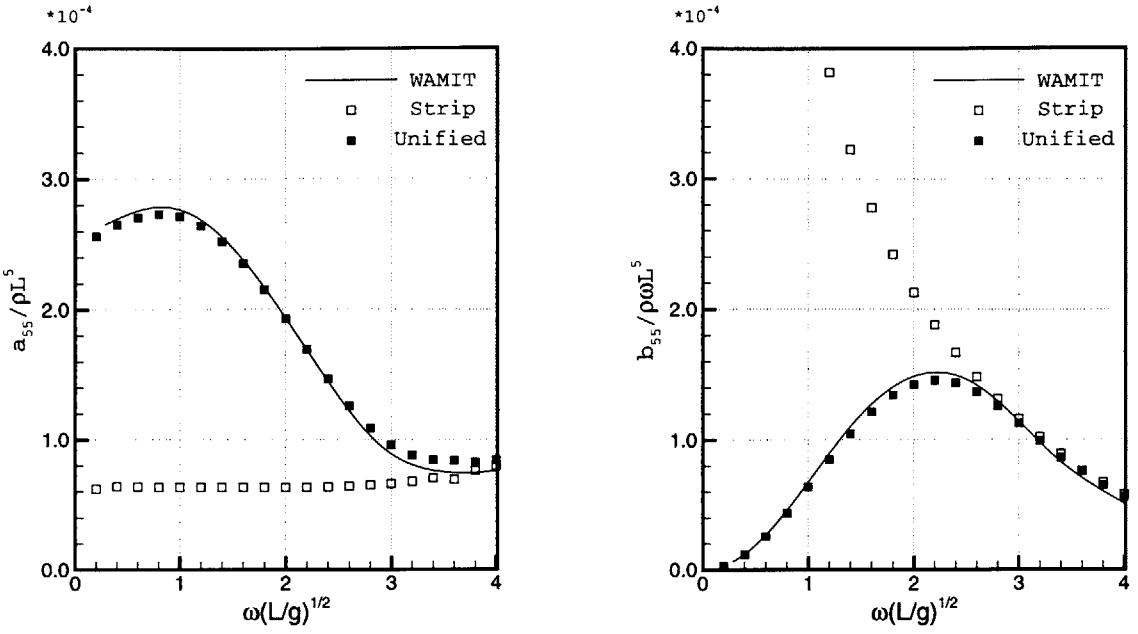


Figure 5-8: The pitch added mass and damping coefficient : parabolic hull, $h/L = 0.2$

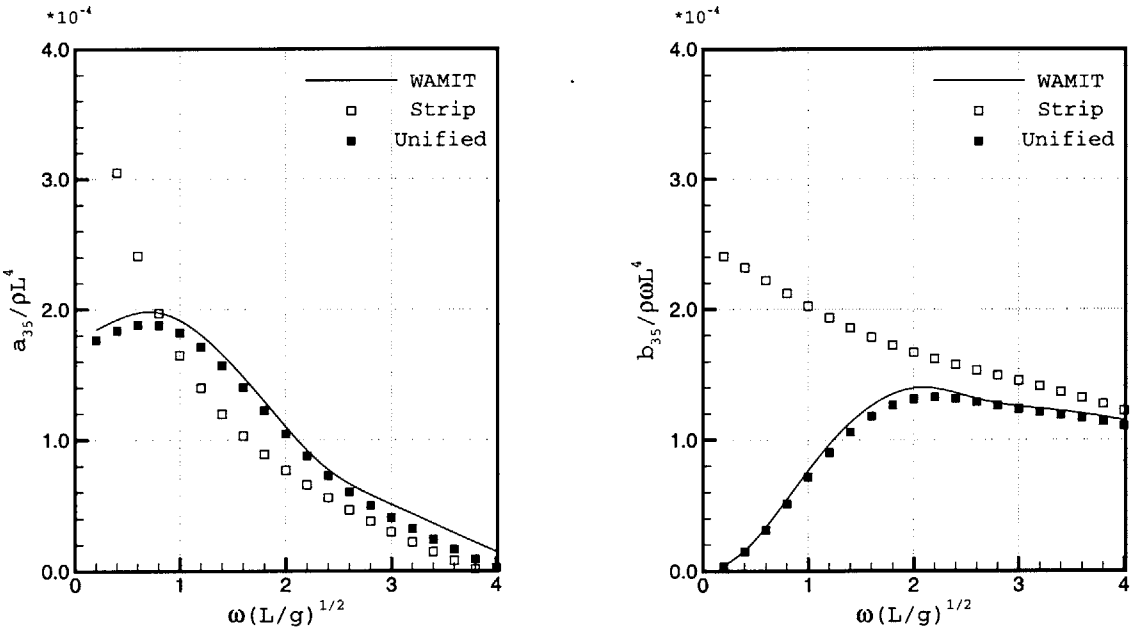


Figure 5-9: The heave and pitch cross-coupled added mass and damping coefficient : parabolic hull, $h/L = 0.2$

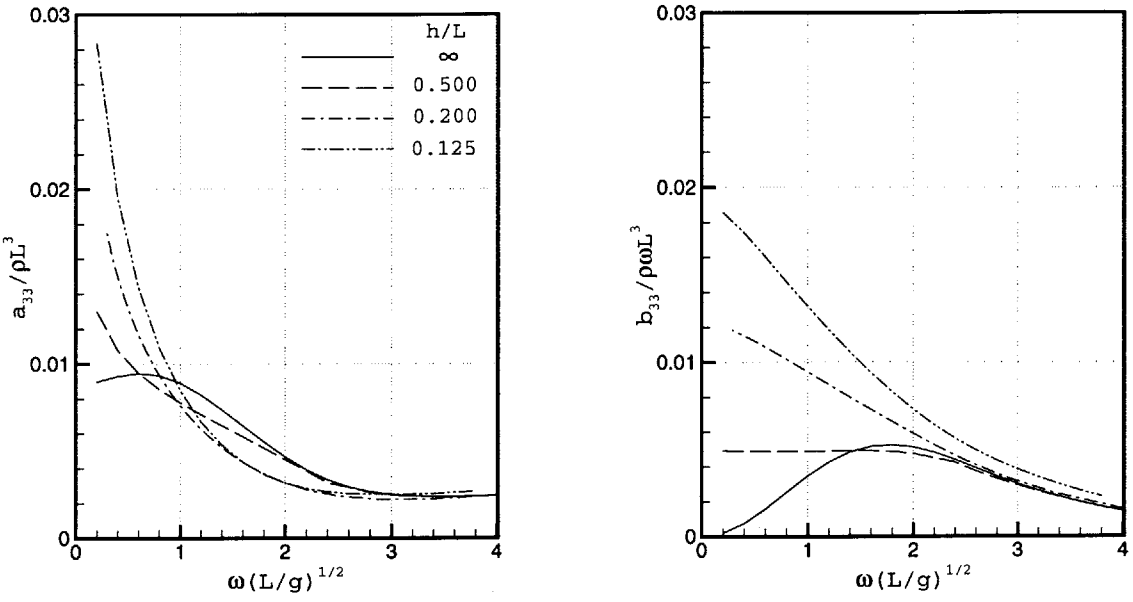


Figure 5-10: Effects of water depth on the heave added mass and damping coefficient : parabolic hull

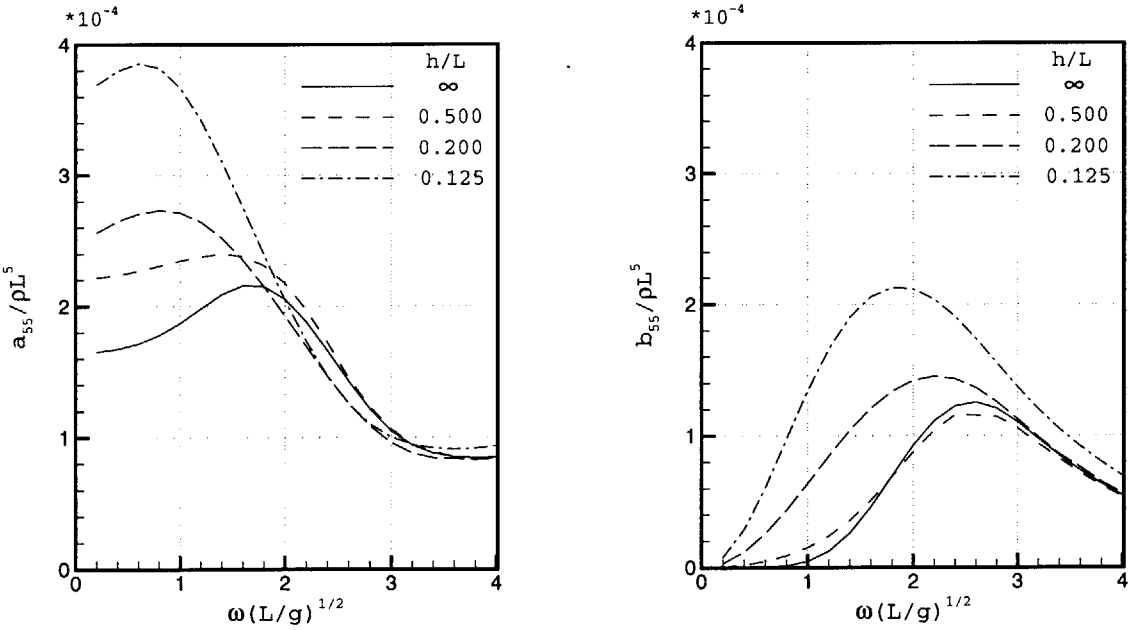


Figure 5-11: Effects of water depth on the pitch added mass and damping coefficient : parabolic hull

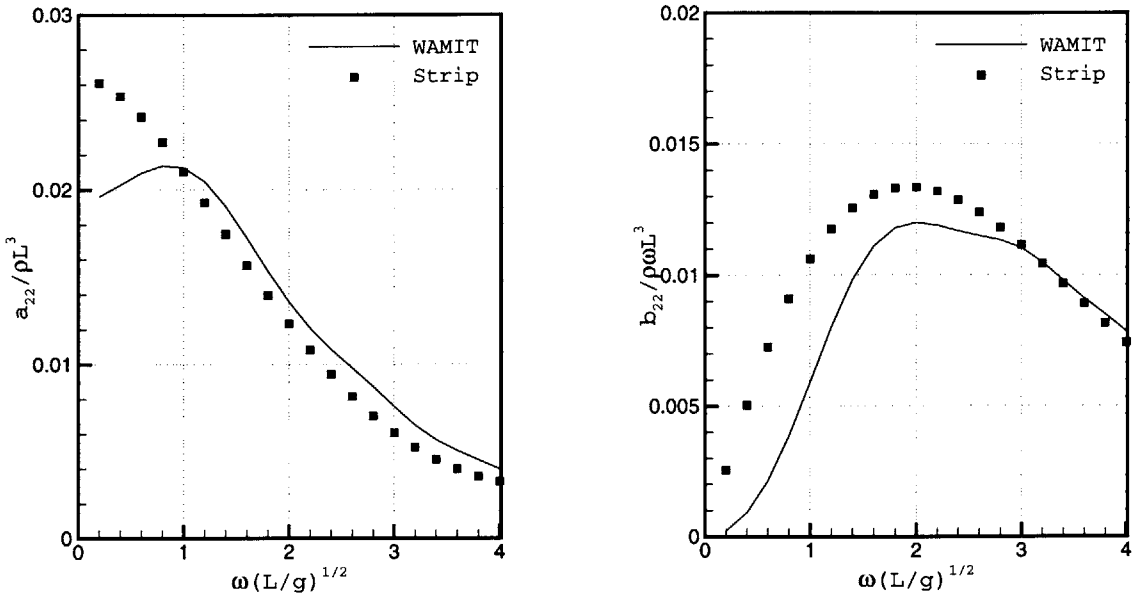


Figure 5-12: The sway added mass and damping coefficient : parabolic hull, $h/L = 0.125$, strip theory

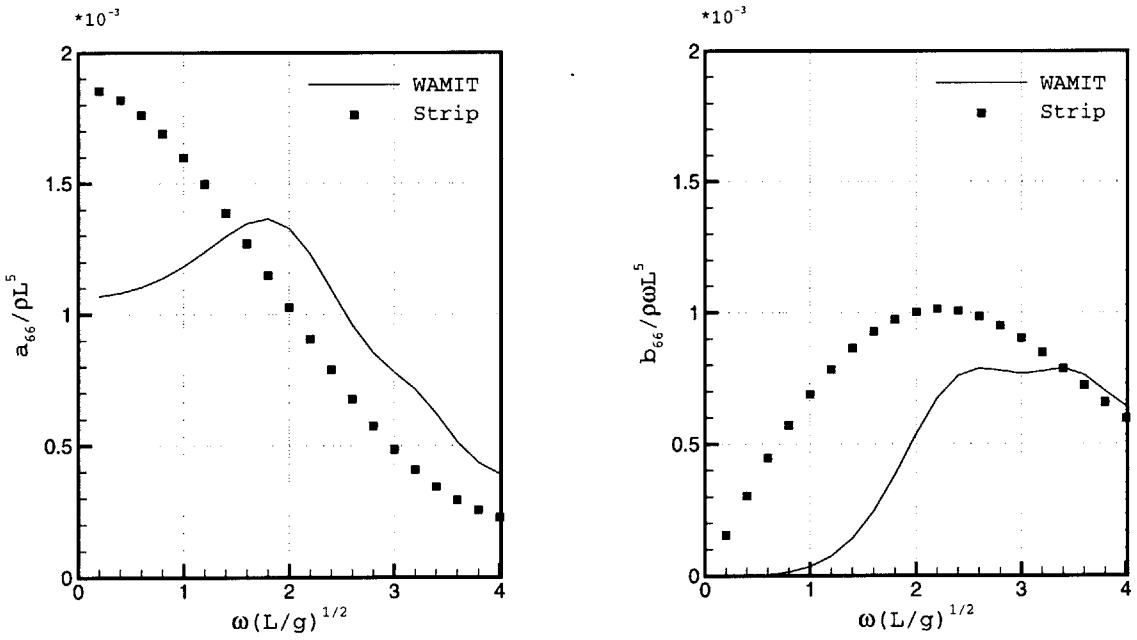


Figure 5-13: The yaw added mass and damping coefficient : parabolic hull, $h/L = 0.125$, strip theory

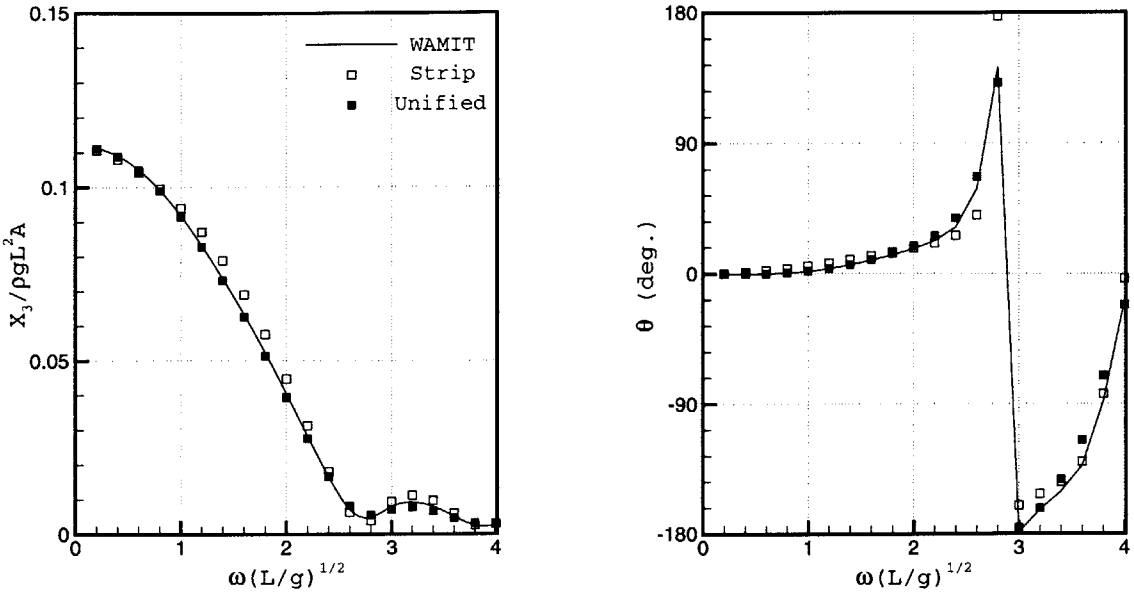


Figure 5-14: Wave excitation heave force (magnitude and phase) : Series 60, infinite depth, $\beta = 180^o$

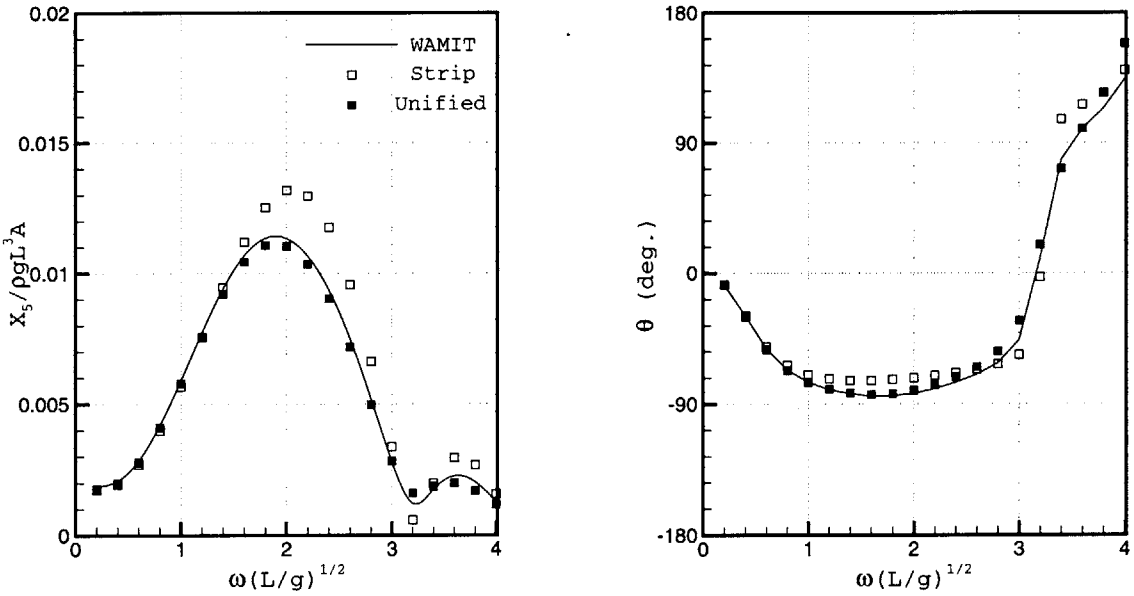


Figure 5-15: Wave excitation pitch moment (magnitude and phase) : Series 60, infinite depth, $\beta = 180^o$

## 5.3 Motion RAOs

Figure 5-16 and 5-17 shows the heave and pitch motion RAOs of the Series 60 hull in deep water, and unified theory predicts very accurate motion RAOs. When the ship has no forward speed, the heave and pitch motions are more important than others since the ship will change her position to be parallel to the wave direction.

It is interesting that the results of strip theory don't show the large deviation from unified theory. In particular even at low frequencies where the hydrodynamic coefficients are inaccurate, strip theory shows reasonable motion RAO. It seems that the dominant force at the low frequency range comes not from the added mass and damping but from the restoring force. Actually this is the reason why strip theory is still valid for the analysis of the linear seakeeping performance. Therefore, if only the motion RAO is of interest, strip theory may be not a bad choice.

However, when it comes to an extension to the second-order quantities, the accuracy of the linear solution is more important. In order to compute the second-order quantities using the linear solutions, the linear solution should be as accurate as possible. In this case, the accuracy of strip theory is not enough. This issue will come back in next section.

Figure 5-18 shows the depth effects on the motion RAO. It is interesting that the heave motion is less than the deep-water case when the depth become shallow, in particular at low frequencies. Since, for a fixed frequency, the incident wave length becomes shorter as the depth decreases, the heave response at low frequencies is not large as much as in deep water case. Also the peak of the pitch motion shifts to a lower frequency.

Figure 5-19 shows the heave and pitch RAOs in finite depth. The motion RAO for finite depth has the same accuracy with that of deep water. Both unified and strip theory don't show large discrepancies with WAMIT.

Figure 5-20 shows the sway motion RAO and its phase at oblique sea. At oblique

ship, sway, roll and yaw motions becomes significant, and strip theory predicts the motion RAOs very well. Figure 5-20 and 5-21 shows the results for the roll and yaw motions, and the present strip theory code provides a nice agreement with WAMIT.

The viscous damping in the roll motion plays a significant roll at resonance. Figure 5-22 shows the effects of the viscous damping at the roll resonance. The resonance frequency is a function of the transverse metacentric height which is related with the ship beam. Besides the motion RAO is narrow banded near resonance, as shown in figure 5-22. The values of $C_D$ applied in this figure are 0.05 and 0.075, and these are the general range of $C_D$ in real ships. The application of viscous damping offers more realistic motion RAO.

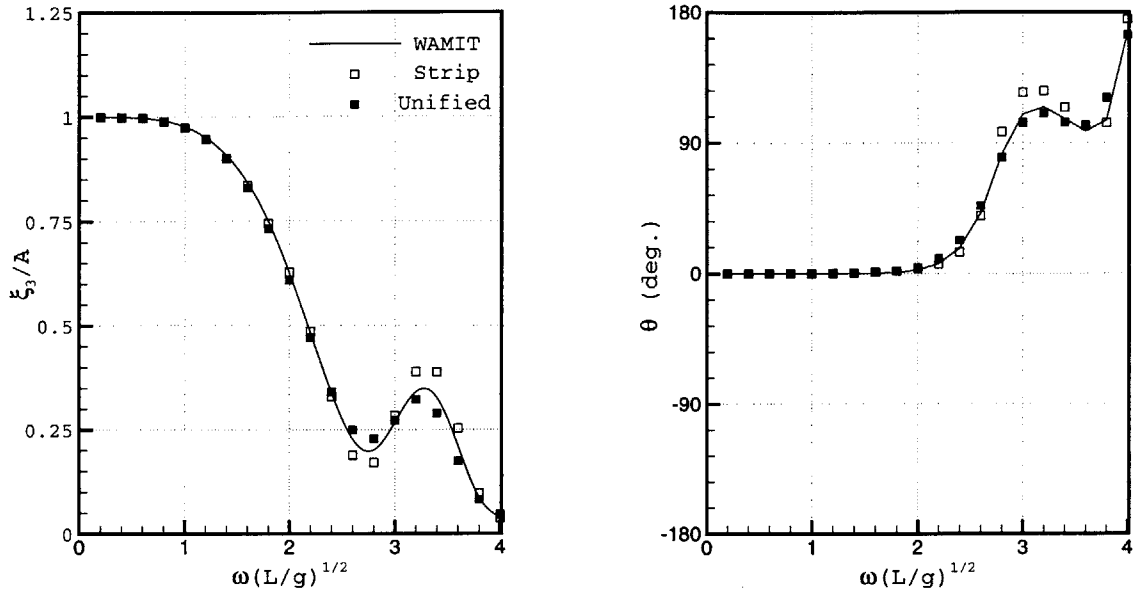


Figure 5-16: Heave RAO (magnitude and phase) : Series 60, infinite depth, $\beta = 180^o$

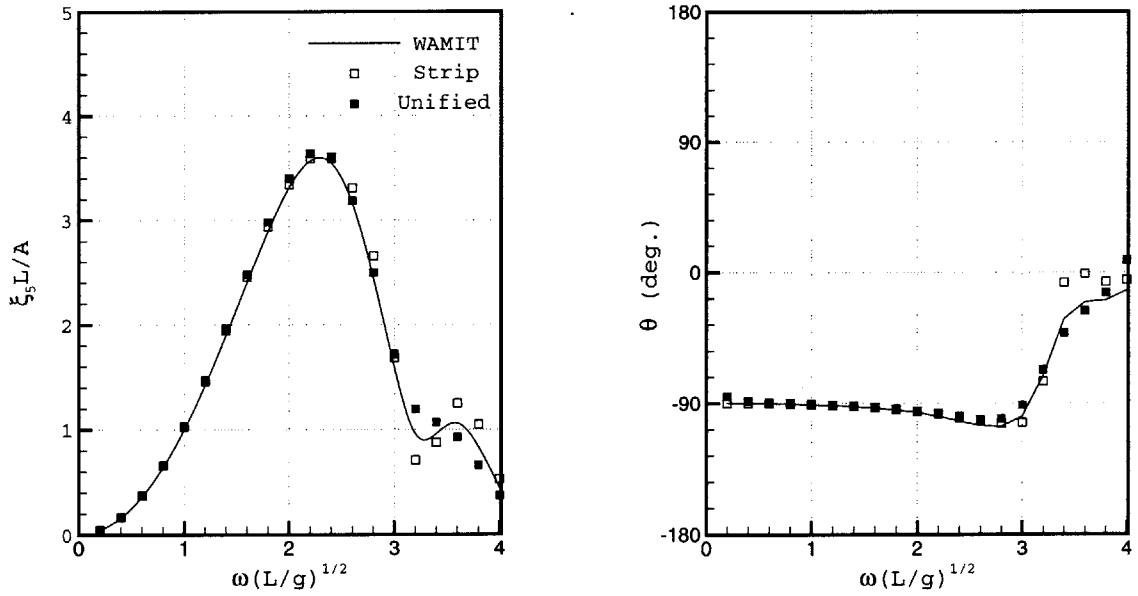


Figure 5-17: Pitch RAO (magnitude and phase) : Series 60, infinite depth, $\beta = 180^o$

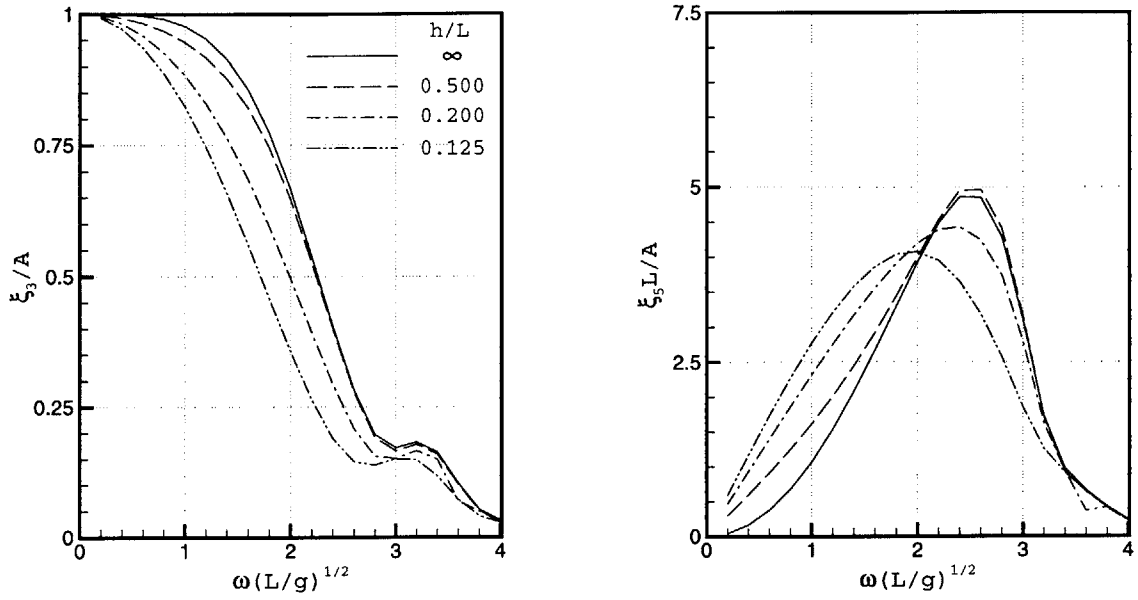


Figure 5-18: Effects of water depth on the heave and Pitch RAOs (magnitude) : parabolic hull, $\beta = 180^o$

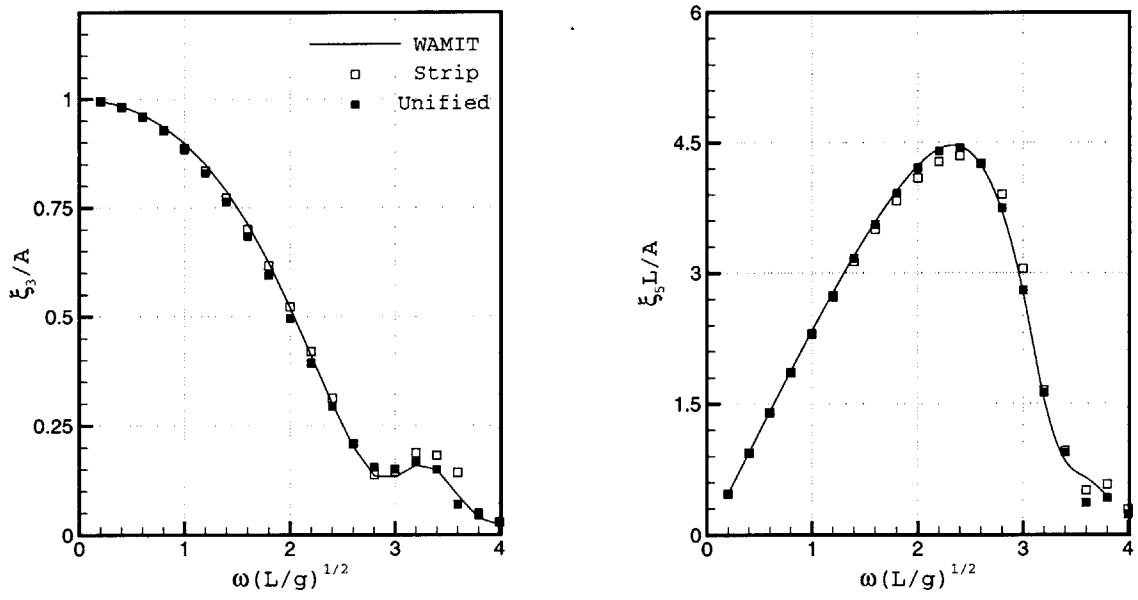


Figure 5-19: Heave and Pitch RAOs (magnitude) : parabolic hull, $h/L = 0.2, \beta = 180^o$

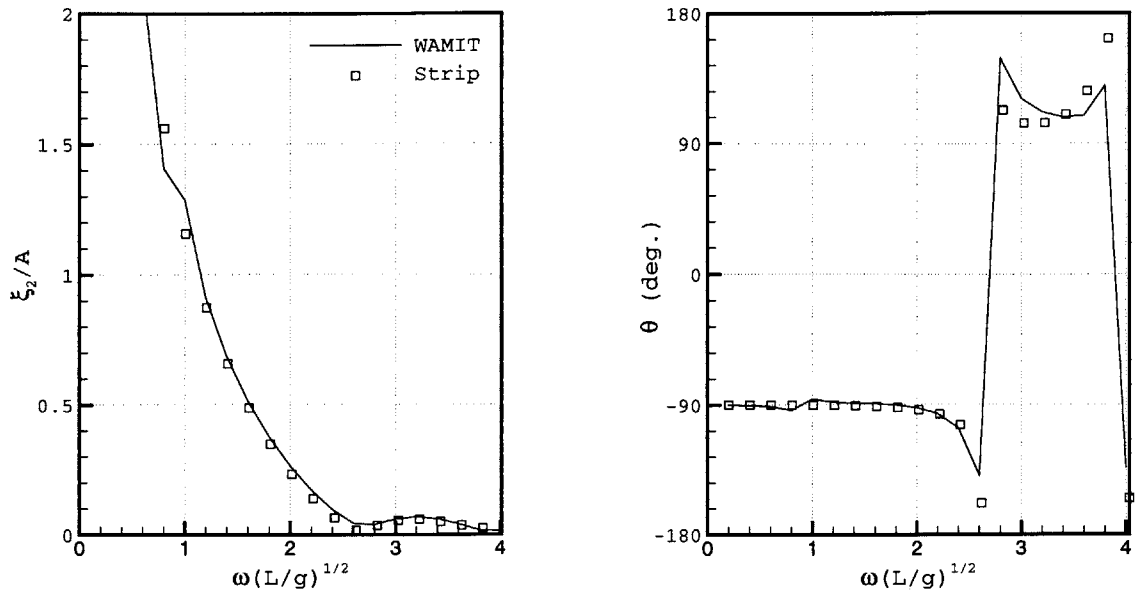


Figure 5-20: Sway RAO at oblique sea (magnitude and phase) : Series 60, $h/L = 0.125, \beta = 150^o$

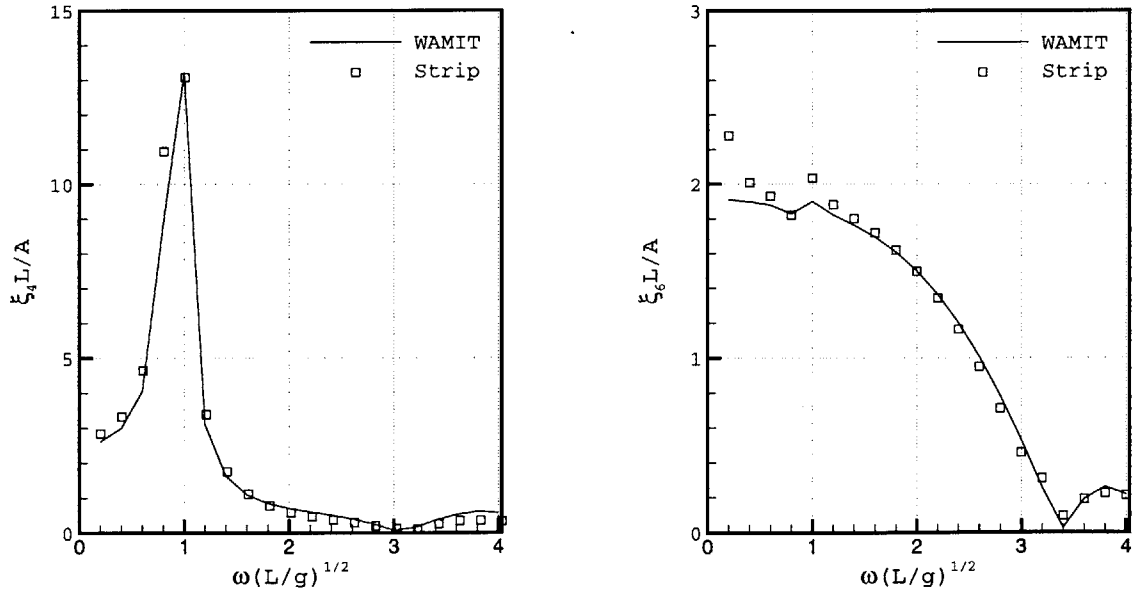


Figure 5-21: Roll and yaw RAOs at oblique sea (magnitude and phase) : Series 60, $h/L = 0.2, \beta = 150^o$

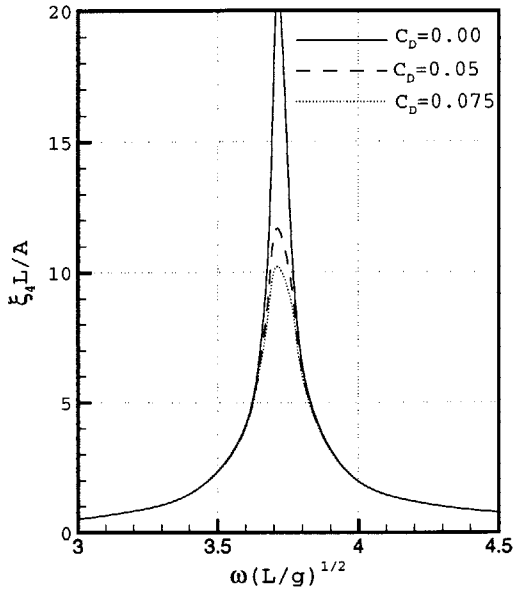


Figure 5-22: Effects of the equivalent viscous damping on roll motion : Series 60, infinite depth, $\beta = 90^o, kA = 0.05$

## 5.4 The Second-Order Quantities

Albeit strip theory predicts the reasonable motion RAO, the velocity potential is not accurate as much as motion RAO. It was proven in the results of the hydrodynamic forces. Since the computation of the second-order forces requires the velocity potential as well as the motion RAO, unified theory is expected to produce better results of the second-order quantities.

Figure 5-23 compares the Kochin function of slender-body theory with WAMIT's. At a low frequency, the magnitude of the Kochin function is dictated by the real component since Froude-Krylov force is dominant, while the imaginary term plays important roll at high frequencies. Some discrepancy is found near $\theta = 0$ and $\pi$, but the general agreement is favorable.

In Figure 5-24, the longitudinal mean drift force is shown for different depths. When $h/L$ is 1.0, 0.5, the discrepancy with the infinite depth limit is not so significant. However, as the depth becomes smaller, the force reduces and the frequency of the peak shifts. A wavelength in finite depth is shorter than that of deep water at the same frequency. In this case, the motion RAOs near the peak in finite depth is smaller than in the deep-water case. In consequence the magnitude of the peak becomes smaller and the frequency of the peak changes a little.

Figure 5-25 shows the comparison of the longitudinal mean force by WAMIT, strip and unified theories. Since the wave heading is $180^o$, only the heave and pitch motions contribute to the mean force in the radiation problem. The agreement between WAMIT and unified theory is not as good as for the linear quantities, but it is quite acceptable, especially near the peak. In the practical sense, the longitudinal force is very important since the ship changes her position to be parallel to the wave direction.

Figure 5-26 shows the longitudinal mean drift forces on the Series 60 hull at oblique sea. In this case, the angle of the incoming wave is $150^o$, and the contributions from sway, yaw and roll motions are significant. Therefore this result is the combination

of unified and strip theories. The accuracy is not as good as the head sea case, and the main source of this discrepancy is the strip theory solution.

Figure 5-27 shows the lateral mean drift forces on the Series 60 hull at oblique sea. The slender-body solution shows nice agreement with WAMIT, unlike the longitudinal forces. In order to figure out this inconsistency, consider the order of magnitude for both forces. The orders of magnitude of the longitudinal and lateral drift forces are different. As shown in Figure 5-26 and 5-27, the longitudinal force is non-dimensionalized with respect to ship beam, and the lateral force by the ship length. This means that the longitudinal force is much smaller than the lateral force, which is natural for a slender body. Hence the longitudinal force is more difficult to predict.

The mean yaw moments at oblique sea are shown in Figure 5-28, and the yaw moments are found not accurate as much as forces.

Figure 5-29 shows the wave drift damping coefficient, $B_{66}$, for Ship1. Finne and Grue [19] obtained the wave drift damping using a three-dimensional panel code, and this figure compares $B_{66}$ with their result. Equation (4.17) is used for slender-body theory. In this figure, ITTC wave spectra are overlapped to indicate the frequency range of real ocean waves. The frequencies of these spectra are normalized, and the ship length is assumed to be 100m which is a reasonable approximation. This figure shows that Aranha's formula provides a reasonable trend in the frequency range where the energy of the ocean wave is dominant. However, at high frequencies, Aranha's formula seems unsuitable to use.

Figure 5-30 shows $B_{11}$ for Ship1. In this figure, $B_{11}$ by Aranha's formula using equation (4.16) is compared with the result of Finne and Grue. When $kL$ is larger than 7, the discrepancy between these results are significant. From Figure 5-29 and 5-30, it is obvious that Aranha's formula is not applicable in the entire frequency range. It is not proper to judge Aranha's formula with a few limited results, but it seems that something is missing in Aranha's formula. In spite of its lack of theoretical background, Aranha's formula have a fascinating advantage that it requires the drift force only at zero speed. Therefore a more profound study is needed.

In the prediction of the drift motion, the viscous effects cannot be ignored. For a slender ship, the viscous effects become significant in the sway and yaw drift motion. A Morrison-type approximation would be used, but a systematic study is necessary.

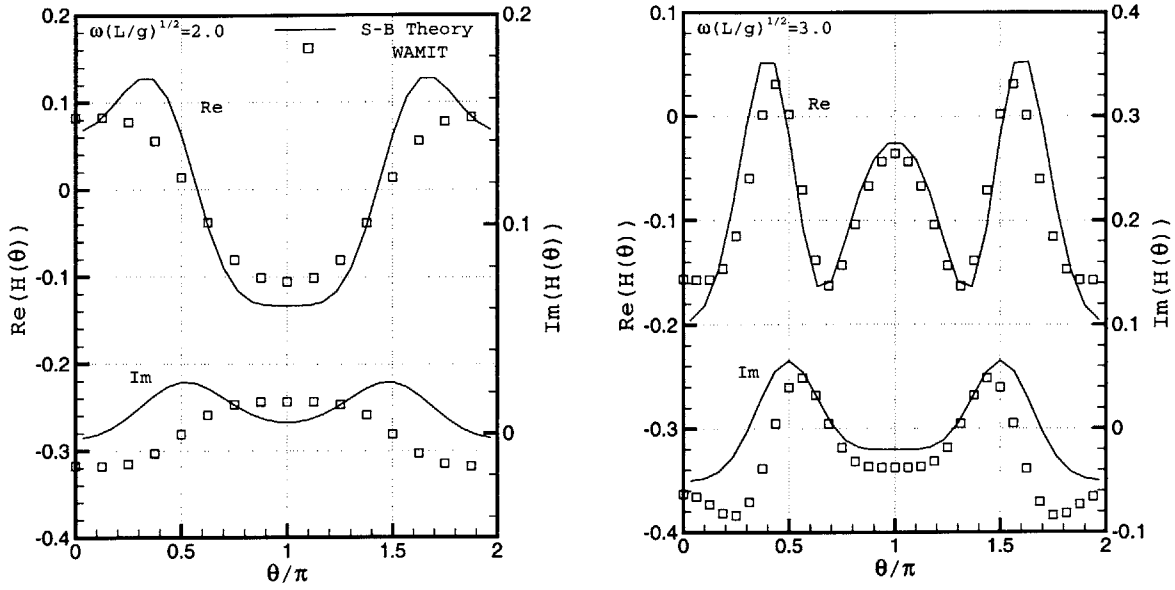


Figure 5-23: Comparison of Kochin function with WAMIT : parabolic hull, $h/L = 0.2, \beta = 180^o$

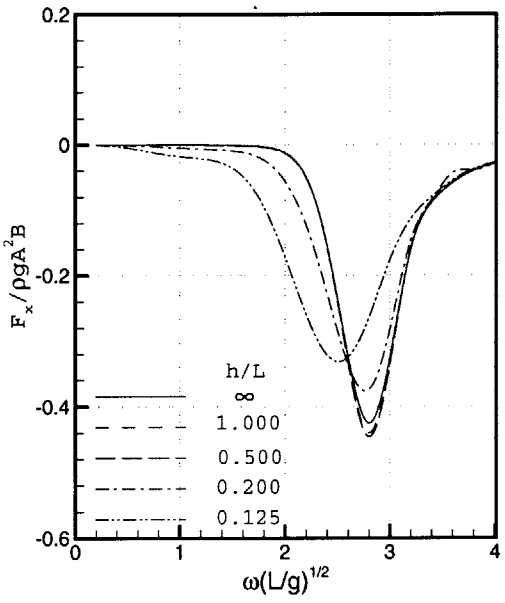


Figure 5-24: Depth effects on the second-order mean force : parabolic hull, $\beta = 180^o$

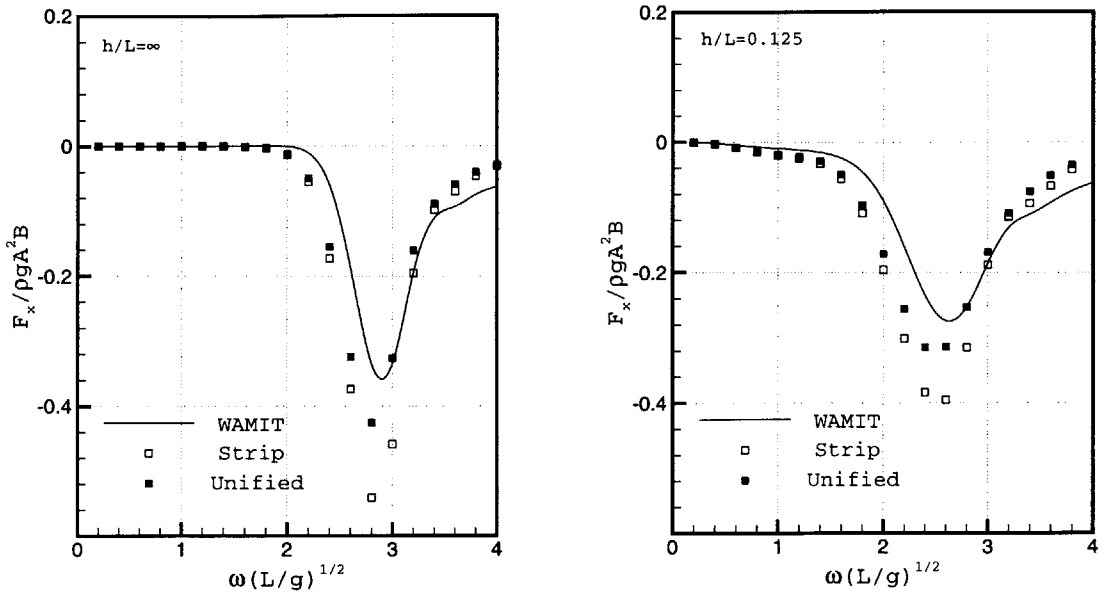


Figure 5-25: Longitudinal mean drift force : parabolic hull, $h/L = \infty, 0.125, \beta = 180^o$

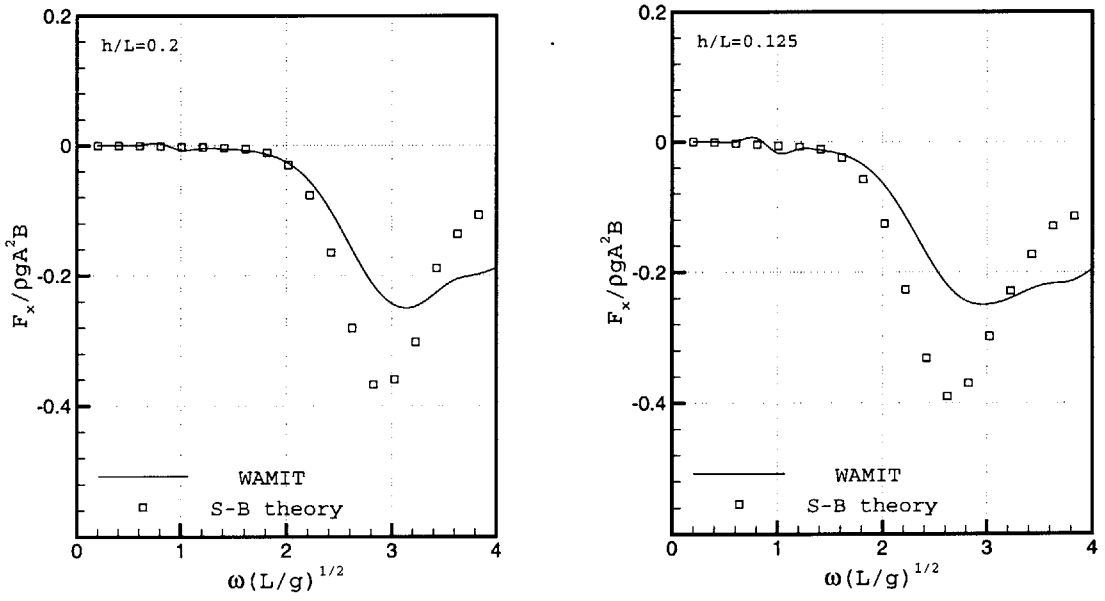


Figure 5-26: Longitudinal mean drift force at oblique sea : Series 60, $h/L = 0.2, 0.125, \beta = 150^o$

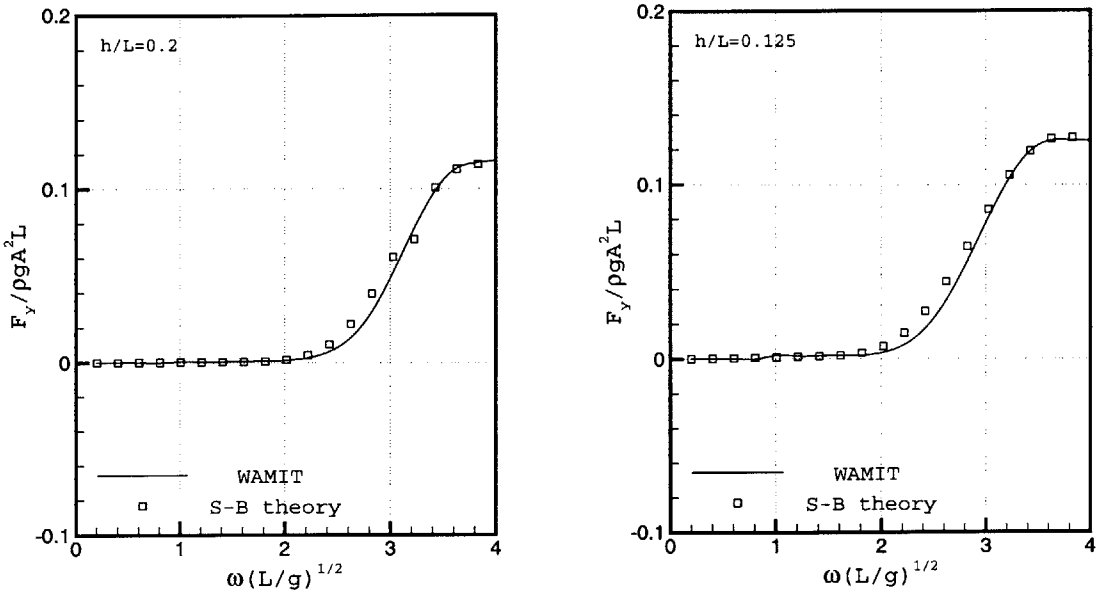


Figure 5-27: Lateral mean drift force at oblique sea : Series 60, $h/L = 0.2, 0.125, \beta = 150^o$

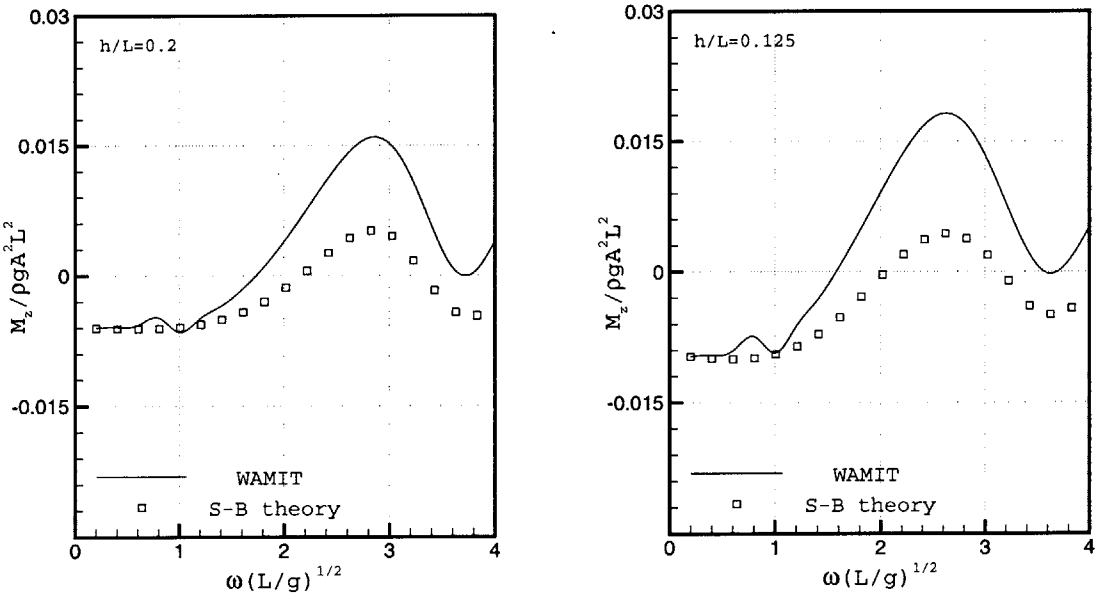


Figure 5-28: Yaw mean drift moment at oblique sea : Series 60, $h/L = 0.2, 0.125, \beta = 150^o$

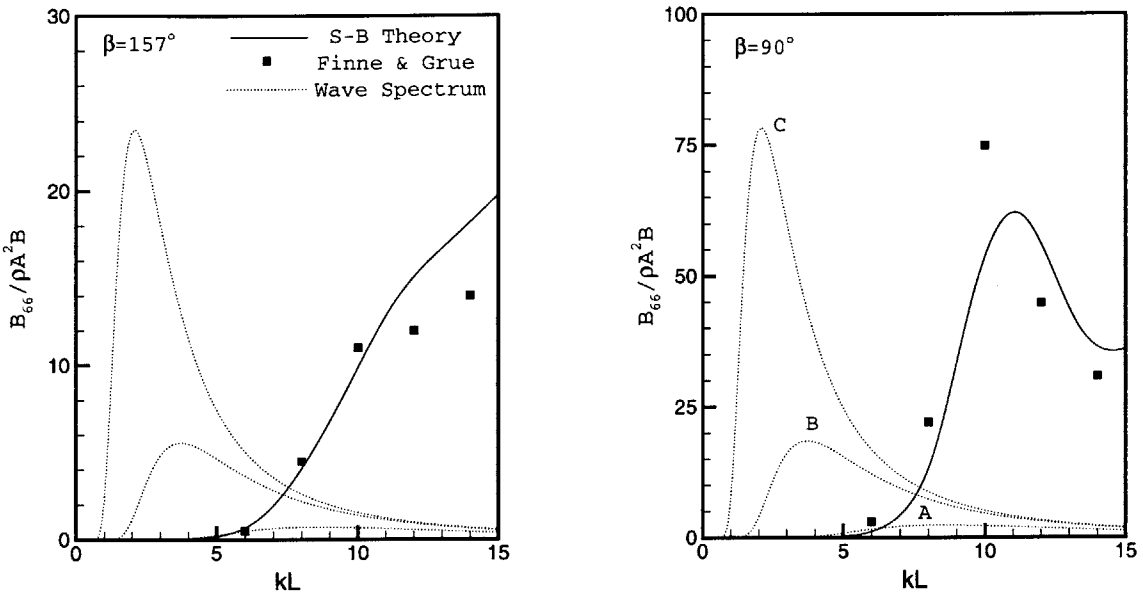


Figure 5-29: Yaw wave drift damping coefficients, $B_{66}$, and ITTC wave spectrum for $L = 100m$ : ship1, infinite depth, $\beta = 157^o$(left) & $\beta = 90^o$(right), $H_s/L = 0.022(A), 0.05(B), 0.089(C)$, $T_m(g/L)^{1/2} = 1.35(A), 2.51(B), 3.35(C)$

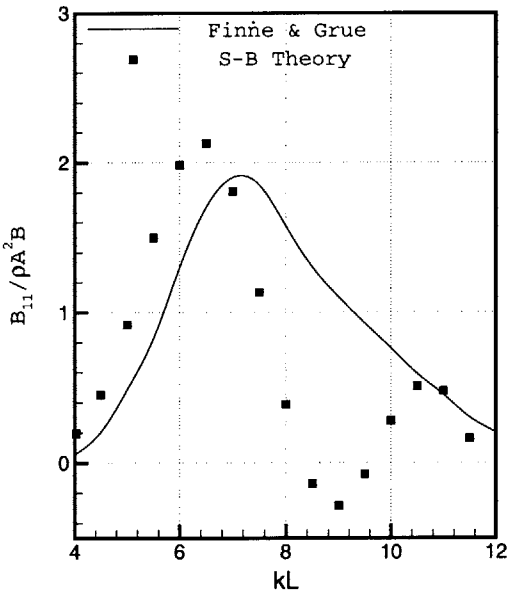


Figure 5-30: Surge wave drift damping coefficients, $B_{11}$ : ship1, infinite depth, $\beta = 180^o$

# Chapter 6

# Conclusions & Contributions

In the present part of the thesis, slender-body theory is applied to compute the linear hydrodynamic forces, motion RAOs and second-order forces. The heave and pitch motions were solved using unified theory, while other motions were solved using strip theory. In order to take into account water depth, unified theory is extended to finite depth.

One of the main contributions of this part is the analytic derivation of a finite-depth unified theory. The analytic forms of the far- and near-field solution in finite depth were derived under slender-body assumption, and a new integral equation was obtained for the strength of three-dimensional wave sources. The kernel was written as a series form which makes it easy to compute. From the comparison of the kernel with that of infinite depth, the limit case of deep water was proved.

An another contribution is the development of a computer code based on the proposed theoretical background. A strip theory code was extended to finite depth, and the development was continued to unified theory for infinite and finite depth. For the sectional computation, NIIRID was extended to finite depth. Numerical computations were carried out for a few typical slender ships, and the hydrodynamic coefficients and motion RAOs was compared with WAMIT's for validation.

In finite depth, the hydrodynamic coefficients are sensitive to water depth at low frequencies. The results which are based on unified theory showed nice agreement

with WAMIT. The same accuracy of unified theory was found for the wave excitation forces and moment. For the motion RAOs, it was found that both unified theory and strip theory predict reasonable values.

The other contribution of the present part is the extension of its computation to the second-order quantities. Since unified theory was proved to provide an accuracy comparable with three-dimensional codes for the linear problem, its solution may be used to compute the second-order quantities. In the computation of the second-order quantities, the accuracy is dependent on Kochin function. Unified theory addes a correction to the near-field solution of strip theory so that Kochin function is more accurate than strip theory. The comparison with WAMIT's result showed a favorable agreement of the mean-drift forces and moment in finite depth as well as infinite depth.

The present work was extended to the wave drift damping for deep water, and Aranha's formula was applied. Aranha's formula has an advantage that it is based entirely upon the knowledge of the drift forces at zero speed. From this study, it was observed that Aranha's formula may be useful in the frequency range in which most of ocean wave energy is, but a very thorough study for this formula is required.

According to the present result, slender-body theory is thought to be an efficient and elegant method to predict the seakeeping performance and second-order quantities of slender ships. Slender-body theory requires much less memory and faster CPU time than any other three-dimensional code. Furthermore, unified theory has an accuracy similar with a three-dimensional code with very simple input data of the hull geometry. Therefore, the method proposed in this thesis is expected to be used directly to the initial design of a floating ship, like an FPSO.

# PART II

# LINEAR & SECOND-ORDER FREE SURFACE FLOW AROUND OFFSHORE STRUCTURES

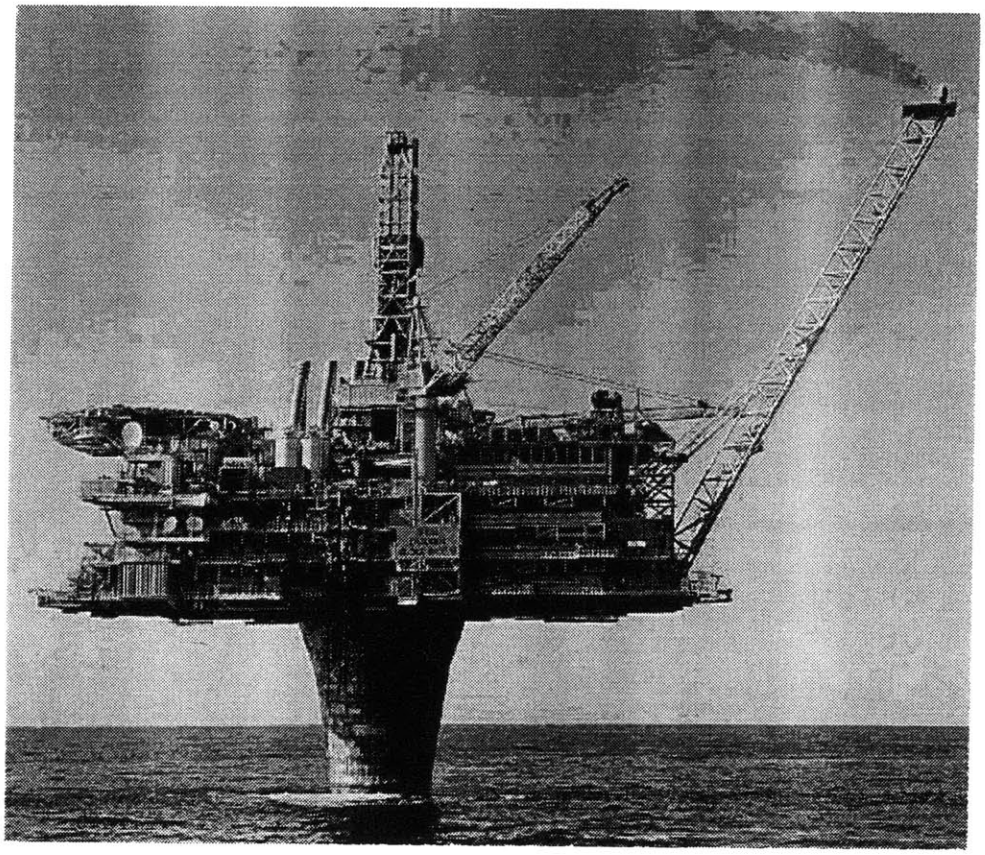

# Chapter 1

# Introduction

The aim of this part is to develop models and a corresponding computational code for the simulation of the nonlinear wave-induced loads and responses of realistic structures. Oil and gas exploration and extraction has been moving into deeper and deeper waters, and offshore structures are being designed for operation at a stationary position, in water depths exceeding 1,000 meters. Examples of such designs include large volume gravity platforms, Tension-Leg Platforms (TLP's), Semi-Submersibles and large Spar Buoys. They are operated in hostile weather environments and over periods which may exceed two decades. This part aims the development of an efficient and accurate numerical method for the design of such offshore structures.

The theoretical approach to the linear wave loads and responses of realistic offshore structures has reached a mature state and some existing computational codes, like WAMIT, are widely used by the oil industries. However, the nonlinear loads and responses in the design of large volume offshore structures play an increasingly important role, and the theoretical status is not much matured yet.

Nonlinear surface wave effects can be divided into two distinct categories, low and high frequencies. Low-frequency effects dictate the slow drift response of compliant structures restrained by weak restoring mechanisms. Its natural period is of the order of minutes, and the quadratic wave effects are dominant. Many researches have carried out for the quadratic wave effects on the slow response of the offshore

structures, and some significant works were done by Korsmeyer, et al [39], Chen, et al [8], Emmerholf & Sclavounos [13] and Lee & Newman [43].

High frequency nonlinear wave effects are more complex than low frequency effects. They are responsible for the excitation of the high-frequency response of the offshore structure and its subsystems in flexural modes with resonant periods of the order of a few seconds. The flexural vibration of the tethers of a TLP and the transverse oscillation of a large volume gravity platform are good examples. Unlike their low-frequency counterpart, high frequency wave effects are not merely of quadratic nature. Sclavounos [70] showed that, in random waves of modest steepness, that second and third order effects are equally important and both may contribute to the springing excitation of the TLP tether response. In steep ambient waves, TLP's are also known to manifest a ringing response which is attributed to nonlinear effects potentially of higher order than third. Even though several studies have considered the analytical and numerical aspects of this problem, like M.H. Kim [27], the modeling and simulation of these phenomena remains a challenging topic.

The present study aims the time simulation of the second-order high-frequency wave loads. Since the frequency-domain method depends critically upon the proper discretization of the free surface for the accurate evaluation of slowly convergent infinite integrals, the time-domain method may circumvent these difficulties and make the direct simulation possible with realistic sea spectra.

The present work is based on the Rankine panel method. After the pioneering work of Hess and Smith [21], there were many studies on the application of panel method to the water wave problems, particularly for the wave resistance problem. Gadd [20] and Dawson [11] deserve to get a credit as pioneers in this field. After their works, many variations of panel method have been developed. In particular, Sclavounos and Nakos [69] proposed a method using B-spline function under the thorough theoretical study. Based on their stability analysis, further developments were continued for the ship motion [49] and the transient wave problems [50] [51]. The present work follows their work for the zero-speed solution of the linear and

high-frequency second-order problem around a single and multiple truncated circular cylinders.

Panels are distributed over the body surface and an annular domain over the mean position of the free surface. The linear and second-order free-surface conditions are stated in terms of a pair of unknowns, the velocity potential and free surface elevation. The radiation condition is enforced by the introduction of an annular artificial beach, the location and extent of the artificial beach are selected to minimize the reflection of the energy back towards the body boundary. The Laplace equation in the fluid domain is enforced by the application of the Green's theorem using the Rankine source as the Green function. This computational set-up allows the solutions of the linear, second or higher-order problems.

The present work includes the rational numerical analysis which ensures that the wave disturbance propagates over the free surface panel mesh in a stable manner and with little reflection from the beach. The time-stepping scheme is selected after a rational stability analysis along the lines of Sclavounos & Nakos [69] and Nakos [51]. A discrete dispersion relation is obtained and a stability condition is derived which offers valuable guidance towards the selection of a neutrally stable time-integration scheme with very desirable properties. As with most time-domain Rankine free surface panel methods, the use of filtering is necessary for the removal of the panel-scale saw-tooth oscillatory error. Several filtering schemes are tested and the best one is selected.

Simulations of the linear and second-order hydrodynamic forces on bottom-mounted and truncated circular cylinders are presented and compared to benchmark computations. Frequency domain forces are obtained from a single record by Fourier analysis, illustrating the very desirable attribute of the time domain method that a single force record contains information across the frequency range, if the incident wave record is properly selected.

The computation is extended to irregular waves. Realistic ocean wave can be expressed as a superposition of a large variety of waves with different frequencies, amplitudes, and phases. The direct time simulation of irregular waves removes several

of the complexities associated with the treatment of low- and high-frequency nonlinear wave-body interactions in the frequency domain. The present method allows the simultaneous solutions of the linear, second-order problems in random wave record, therefore permitting the direct generation of force and response records for use in design. The computation of the time consuming QTF matrices in the frequency domain is circumvented and the alternative solution of the second-order free surface problems in the time domain is carried out efficiently. As the first step towards realistic ocean spectra, the present thesis shows a bench mark test for the waves with multi-component waves.

In chapter 2 of this part, the boundary value problems of interest are formulated with basic assumptions. The numerical method is described in chapter 3. The detailed explanations about spatial discretization and time integration are in this chapter, and a thorough stability analysis is carried out to observe the consistency and temporal stability of the numerical scheme. Chapter 4 introduces the computational results. This include the results of parametric study and wave profile around a body as well as the linear and second-order hydrodynamic forces in a monochromatic wave or multi-frequency waves. Chapter 5 summarizes the present work.

# Chapter 2

# Boundary Value Problems

Consider the coordinate system and a floating body illustrated in Figure 2-1. Assuming ideal flow, the total velocity potential, $\phi$, is governed by the Laplace equation in the fluid domain. For a sufficiently small ambient wave steepness, the following perturbation expansion for the velocity potential and wave elevation is postulated,

$$\phi = \phi_1 + \phi_2 + .... \tag{2.1}$$

$$\eta = \eta_1 + \eta_2 + .... \tag{2.2}$$

where the subscript $k$ denotes the $k$-th order term. Upon the substitution of equation (2.1) and (2.2) into the exact kinematic and dynamic conditions, the linear and second-order free surface conditions are obtained in terms of the velocity potential and wave elevation.

Then the boundary value problems of the linear and second-order problem can be written as follows :

Linear Problem

- Fluid domain,

$$\nabla^2\phi_1 = 0 \tag{2.3}$$

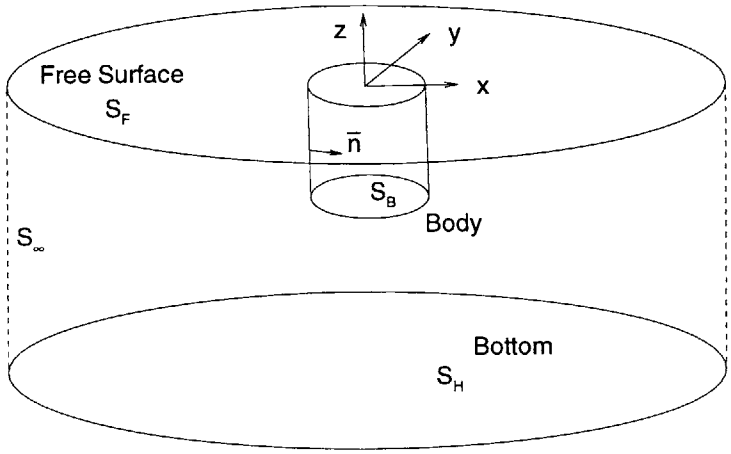


Figure 2-1: Coordinate System

- Free surface, $S_F(z=0)$,

$$\frac{\partial \phi_1}{\partial t} + g\eta_1 = 0 \tag{2.4}$$

$$\frac{\partial \eta_1}{\partial t} - \frac{\partial \phi_1}{\partial z} = 0, \tag{2.5}$$

- Body surface, $S_B$,

$$\frac{\partial \phi_1}{\partial n} = \begin{cases} \frac{\partial \vec{\xi}}{\partial t} \cdot \vec{n} & \text{for radiation problem} \\ 0 & \text{for diffraction problem} \end{cases} \tag{2.6}$$

- Bottom surface, $S_h(z=-h)$,

$$\frac{\partial \phi_1}{\partial z} = 0 \tag{2.7}$$

Second-Order Problem

- Fluid domain,

$$\nabla^2\phi_2 = 0 \tag{2.8}$$

- Free surface, $S_F(z=0)$,

$$\frac{\partial\phi_2}{\partial t} + g\eta_2 = -\frac{1}{2}\nabla\phi_1\cdot\nabla\phi_1 - \eta_1\frac{\partial^2\phi_1}{\partial z\partial t} \equiv f_1 \tag{2.9}$$

$$\frac{\partial\eta_2}{\partial t} - \frac{\partial\phi_2}{\partial z} = -\nabla\phi_1\cdot\nabla\eta_1 + \eta_1\frac{\partial^2\phi_1}{\partial z^2} \equiv f_2, \tag{2.10}$$

- Body surface, $S_B$, for diffraction

$$\frac{\partial\phi_2}{\partial n} = 0. \tag{2.11}$$

- Bottom surface, $S_h(z=-h)$,

$$\frac{\partial\phi_2}{\partial z} = 0 \tag{2.12}$$

In addition the radiation condition should be imposed. The body boundary condition is applied on the mean position of the body. In the present study, the second-order radiation problem is out of interest.

In the diffraction problem, the velocity potential and wave elevation can be separated as the incident wave and perturbed components. In the linear problem, considering the random ambient wave, the incident wave can be expressed as a superposition of a large variety of waves such that

$$\phi_{I,1} = \sum_{m=1}^{M} \Re\{\frac{igA_m}{\omega_m}\frac{\cosh k_m(z+h)}{\cosh k_m h}\, e^{-ik_m\cos\beta_m x - ik_m\sin\beta_m y + \omega_m t + i\theta_m}\} \tag{2.13}$$

where $A_m, \omega_m, k_m, \beta_m, \theta_m$ are the amplitude, frequency, wave number, heading angle, and phase of the $m$-th component, respectively. Besides $h$ is the water depth. When the wave is long-crested, $\beta_m$ are the same. The second-order incident wave takes the

following form:

$$\phi_{I,2} = \sum_{l=1}^{M} \sum_{m=1}^{M} \Re\{\phi_{I,2}^{+} \, e^{i(\omega_l+\omega_m)t} + \phi_{I,2}^{-} \, e^{i(\omega_l-\omega_m)t}\} \tag{2.14}$$

where $\phi_{I,2}^{+}, \phi_{I,2}^{-}$ is referred as the complex sum- and difference-frequency components of the second-order incident potential.

The hydrodynamic forces acting on the body are obtained by integrating the linear and second-order pressure over the wetted body surface. This leads to the definitions of the linear and second-order forces,

$$\vec{F}_1 = -\rho \int\int_{S_B} (\frac{\partial \phi_1}{\partial t}) \vec{n} ds \tag{2.15}$$

$$\vec{F}_2 = \vec{F}_q + \vec{F}_p \tag{2.16}$$

where

$$\vec{F}_q = -\rho \int\int_{S_B} (\frac{1}{2} \nabla\phi_1 \cdot \nabla\phi_1) \vec{n} ds + \frac{1}{2} \rho g \oint_{wl} \eta_1^2 \vec{n} dl \tag{2.17}$$

$$\vec{F}_p = -\rho \int\int_{S_B} (\frac{\partial \phi_2}{\partial t}) \vec{n} ds \tag{2.18}$$

Here, $\rho, g, \vec{n}$ are the fluid density, gravitational acceleration, and normal vector on the body surface. Moreover, $\oint_{wl}$ denotes the contour integral along the body waterline on the $z = 0$ plane. In the second-order force, $\vec{F}_q$ is a contribution from the linear solution, while $\vec{F}_p$ comes from the pure second-order potential.

# Chapter 3

# The Numerical Method

## 3.1 Rankine Panel Method

The present study adapts the Rankine panel method developed by Sclavounos and Nakos [69], Nakos, Sclavounos, & Kring [50], Kring [42] for the treatment of the ship seakeeping problem. In this method, Rankine panels are distributed over the body boundary and a domain of finite extent on the z=0 plane. Both the velocity potential and wave elevation are retained as unknowns and discretized by adopting a bi-quadratic B-spline variation over the panel surface which maintains continuity of both unknowns across panels.

The velocity potential, free surface elevation, and normal velocity at $\vec{X}_i = (x_i, y_i, z_i)$ are approximated as,

$$\begin{pmatrix} \phi \\ \eta \\ \phi_n \end{pmatrix} (\vec{X}_i, t) \simeq \sum_j \begin{pmatrix} \phi \\ \eta \\ \phi_n \end{pmatrix}_j (t)\ B_j(\vec{X}_i) \equiv \sum_j \begin{pmatrix} \phi \\ \eta \\ \phi_n \end{pmatrix}_j (t)\ B_{ij}, \tag{3.1}$$

where $B_j$ is a B-spline basis function with respect to the local coordinate system, $(\hat{x}, \hat{y})$.

The B-spline basis function of the $(p, q)$-th order can be written as

$$B^{(p,q)}(\hat{x}, \hat{y}) = b^{(p)}(\hat{x}) b^{(q)}(\hat{y}) \tag{3.2}$$

where

$$b^{(p)}(\hat{x}) = \frac{1}{\Delta \hat{x}} \int_{-\infty}^{\infty} b^{(p-1)}(\xi) b^{(0)}(\hat{x} - \xi)\, d\xi \tag{3.3}$$

and

$$b^{(0)}(\hat{x}) = \begin{cases} 1, & |\hat{x}| \leq \Delta \hat{x}/2 \\ 0, & |\hat{x}| > \Delta \hat{x}/2 \end{cases} \tag{3.4}$$

where $\Delta \hat{x}$ is the panel size in the local coordinate system.

Basically, any order can be selected for the basis function. However, since the second-order free surface boundary conditions require the second-order differential terms, it is not desirable to choose $p$ and $q$ less than 2. One distinctive advantage of the higher-order discretization is the analytic treatment of a lower-order differential term. On the other hand, the number of neighbor panels increases when the order of basis function becomes large, and this requires more complicated numerical treatment. Therefore, the present study applies the bi-quadratic basis function, and this discrete approximation provides the convergence of the numerical method which will be mentioned later. The bi-quadratic basis function is written as,

$$B_j = b^{(2)}(\hat{x}) b^{(2)}(\hat{y}), \tag{3.5}$$

with

$$b^{(2)}(s) = \begin{cases} \frac{1}{2\Delta \hat{S}^2}(s + \frac{3\Delta \hat{S}}{2})^2, & -\frac{3\Delta \hat{S}}{2} < s \leq -\frac{\Delta \hat{S}}{2} \\ \frac{1}{\Delta \hat{S}^2}(-s^2 + \frac{3\Delta \hat{S}^2}{4}), & -\frac{\Delta \hat{S}}{2} < s \leq \frac{\Delta \hat{S}}{2} \\ \frac{1}{2\Delta \hat{S}^2}(-s + \frac{3\Delta \hat{S}}{2})^2, & \frac{\Delta \hat{S}}{2} < \hat{S} \leq \frac{3\Delta \hat{S}}{2} \end{cases} \tag{3.6}$$

This function introduces the coupling of the unknowns with their value over the 8 neighboring panels.

Applying the Green's identity over the body surface, $S_B$, and the mean position of the free surface, $S_F$ ($z = 0$ plane), and substituting the discretization (3.1) of the velocity potential and the wave elevation, the following system of equations is obtained,

$$(\phi_k)_j^{n+1} B_{ij} \quad + \quad (\phi_k)_j^{n+1} \int\int_{S_B \cup S_F} B_{ij}(\vec{\zeta}) \frac{\partial}{\partial n} G(\vec{X}_i; \vec{\zeta}) d\zeta \\ - \; (\frac{\partial \phi_k}{\partial n})_j^{n+1} \int\int_{S_B \cup S_F} B_{ij}(\vec{\zeta}) G(\vec{X}_i; \vec{\zeta}) d\zeta = 0, \qquad (3.7)$$

where $G(\vec{X}_i; \vec{\zeta})$ is the Rankine source potential defined by $G(\vec{X}_i; \vec{\zeta}) = 1/2\pi |\vec{X}_i - \vec{\zeta}|$ and the summation notation is understood over the index $j = 1, ..., N$ where $N$ is the total number of panels. The subscript $k$ denotes the problem order, i.e. $k = 1$ for linear and $k = 2$ for second order, and the index $i$ denotes the field or collocation point where the integral equation is enforced, with $i = 1, ..., N$. Finally the superscript $n+1$ denotes the value of the respective quantity at the $(n+1)$th time step.

Equation (3.7) is a linear system of equations which relates the velocity potential to its normal derivative over the domain boundaries at the $(n+1)$th time step. Over the body boundary, the normal derivative is known and $\phi^{n+1}$ is unknown. Over the $z = 0$ plane, the normal derivative $\phi_z^{n+1}$ is the unknown, while the velocity potential is known in terms of its value at the previous time steps obtained from the discretization of the free surface conditions.

The discretized forms of the free-surface boundary conditions are

$$\frac{(\phi_k)_j^{n+1} - (\phi_k)_j^n}{\Delta t} B_{ij} + g(\eta_k)_j^{n+1} B_{ij} \quad = \quad \delta_{2,k} (f_1)_j^{n+1} \qquad (3.8)$$

$$\frac{(\eta_k)_j^{n+1} - (\eta_k)_j^n}{\Delta t} B_{ij} - (\frac{\partial \phi_k}{\partial z})_j^n B_{ij} \quad = \quad \delta_{2,k} (f_2)_j^{n+1}, \qquad (3.9)$$

where $\delta_{2,k}$ is a delta function which takes the value of zero for $k = 1$ and the value of one for $k = 2$. In addition $\Delta t$ is the time step.

The elimination of the wave elevation between equations (3.8) and (3.9) leads to an explicit relation of the velocity potential $\phi^{n+1}$ at the $(n+1)$th time step to the potential and the normal derivative at the $n$th time step. Therefore, at the $(n+1)$th time step the unknowns are the potential over the body boundary and its normal derivative over the $z = 0$ plane, which are determined upon solving the linear system of equation, (3.7). The wave elevation $\eta^{n+1}$ then follows from equation (3.9) and the velocity potential over the free surface at the subsequent $(n+2)$th time step from equation (3.8).

The forcing functions of the linear problem are zero, while its second order counterparts $f_i$ are finite and a function of the linear solution which should be determined before solving of the second-order problem.

For the finite depth problem, the additional panels are distributed on the bottom surface, $S_h$, and normal flux is set to be zero.

## 3.2 Stability Analysis

The theoretical justification of a numerical method can be achieved by the stability analysis. There are two issues in the stability analysis. One is consistency, and the other is temporal stability. The proof of consistency indicates that the discrete numerical solution approaches the continuous solution when the spatial and temporal discretizations go to zero. In a wave problem, the dispersion relation can be observed in order to check the consistency. Temporal stability analysis offers a certain condition or absolute stability/instability of the selected time-integration scheme. By the Dahlquist equivalent theorem, a linear numerical scheme is convergent if and only if it is consistent and stable.

The stability analysis of Sclavounos & Nakos [69] and Nakos [50] for the forward-speed ship wave problem is applicable to the zero speed problem as well. Consider the evolution of a surface wave disturbance in the absence of a body over the rectangular panel mesh illustrated in Figure 3-1.

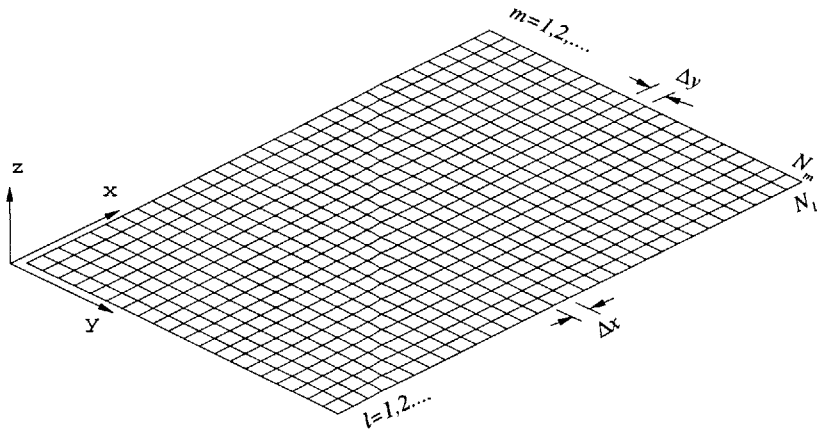


Figure 3-1: Rectangular panels on free surface for stability analysis

From the Green's theorem, the velocity potential and its normal derivative over the free surface are related by the expression,

$$\phi_k(\vec{X}_i) - \int\int_{S_F} \frac{\partial}{\partial z}\phi_k(\vec{\zeta})G(\vec{X}_i;\vec{\zeta})d\zeta = R(\vec{X}_i) \tag{3.10}$$

where $R(\vec{X}_i)$ is the forcing term corresponding to the linear or second-order excitation of the free surface conditions, equation (3.8) and (3.9).

Introducing the discrete Fourier transform of the function, $f(l\Delta x, m\Delta y, n\Delta t)$, the values of which are known at the spatial location, $x = l\Delta x, y = m\Delta y$, and at the time step, $t = n\Delta t$,

$$\tilde{f}(u,v,\omega) = \Delta x\Delta y\Delta t \sum_{l=0}^{N_l}\sum_{m=0}^{N_m}\sum_{n=0}^{N_n} f(l\Delta x, m\Delta y, n\Delta t)e^{i(ul\Delta x + vm\Delta y - \omega n\Delta t)} \tag{3.11}$$

the inverse transform becomes,

$$\begin{aligned} &f(l\Delta x, m\Delta y, n\Delta t) \;=\\ &\frac{1}{(2\pi)^3}\int_{-\pi/\Delta t}^{\pi/\Delta t}\int_{-\pi/\Delta x}^{\pi/\Delta x}\int_{-\pi/\Delta y}^{\pi/\Delta y} \tilde{f}(u,v,\omega)\; e^{-i(ul\Delta x + vm\Delta y - \omega n\Delta t)}d\omega du dv. \end{aligned} \tag{3.12}$$

Then the Fourier transforms of the integral equation (3.10) and the free surface

conditions (3.8), (3.9) have the following forms:

$$\tilde{\phi}\tilde{B} - \tilde{\phi}_z\tilde{S} = \tilde{R} \tag{3.13}$$

$$\frac{\mathrm{Z}-1}{\Delta t}\tilde{\phi}\tilde{B} + g\mathrm{Z}\tilde{\eta}\tilde{B} = \tilde{f}_1 \tag{3.14}$$

$$\frac{\mathrm{Z}-1}{\Delta t}\tilde{\eta}\tilde{B} - \tilde{\phi}_z\tilde{B} = \tilde{f}_2 \tag{3.15}$$

where Z is the complex function $\mathrm{Z} = e^{i\omega\Delta t}$, and $\tilde{B}, \tilde{f}_1, \tilde{f}_2$, and $\tilde{R}$ are the discrete Fourier transforms for $B_{ij}, f_1, f_2$, and $R$, respectively. In addition $\tilde{S}$ is the discrete Fourier transform of $S_{ij}$,

$$S_{ij} = \int\int_{S_F} B_{ij}(\vec{\zeta})G(\vec{X}_i;\vec{\zeta})d\zeta. \tag{3.16}$$

The integral limit of the potential comes from the consideration of the aliasing theorem and from the selection of integration contour for the inverse that includes all singularities in the dispersion equation. The Fourier transforms of $B$ and $S$ for the general order of the basis function are written with the form :

$$\tilde{B} = \Delta x\Delta y \sum_{m=-\infty}^{\infty}\sum_{l=-\infty}^{\infty} \frac{\sin^{p+1}(\hat{u}\pi + m\pi)\ \sin^{q+1}(\hat{v}\pi + l\pi)}{(\hat{u}\pi + m\pi)^{p+1}\ (\hat{v}\pi + l\pi)^{q+1}} \tag{3.17}$$

$$\begin{aligned}\tilde{S} &= \frac{\Delta x^2\Delta y}{2\pi} \times \\ &\sum_{m=-\infty}^{\infty}\sum_{l=-\infty}^{\infty} \frac{\sin^{p+1}(\hat{u}\pi + m\pi)\ \sin^{q+1}(\hat{v}\pi + l\pi)}{(\hat{u}\pi + m\pi)^{p+1}\ (\hat{v}\pi + l\pi)^{q+1}\sqrt{(\hat{u}+m)^2 + \alpha^2(\hat{v}+l)^2}}\end{aligned} \tag{3.18}$$

where $\hat{u} = u\Delta x/2\pi, \hat{v} = v\Delta y/2\pi$, and $\alpha = \Delta x/\Delta y$.

The discrete potential, $\phi(l\Delta x, m\Delta y, n\Delta t)$, can be obtained by eliminating $\tilde{\phi}_z$ and $\tilde{\eta}$ from equation (3.13) to (3.15),

$$\phi_k(l\Delta x, m\Delta y, n\Delta t) = \frac{1}{(2\pi)^3}\int_C\int_{-\infty}^{\infty}\int_{-\infty}^{\infty}\frac{\tilde{R}_k}{\tilde{W}}e^{-i(ul\Delta x + vm\Delta y - \omega n\Delta t)}d\omega du dv, \tag{3.19}$$

where

$$\tilde{R}_k = \delta_{2,k}(\mathrm{Z}-1)\Delta t\tilde{S}\tilde{f}_1 + \tilde{B}\Delta t^2 gZ\tilde{R} - \delta_{2,k}\Delta t^2 gZ\tilde{f}_2 \tag{3.20}$$

$$\tilde{W} = (\mathrm{Z}-1)^2\tilde{B}\tilde{S} + g\mathrm{Z}\Delta t^2\tilde{B}^2. \tag{3.21}$$

$\tilde{W} = 0$ contains the dispersion relation of this discrete system. In a non-dimensional form, the discrete dispersion relation can be written as follows :

$$\mathrm{Z}^2 - (2 - \frac{S_o}{\beta^2})\mathrm{Z} + 1 = 0, \tag{3.22}$$

where $\beta = \sqrt{\Delta x/g\Delta t^2}$ and $S_o(\hat{u},\hat{v}) = \Delta x\tilde{B}/\tilde{S}$.

If the numerical method has the consistency, $\tilde{W}$ must recover the continuous dispersion relation, $W$,

$$W = \omega^2 - g\sqrt{u^2+v^2} = 0 \tag{3.23}$$

The consistency of the discrete dispersion relation can be examined through an asymptotic expansion of $\tilde{B}/\tilde{S}$. When $\Delta x, \Delta y \to 0$, a series expansion of $\tilde{B}/\tilde{S}$ becomes,

$$\begin{aligned}\frac{\tilde{B}}{\tilde{S}} &= \frac{1}{\sqrt{u^2+v^2}} + \frac{(-1)^{p+1}\Delta s(v\Delta s)^{q+1}}{(v\Delta s+2\pi)^{q+1}\sqrt{(u\Delta s)^2+(v\Delta s+2\pi)^2}} \\ &+ \frac{(-1)^{q+1}\Delta s(u\Delta s)^{p+1}}{(u\Delta s+2\pi)^{p+1}\sqrt{(u\Delta s+2\pi)^2+(v\Delta s)^2}} \\ &+ \frac{(-1)^{p+q+2}\Delta s(u\Delta s)^{p+1}(v\Delta s)^{q+1}}{(u\Delta s+2\pi)^{p+1}(v\Delta s+2\pi)^{q+1}\sqrt{(u\Delta s+2\pi)^2+(v\Delta s+2\pi)^2}} \\ &+ O(\Delta s^{p+q+3})\end{aligned} \tag{3.24}$$

where $\Delta s = O(\Delta x, \Delta y)$.

When $p = q$, it can be simplified as

$$\frac{\tilde{S}}{\tilde{B}} = \sqrt{u^2 + v^2} + O(\Delta s^{p+2}). \tag{3.25}$$

so that, as $\Delta t \to 0$, the discrete dispersion relation recovers the familiar continuous limit,

$$\tilde{W} = W + O\{\Delta s^{p+3}, \Delta t\} = 0. \tag{3.26}$$

This result proves that the present numerical scheme for time integration has the consistency for any order of the basis function. In particular, when the bi-quadratic spline is applied, the accuracy of the dispersion relation is of fifth order in panel size, and the major source of numerical error comes from the temporal discretization.

Figure 3-2 shows a comparison of the continuous and discrete dispersion relations for $\alpha = 1.0$ and $v = 0$, which shows a favorable agreement. As the time step, $\Delta t$, becomes larger for a fixed $\hat{u}$, the numerical error increases. When $\beta$ is 0.7, the discrete system becomes unstable at a certain $\Delta t$ and $\Delta x$.

An important property of the discrete dispersion relation is found at $u\Delta x/2\pi = 0.5$, which the wavelength is exactly two panels long. The slope of the discrete dispersion relation goes to zero at this point, and this indicates a zero group velocity. This produces the growth of a short wave length error, which is known as the Nyquist saw-tooth wave. External forcing will cause these short wavelength errors to grow since a zero group velocity means no energy can be radiated away. To prevent this type of instability, a low-pass spatial filter must be applied.

The condition of temporal stability follows from the discrete dispersion relation, equation (3.22). When the root of equation (3.22) is on a unit circle, the scheme becomes neutrally stable, and the condition for neutral stability becomes

$$\beta \geq \frac{\sqrt{S_o(\hat{u}, \hat{v})}}{2}. \tag{3.27}$$

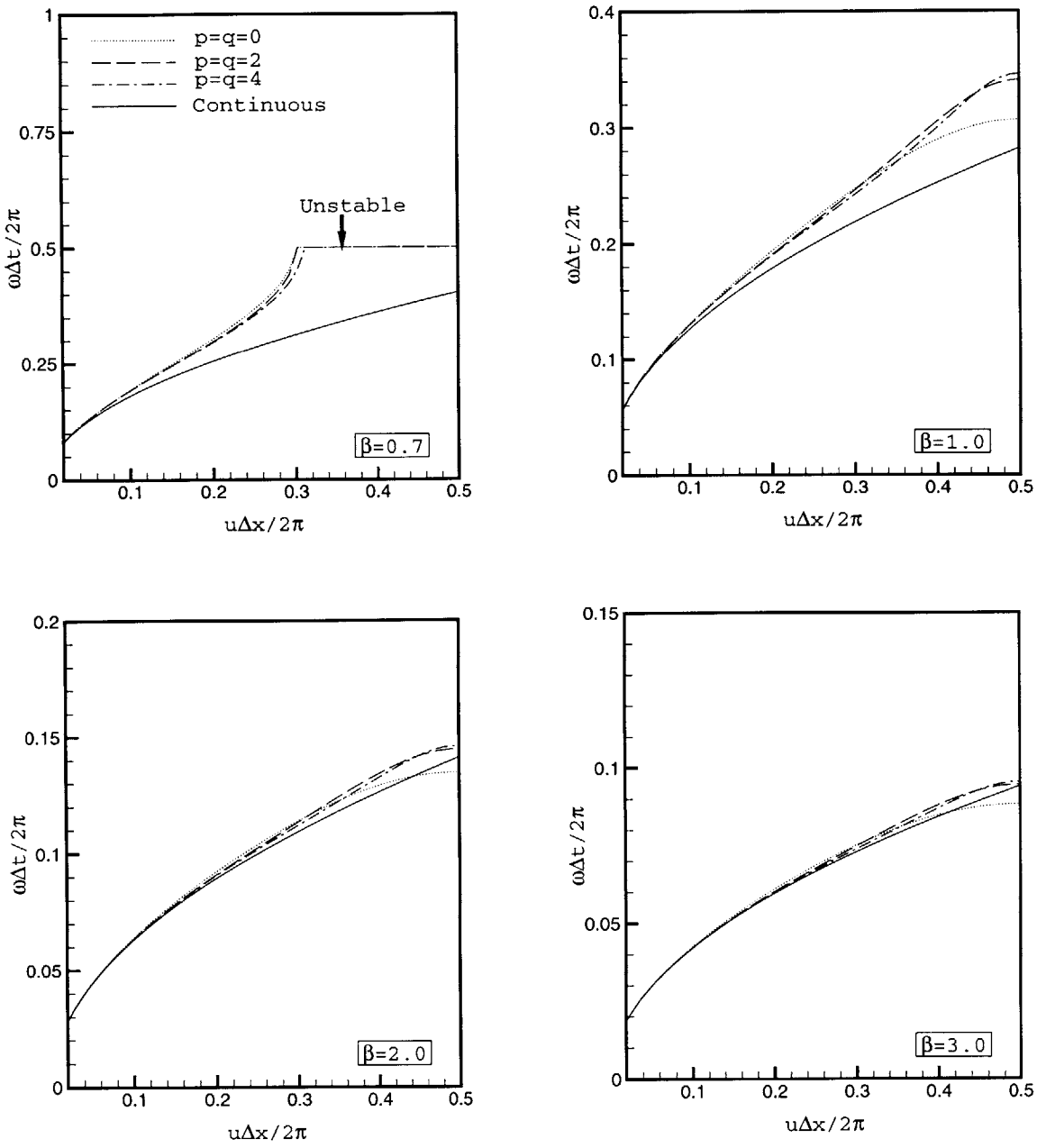


Figure 3-2: Comparison of dispersion relation for the different order of basis function, $\alpha = 1.0, \beta = 1.0$

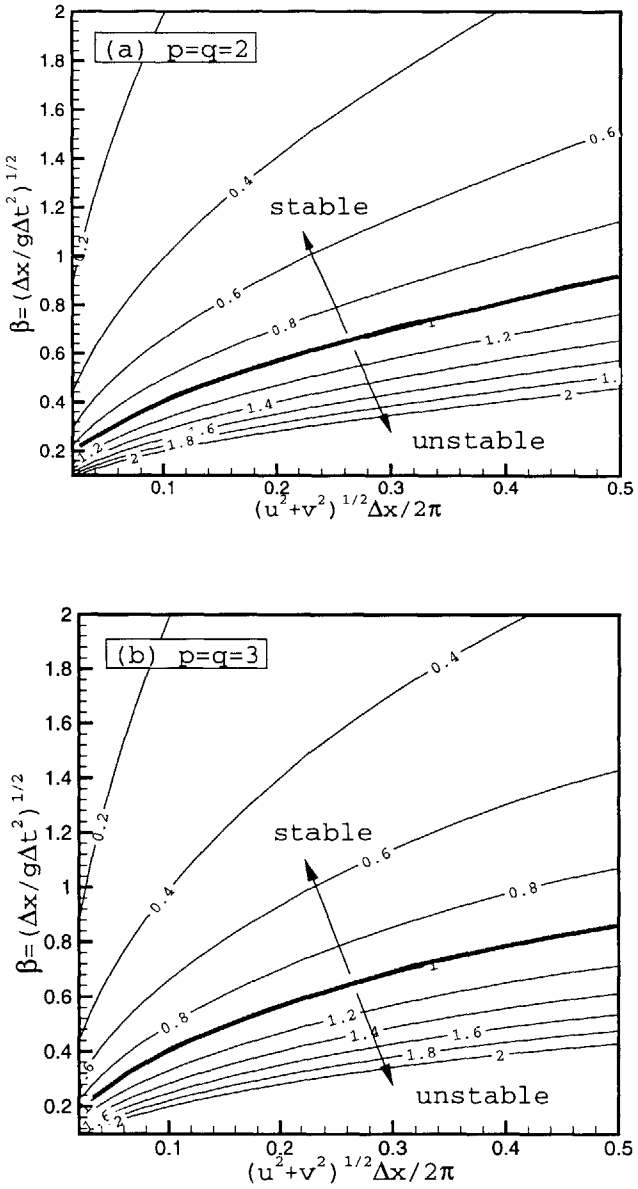


Figure 3-3: Contour plot of $S_o/4\beta^2$ and stability zone, $\alpha = 1.0$, $u = v$

Therefore, if this condition is satisfied, the present numerical method is consistent, neutrally stable, and sufficient for the solution of the continuous boundary value problem originally posed.

The limit behavior is of interest when the space segment approaches zero. Using the limit case of equation (3.25), it is simple to show that the neutral stability condition becomes

$$\Delta t^2 \leq \frac{4}{g\sqrt{u^2+v^2}} \tag{3.28}$$

This condition says that the time segment must be inversely proportional to the square root of the wave number. Therefore, the maximum $\Delta t$ becomes

$$\Delta t^2_{max} \leq \frac{4\Delta s}{\pi g} \tag{3.29}$$

so that the time segment also approaches zero as $\Delta s$ goes to zero.

Figure 3-3 shows the contour plot of $S_o/2\beta^2$ when $\alpha = 1.0$ and $u = v$. The boundary of stability zone is a line such that $\sqrt{S_o}/2\beta = 1$. The stability zones for the bi-quadratic and bi-cubic basis functions have minor difference. Based on Figure 3-2 and this figure, the basis function higher than bi-quadratic doesn't offer a significant improvement for numerical stability.

## 3.3 Wave Absorbing Zone

This study adopts a wave absorption zone to satisfy the radiation condition (Figure 3-4). The numerical implementations of this concept can be found in the work of Baker et al. [5] and Cointe [10]. This method is intended to minimize the reflection at the truncated boundary by absorbing outgoing waves which travel through the absorption zone. The design of this artificial zone must be considered in terms of its damping parameters, such as its size, strength, and the distance from the body where the wave-absorbing zone starts.

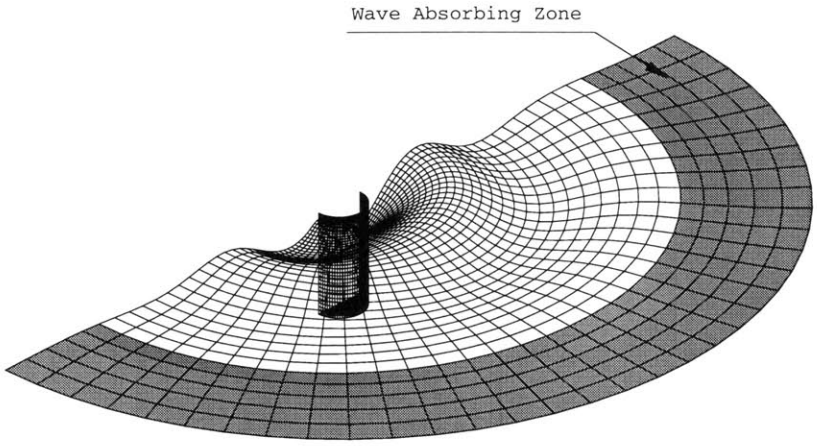


Figure 3-4: Application of the artificial wave absorbing beach

Consider the following linearized kinematic condition in the wave-absorbing zone,

$$\frac{\partial \eta_1}{\partial t} - \frac{\partial \phi_1}{\partial z} + \mu_1(r)\eta_1 + \frac{\mu_2(r)}{g}\phi_1 = 0. \tag{3.30}$$

A extra term, $\mu_1(r)\eta_1$, is a type of Newtonian cooling or mass flux through the surface that is proportional to the wave elevation. The other additional term, $\frac{\mu_2(r)}{g}\phi_1$, is similar to the Rayleigh viscosity and acts as a sponge that modifies the dispersion of the wave. In Appendix D, numerical tests are introduced for some different choices of damping mechanism, and it is obvious that the adoption of $\mu_2(r)$ provides better result.

Putting $\phi_1 = Re\{\Psi_1(x, y, z)e^{i\omega t}\}$, the kinematic condition becomes,

$$g\frac{\partial \Psi_1}{\partial z} + \{-\omega^2 + i\omega\mu_1(r) - \mu_2(r)\}\Psi_1 = 0. \tag{3.31}$$

If $\mu_1(r), \mu_2(r)$ are assumed to be constants, the dispersion relation for infinite depth becomes

$$\omega = \frac{i\mu_1 \pm (-\mu_1^2 + 4gk - 4\mu_2)^{1/2}}{2}. \tag{3.32}$$

The imaginary term contributes to the wave damping, thus $\mu_1$ will be the damping parameter as long as $\mu_1^2 < 4gk + 4\mu_2$. It should be noted that the dispersion property of the waves is affected by the Newtonian cooling. To offset this dispersion, the damping parameters, $\mu_1$ and $\mu_2$, may be selected to satisfy the relationship

$$\mu_2 = -\frac{\mu_1^2}{4}. \tag{3.33}$$

It is desirable for the damping parameters to vanish at the inner edge of the zone and increase slowly towards the outer edge. If there is a sudden change of the free surface boundary conditions at the beginning of the wave absorbing zone, a reflection may be caused at the edge.

When the damping parameters are not constant across the zone, an analytic treatment of the change in dispersion is difficult. However, computational testing indicates that the results of equation (3.33) are still applicable. In this study, a quadratic taper is used for $\mu_1$,

$$\mu_1 = 3\mu_o \frac{(r - r_o)^2}{L^3} \tag{3.34}$$

which satisfies $\int_L \mu_1 dr = \mu_o$, where $\mu_o$ is a constant, called the beach strength, and $L$ is the zone size.

The effect of the wave-absorbing zone on the second-order problem follows from the linear theory since the dispersion characteristics are the same in deep water. In practice, if the wave absorbing zone for the second-order problem overlaps with that of the linear problem, there will be some interference since the linear solution will already contain the effect of its own numerical beach.

## 3.4 Conversion to Frequency Domain

The time domain solution produces a force record that can be converted to the frequency domain through a Fourier transform. A Fast Fourier Transform (FFT) was

not used in this study since the component frequencies are a function of the time interval and will not be easily applicable to arbitrary, unequal frequency intervals. However, since the underlying frequency components are given with the forcing, a similar method can be used.

If a time-dependent function, $f(t)$, is written as the following form :

$$f(t) = A_o + \sum_{n=1}^{N} A_n e^{i\omega_n t}, \tag{3.35}$$

a direct integration of the Fourier series should satisfies

$$\int_{t_2}^{t_1} f(t) e^{i\omega_m t} dt = A_o \sum_{n=1}^{N} \int_{t_2}^{t_1} e^{i\omega_m t} dt + \sum_{n=1}^{N} A_n \int_{t_2}^{t_1} e^{i\omega_n t} e^{i\omega_m t} dt \tag{3.36}$$

where $\omega_n$ is a basis frequency of $f(t)$ with a complex amplitude $A$, and $\omega_m$ is a test frequency.

Since the equation is valid for arbitrary test frequencies, there is no restriction on the selection of the basis and test frequencies. The substitution of $N + 1$ test frequencies including a steady component leads to a linear system of equations which determines $A_n$. The left-hand side can be evaluated by numerical integration. This provides an efficient Fourier transform for the given time record.

## 3.5 Spatial Filtering

It is shown that a saw-tooth wave may be generated in the discrete system. Spatial filtering schemes are widely used in time-domain wave problems in order to eliminate the spurious, saw-tooth waves. Shapiro [63] suggested a general filtering equation of the following form,

$$\bar{\eta}_j = \sum_{k=0}^{K} c_k (\eta_{j-k} + \eta_{j+k}), \tag{3.37}$$

where $K$ indicates the number of mesh points included in the filter, and $c_k$ is the weight for each point. Longuet-Higgins & Cokelet [45] have suggested two filtering equations with quadratic and cubic accuracy, and their 5-point filter is popular.

In the present computation, a 7-point filter is applied, and $c_0 = 0.3506, c_1 = 0.2306, c_2 = -0.1006, c_3 = 0.0194$ are selected to minimize the smoothing effect. The amplification factor of this scheme is

$$R = 0.7012 + 0.4612\cos(\frac{2\pi\Delta\hat{s}}{\lambda}) - 0.2012\cos(\frac{4\pi\Delta\hat{s}}{\lambda}) + 0.0388\cos(\frac{6\pi\Delta\hat{s}}{\lambda}) \quad (3.38)$$

where $\lambda$ is the wave length to be considered. The amplification factors for different filters are introduced in Appendix E. If the wave length is $2\Delta\hat{s}$, the amplification ratio becomes zero so the saw-tooth waves will be completely removed.

The application of filter results in some minor energy loss. It is desirable for a filter not to have much energy loss, and Nakos [50] showed that the amplification ratio of the present filter indicates less damping than other 5- and 7-point filters. In Appendix E, the smoothing effect by filters is described in detail.

An important side effect of the spatial filter is that it will also affect the non-wavelike free surface modes near the body. This error can be minimized if the spatial filter is not applied at every time step. If the filter is only applied periodically, the free surface near the body will have time to return to its equilibrium position. In the time record, this effect appears as an error spike. Since, the underlying numerical method is neutrally stable, this error spike quickly disappears within two to three time steps.

To quantify this side effect, the application of the filter can be viewed as an additional forcing term. Applying it to the potential and wave elevation yields, $\bar{\phi}_i^n = \phi_i^n + \epsilon_\phi$ and $\bar{\eta}_i^n = \eta_i^n + \epsilon_\eta$. The free surface boundary conditions become

$$\frac{(\phi_k)_j^{n+1} - (\phi_k)_j^n}{\Delta t} B_{ij} + g(\eta_k)_j^{n+1} B_{ij} = \delta_{2,k}(f_1)_j^{n+1} - (\epsilon_\phi^n/\Delta t)\delta_{n,NF} \quad (3.39)$$

$$\frac{(\eta_k)_j^{n+1} - (\eta_k)_j^n}{\Delta t} B_{ij} - (\frac{\partial\phi_k}{\partial z})_j^n B_{ij} = \delta_{2,k}(f_2)_j^{n+1} - (\epsilon_\eta^n/\Delta t)\delta_{n,NF} \quad (3.40)$$

where $NF$ is the time step interval or period at which the spatial filter is applied. Therefore, as $\Delta t$ decreases, this error spike becomes higher and narrower.

This side effect can be ignored by showing that the force record between applications of the filter is insensitive to the period. There will be a minimum period of application below which this error spike becomes significant. There is also a maximum period beyond which the spurious, saw-tooth oscillations become unstable. Numerical experience has shown that this bound is very broad and poses no difficulty in practice.

# Chapter 4

# Computational Results & Discussion

## 4.1 Solution Grid

The computational method has been applied to both truncated and bottom-mounted circular cylinders. Figure 4-1 shows the solution grid for a single bottom-mounted cylinder and the truncated 4 cylinders. The computational result may be influenced significantly by a grid system, and the choice of proper solution grids is essential. Since the radiation and diffraction potential have a source- or dipole-like behavior at far from the disturbance, a circular computational domain with a polar grid system is adopted in the present computation.

For the panel distribution on the free surface near a multi-cylinder array, the solution of a Poisson equation with negative exponential forcing provides a body-fitted mesh. This grid system allows for panel sizes that expand with distance from the body, which is necessary for computational efficiency, and it can be applied both to single vertical cylinders or to more general multi-body structures. Appendix F explains the generation of an elliptic grid system.

The second-order problem, with significant energy at wavelength shorter than the linear problem, requires a finer mesh resolution so that the number of panels become

much larger for the same computational domain. Fortunately the sum-frequency disturbance is localized near the body, and the computation domain may be smaller than the linear problem. In this viewpoint, two different mesh systems depending on the order of problem can be used in order to minimize the computational effort. In this case, an interpolation scheme transmits the linear solution from its large, coarse grid to the smaller, denser grid of the second-order problem.

In the simulation of random wave, the computational domain must cover the longest wave length, while the mesh size should be enough fine to resolve the shortest wave length. In particular, if the difference-frequency components as well as sum-frequency are supposed to be simulated, the computational domain depends on the smallest difference-frequency and the mesh size near the body depends on the largest sum-frequency. Figure 4-2 shows an example of computational domain and solution grids for random incident wave.

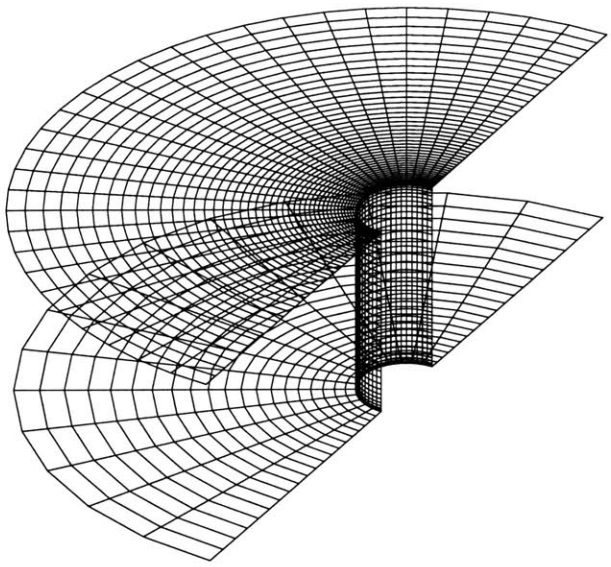

(a) Single Cylinder (half)

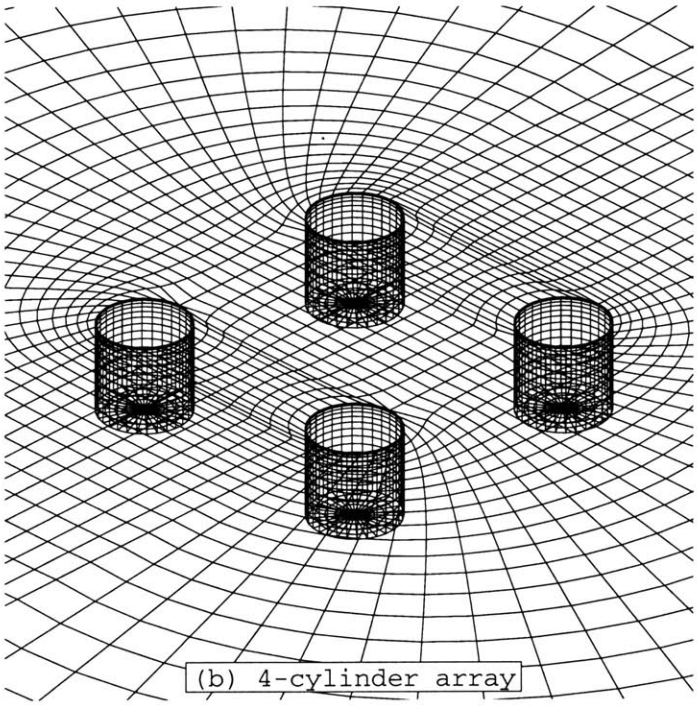


Figure 4-1: Solution grids : (a) a single bottom-mounted cylinder, (b) 4 truncated cylinder

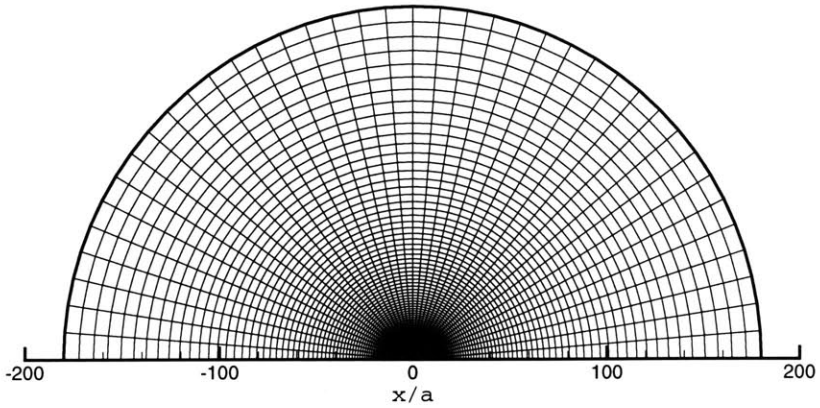


(a) Computational domain

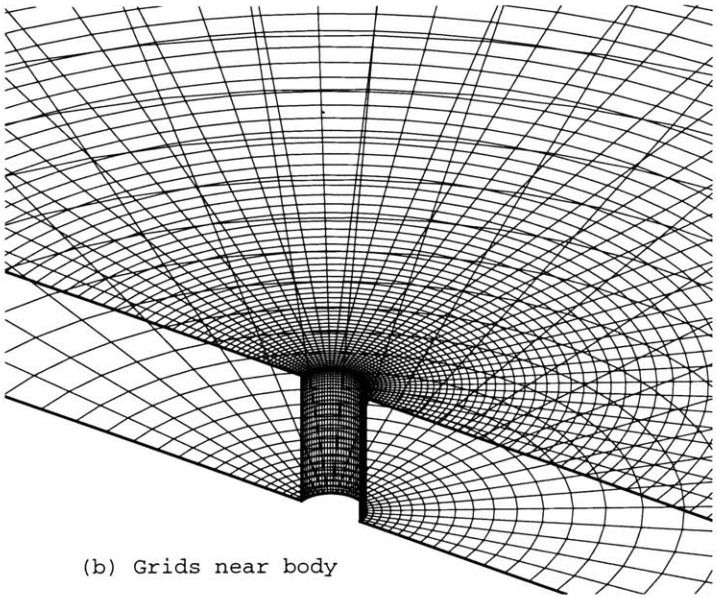

(b) Grids near body

Figure 4-2: Solution grids for random waves near a bottom-mounted cylinder (half) : (a) computational domain, (b) grids near the body

## 4.2 Wave Absorbing Zone

The role of the wave absorbing zone, is another critical numerical issue. If the damping mechanism is too weak or too strong, the outgoing waves may be reflected by the truncated boundary or the inner edge of the absorbing zone. Therefore it is necessary to examine the sensitivity of the results to the parameters of the zone.

To test this sensitivity, the flow is computed near a single, truncated, circular cylinder of diameter $D(=2a)$ and draft $d$. A quadratic taper for $\mu_1$ with $\mu_2 = -\mu_1^2/4$ is applied.

The rate of wave absorption for given zone parameters is related to the wave frequency. So, the strength of the zone, $\mu_1$, will be dictated by the highest expected frequencies, while, in general, the necessary length of the zone is dictated by the lowest frequencies. The optimal choice of the damping strength is related to the frequency, but a choice based upon the high frequencies will still be effective for lower frequencies. Therefore, the absorbing zone can damp a wide spectrum of wavelengths.

| $\omega$ | $R_{max}/D$ | $L/D$ | $R_{max}/\lambda_1$ | $A_{33}/(\rho\nabla)$ | $B_{33}/(\rho\nabla\sqrt{D/g})$ |
|---|---|---|---|---|---|
| 0.5 | 205.4 | 20.0 | 1.6 | 0.7316 | 0.2489 |
| | | 40.0 | 3.2 | 0.7315 | 0.2595 |
| | | 60.0 | 4.8 | 0.7315 | 0.2596 |
| 1.5 | 25.9 | 10.0 | 3.6 | 0.5391 | 0.0753 |
| | | 15.0 | 5.4 | 0.5392 | 0.0753 |
| | | 20.0 | 7.2 | 0.5392 | 0.0753 |

Table 4.1: The heave added mass ($A_{33}$) and damping coefficient($B_{33}$) for different lengths of the wave absorbing zone. : $a/d = 1.0, \mu_o = 3.0$. (WAMIT with same body grid : 0.7324, 0.2491 ($\omega(D/g)^{1/2} = 0.5$), 0.5420, 0.0749($\omega(D/g)^{1/2} = 1.5$) )

Figure 4-3 and 4-4 show the time history of the horizontal force acting on a truncated cylinder in a monochromatic wave. Here, $A_1, \lambda$ is the amplitude and length of the linear incoming wave. For the different zone sizes and damping strength, the forces are almost identical.

Table 1 summarizes the hydrodynamic coefficients of a truncated circular cylinder undergoing forced heave motion. Based in Figure 4-3, 4-4 and this table, it is obvious that the computational result is insensitive to both the strength and size of zone.

Figure 4-5 shows the second-order wave profile near a truncated cylinder. Figure (a) and (b) have different strength of beaches, but any significant difference of wave profile is not found. The hydrodynamic force on the body is shown in Figure 4-6. Like the linear force, it is obvious that the second-order force is insensitive on the damping parameters. Therefore, the wave-absorbing zone is valid also for the second-order problem, as expected.

When the incident wave is irregular, the damping mechanism must take care of the longest and shortest waves simultaneously. Since the beach strength is related to the wave frequency and the beach size is a function of the wave length, the zone must be wide enough to damp the longest wave and the beach strength must be strong enough to damp the shortest wave. However, as shown in Figure 4-2, the grid resolution at the artificial beach is too coarse to simulate short waves since the grid size expands towards the truncation boundary. In this case, not the artificial beach but the numerical damping plays a significant roll to damp short waves, and the primary roll of the wave-absorbing zone is to eliminate long waves. The test cases for the irregular incident waves are described in section 4.5.

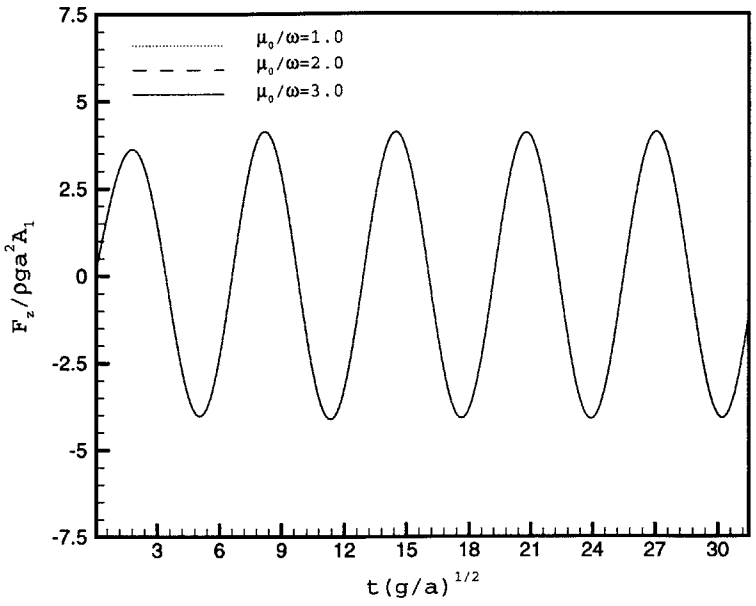


Figure 4-3: Linear horizontal force acting on a single truncated cylinder : $\omega(a/g)^{1/2} = 1.0$, $L/\lambda = 1.0$, different damping strength

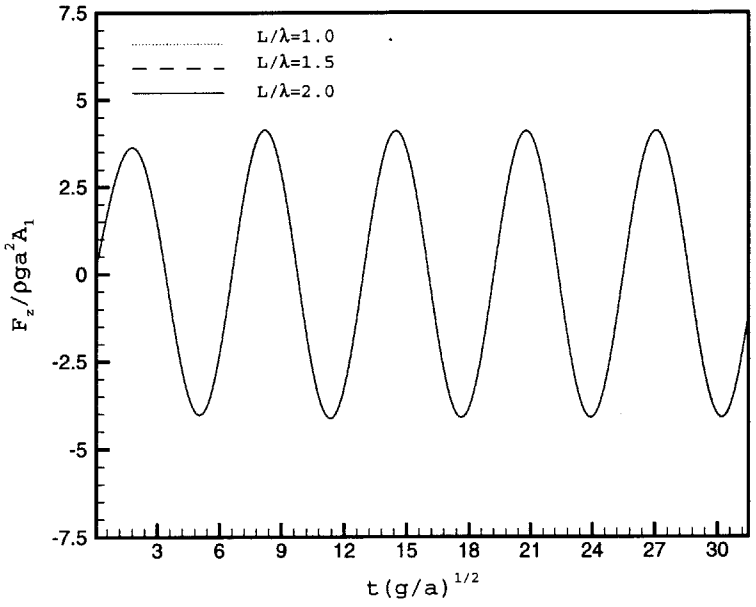


Figure 4-4: Linear horizontal force acting on a single truncated cylinder : $\omega(a/g)^{1/2} = 1.0$, $\mu_0/\omega = 2.0$, different zone size

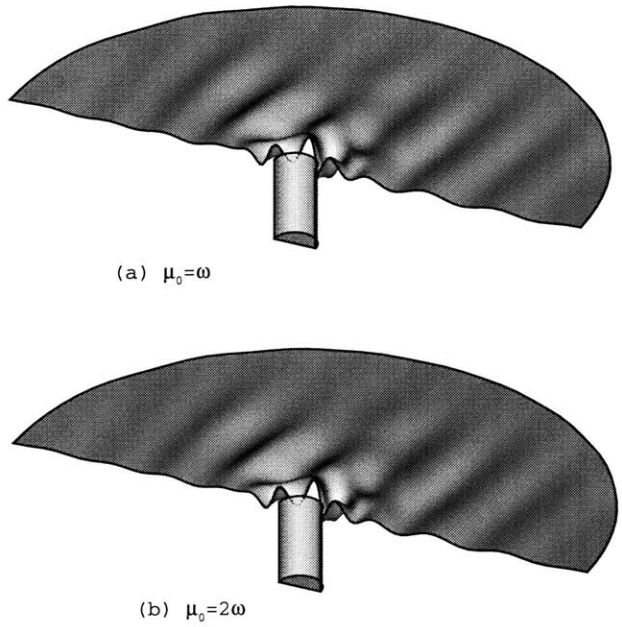


Figure 4-5: Instantaneous second-order wave profiles for different damping strength : $\omega(a/g)^{1/2} = 1.0$, $L/\lambda = 1.0$, $t(g/a)^{1/2} = 25.133$

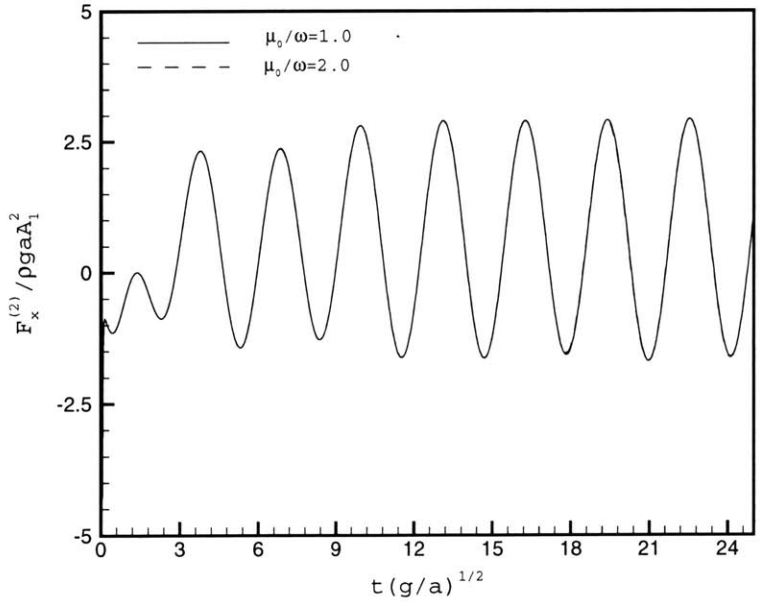


Figure 4-6: Second-order horizontal force acting on a single truncated cylinder : $\omega(a/g)^{1/2} = 1.0$, $L/\lambda = 1.0$, different damping strength

## 4.3 Linear Radiation Problem

The linear radiation problem has been solved for a single vertical cylinder and an array of four vertical cylinders. The hydrodynamic forces were obtained by direct integration of the pressure on the bodies.

Figure 4-7 illustrates the free surface elevation for the four-cylinder array in forced surge motion. This array is the typical shape of a tension-leg platform (TLP). The hydrodynamic coefficients for this solution are compared to the frequency-domain code, WAMIT, in Figure 4-9 and 4-8. In this case, 3500 panels are distributed on the free surface and 1260 panels are distributed on the body. The free surface has been divided into four patches in order to fit the mesh near the body. In the actual computation the symmetry condition is applied so that only half the domain needs to be considered. Since, the continuity of the solution has not been explicitly enforced at the boundaries of the patches, there is a slight error at these intersections. This error decays with increasing grid density and doesn't have a significant effect on the body forces.

The principle of linear superposition allows a multi-frequency time domain simulation. Figure 4-10 shows the time history of the vertical force acting upon a single cylinder forced to heave with eleven frequency components. This case is intended to demonstrate the ability of the numerical beach to absorb both short and long wavelengths simultaneously. The grid resolution is small enough for the highest frequency, and the domain is large enough for the longest wave. Figure 4-11 presents the added mass and damping coefficients for the single and multiple frequency solutions. There is no significant discrepancy between the two cases.

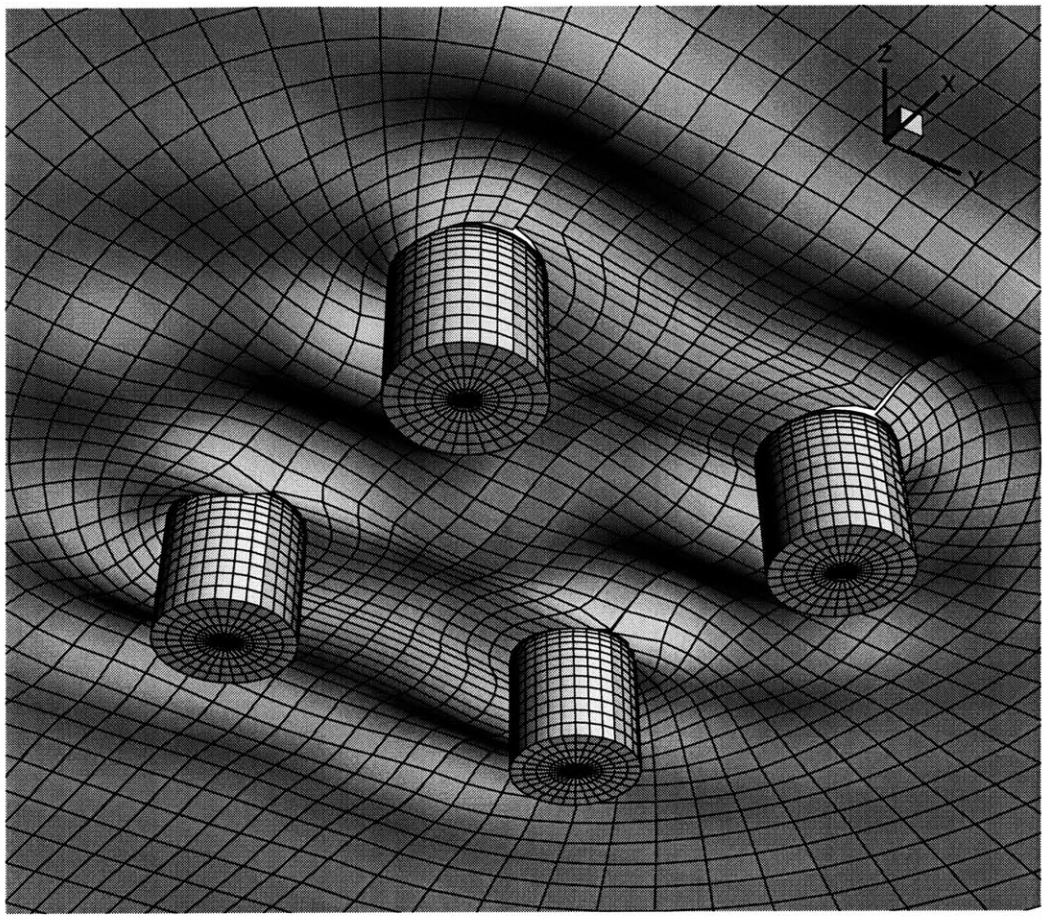


Figure 4-7: Wave profile near a 4-cylinder array under forced surge motion : $a/d = 1.0$ for each cylinder, $(x/D, y/D) = (1.5, 1.5), (1.5, -1.5), (-1.5, -1.5), (-1.5, 1.5)$, $\omega(D/g)^{1/2} = 2.0$

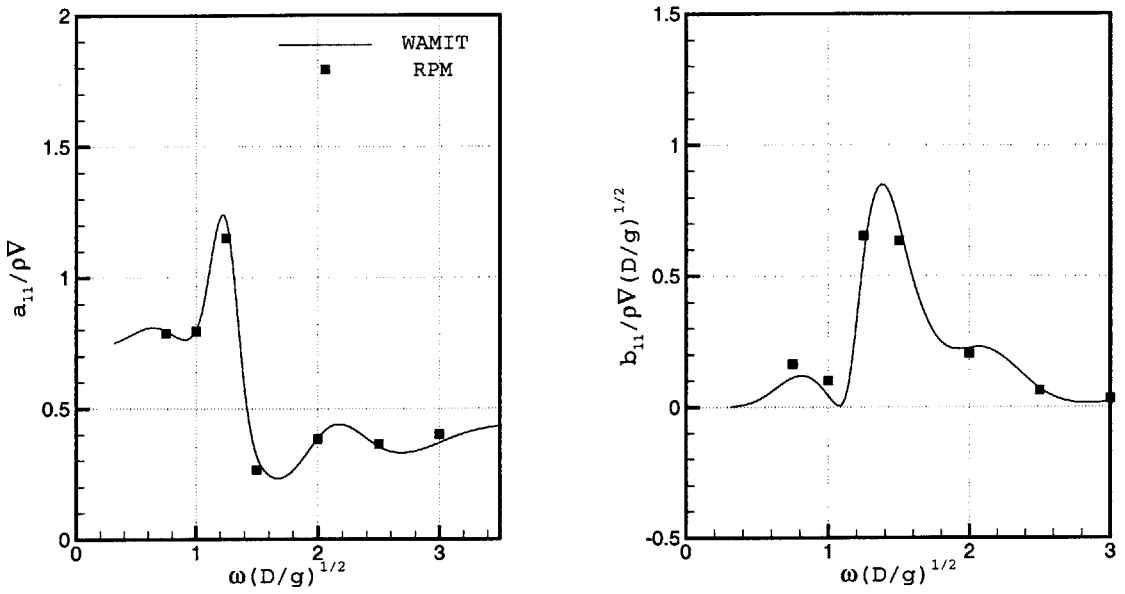


Figure 4-8: Surge added mass and damping coefficient of a 4-cylinder array : the same array with Figure 4-7

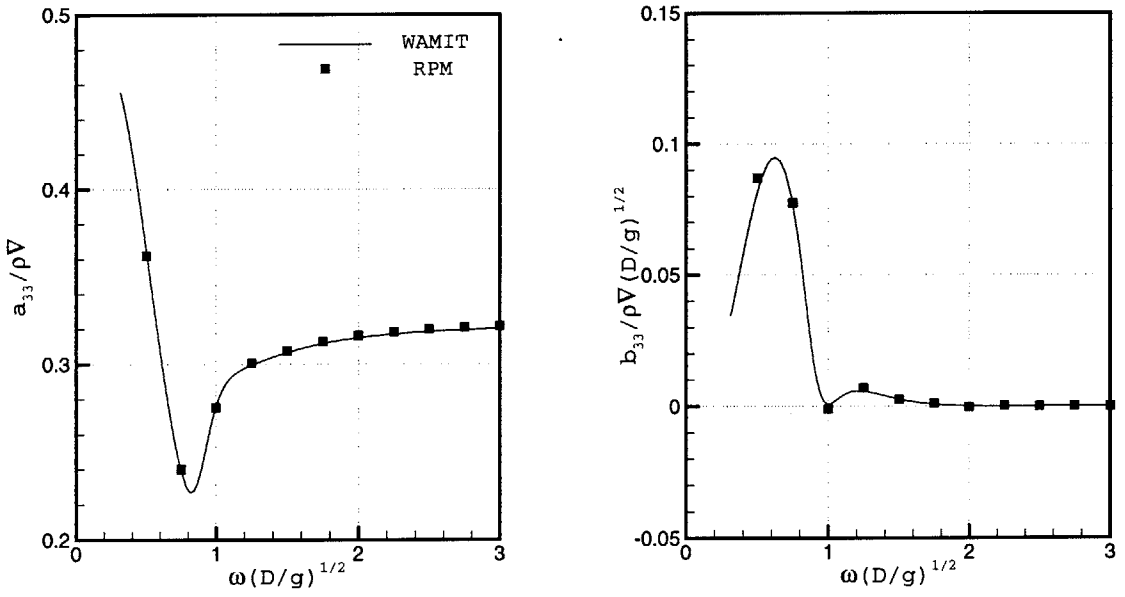


Figure 4-9: Heave added mass and damping coefficient of a 4-cylinder array : the same array with Figure 4-7

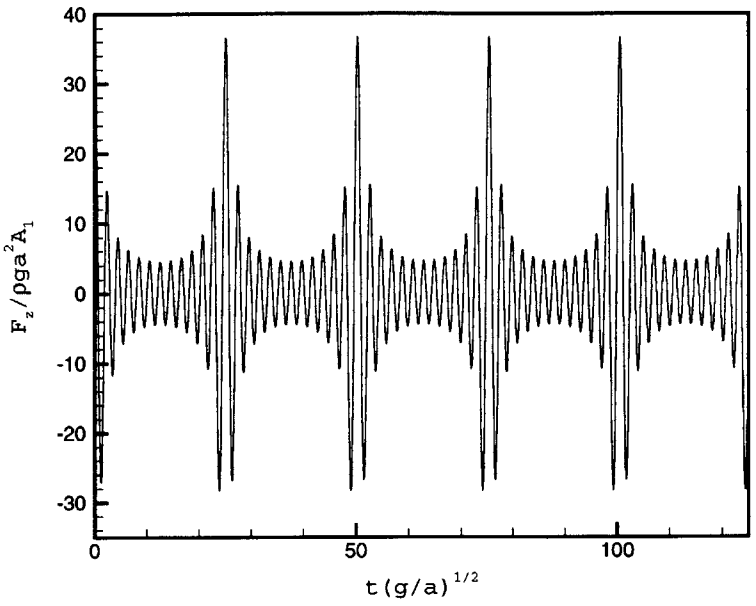


Figure 4-10: Time-history of vertical force on a single cylinder in force heave motion with multi frequencies : $a/d = 1.0, \xi_0/a = 0.05$

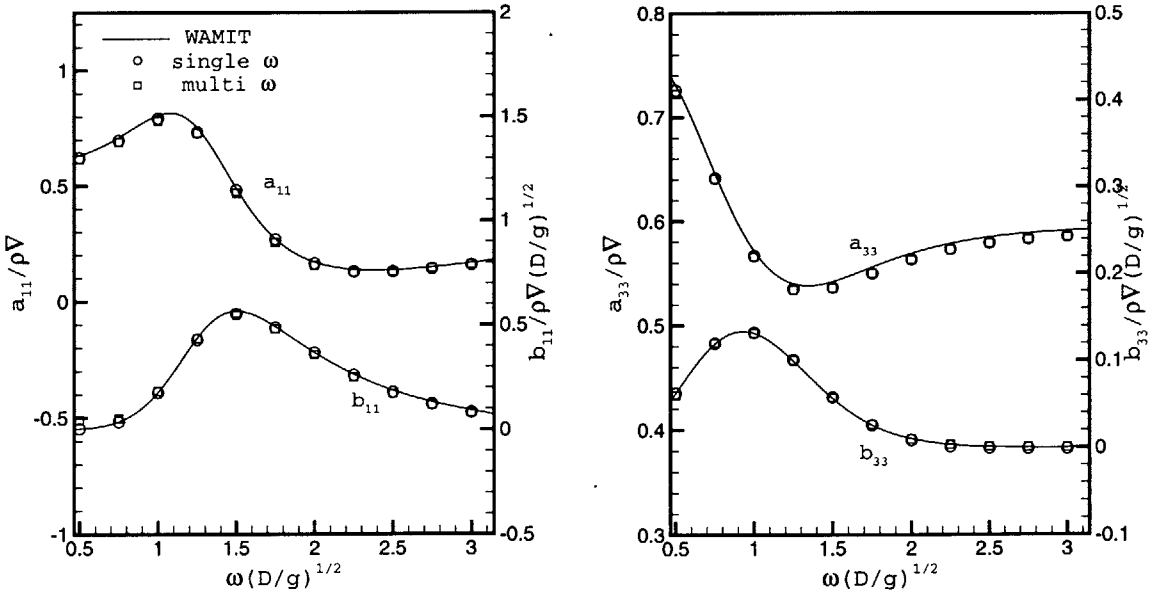


Figure 4-11: Added mass and damping coefficient for surge and heave motion : the same cylinder with Figure 4-10

## 4.4 Linear & Second-Order Diffraction Problem : Monochromatic Wave

The computational procedure for the linear diffraction problem is the same as the radiation problem except for the incident wave forcing. However, the second-order problem is more complicated for two reasons. First, the relative value of the second-order physical parameters is small in comparison to the linear solution. A small error in the linear solution may lead to a large error in the second-order solution. An accurate solution of the underlying linear problem is essential. Second, the grid resolution for the second-order problem must be more fine since it is driven by the double frequency of the linear wave. With the application of the multi-grid approach, computational efficiency does not suffer since a smaller domain can be used.

Figure 4-12 illustrates the wave elevation near a bottom-mounted circular cylinder in a regular incident wave. Although scattering is not evident in the linear problem at this frequency, the second-order problem does show significant diffraction. In this case, the contribution of the second-order solution to wave run-up is obvious. Figure 4-13 shows the contours of the disturbance velocity potential around a cylinder. The second-order potential is much more localized around the cylinder.

Figure 4-14 shows the comparison of the time history of the horizontal force acting upon the cylinder. The second-harmonic component induces a peak force greater than the linear contribution.

The hydrodynamic forces are illustrated in Figures 4-15 and 4-16. Figure 4-15 shows the linear wave excitation force, and Figure 4-16 is the second-order quadratic transfer function (QTF). The linear solution is compared to WAMIT and the second-order results are compared to Kim [27]. The result of M.H. Kim is based on a frequency-domain method. He studied the second-order forces for vertical axi-symmetric bodies using a boundary integral method with ring-sources, and the solutions was expedited by analytic integration in the entire local-wave-free outer field of a requisite

free-surface integral.

In Figure 4-16, $F_q$ is the quadratic force composed from the linear solution, and $F_p$ is the component due to the second-order potential. The total second-order force is $F_2$. The result shows a nice agreement.

Figure 4-17 shows the comparison of the wave run-up with the experiments of Kriebel [41] along the weather ($\theta = 0$) and lee ($\theta = 180$) sides. The computational results are actually computed at $r = 1.02a$ and the experimental data is the averaged value over 10 waves. It is obvious that the linear solution is not sufficient, and the second-order contribution is significant. When the waves become steep, the second-order solution will also not be sufficient because of stronger nonlinear effects.

Figure 4-18 shows the time history of the vertical force acting upon a truncated circular cylinder in infinite depth. In this case, the major contribution to the vertical force comes from second-order theory. The particular solution of the second-order inhomogeneous problem is the main component. As discussed by Newman [57], the partial standing waves generated by interference of the scattered and incoming wave induce a pressure component which does not decay with depth. This leads to an effect sometimes called a microseism. The wave-absorbing zone used in this study has proven to be sufficient for this type of standing wave. In Figure 4-19, the QTF of the second-harmonic vertical force is compared to the result of Kim [28], and shows good agreement.

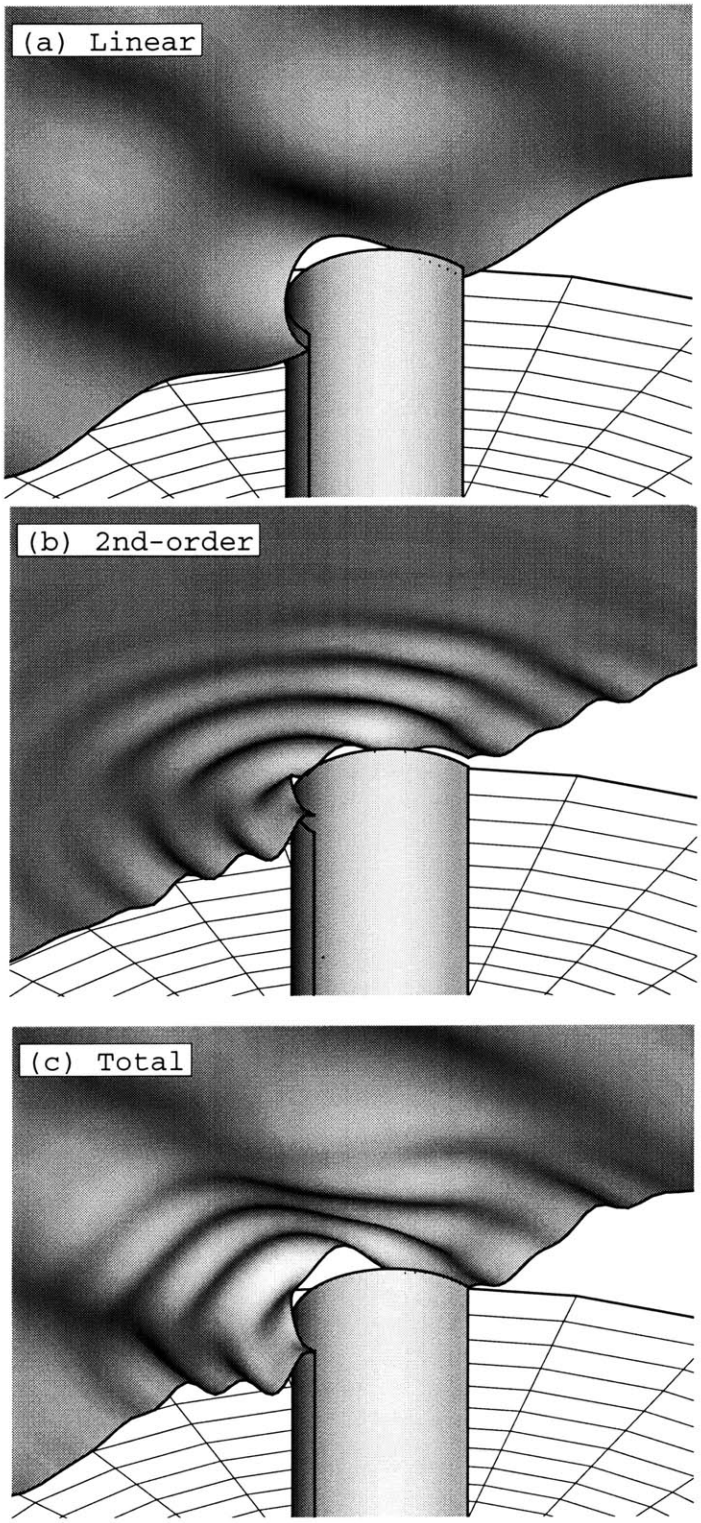


Figure 4-12: Wave profile near a bottom-mounted cylinder : diffraction problem, $a/d = 0.25$, $k_1 a = 2.0$, $A_1/a = 0.2$

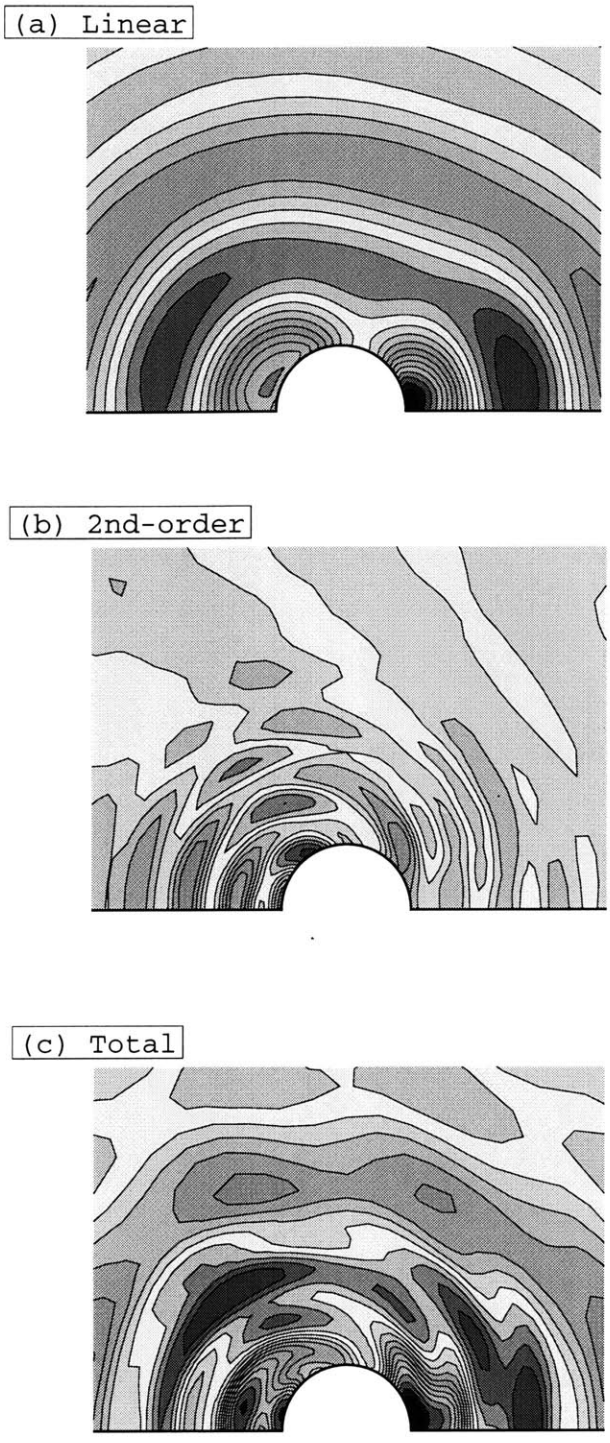


Figure 4-13: Contour profile of the diffraction potential near a bottom-mounted cylinder : the same case with 4-13

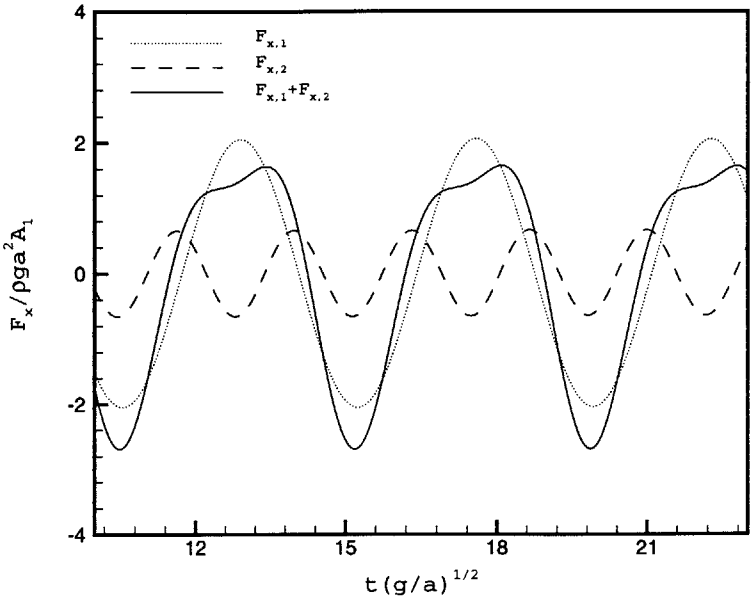


Figure 4-14: Time-history of horizontal force on a bottom-mounted cylinder : diffraction problem, the same cylinder with Figure 4-12

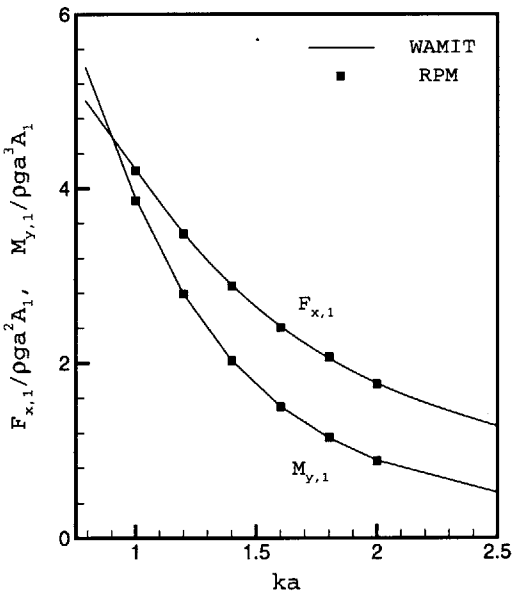


Figure 4-15: Linear wave excitation force and moment on a bottom-mounted cylinder : the same cylinder with Figure 4-12

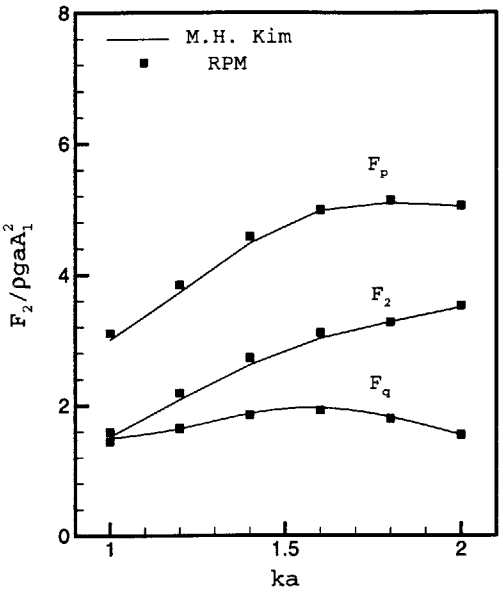


Figure 4-16: Module of surge QTF on a bottom-mounted cylinder : the same cylinder with Figure 4-12

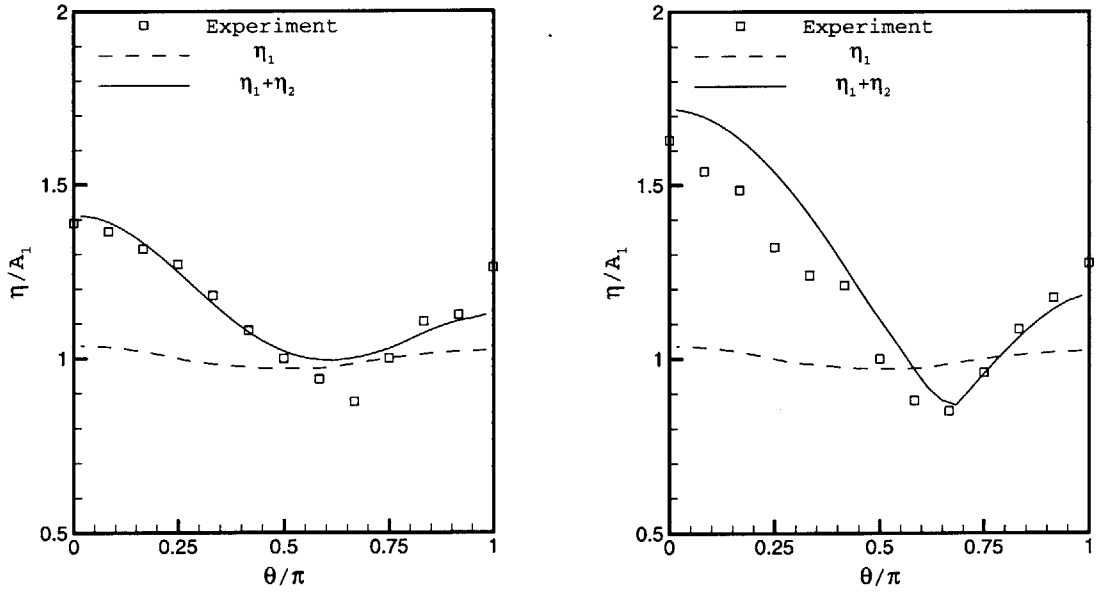


Figure 4-17: Wave run-up on(experiment)/near(computation) a bottom-mounted cylinder : $d/a = 2.768, k_1 a = 0.271$, (a) $A_1/a = 0.244$, (b)$A_a/a = 0.397$

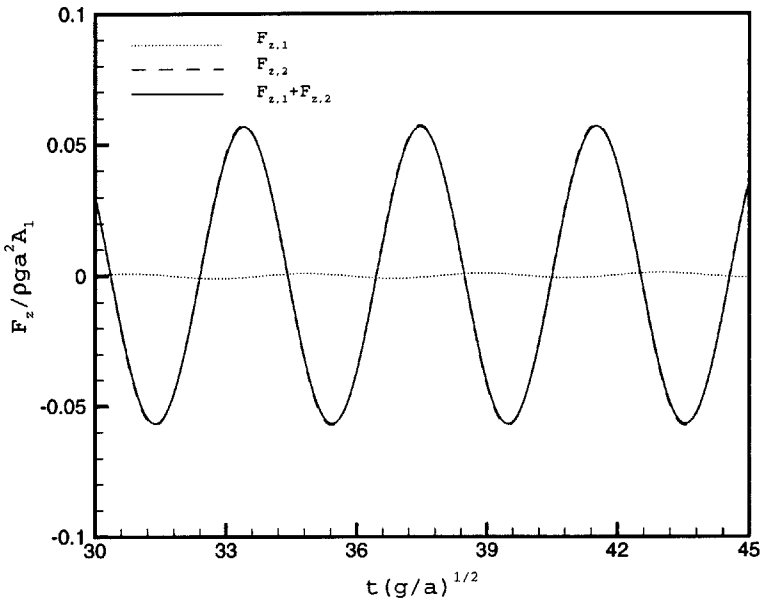


Figure 4-18: Time-history of the vertical forces on a single truncated cylinder : $d/a = 2.075, k_1 a = 0.6, A_1/a = 0.2$

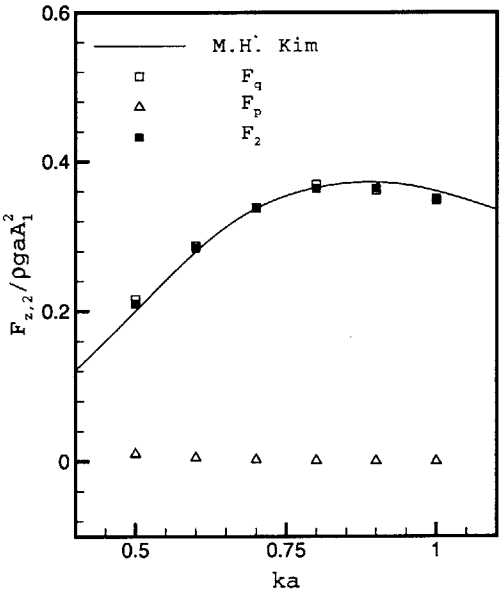


Figure 4-19: Module of heave QTF on a single truncated cylinder : the same cylinder with Figure 4-18

## 4.5 Wave Loads at Irregular Waves

The computation is extended to irregular incident wave. The linear radiation problem with multiple frequencies was mentioned in section 4.3, and it was found that the linear superposition can be well simulated by the present numerical method.

The second-order problem with irregular wave is more complicated than the linear problem due to the nonlinear interaction of components. In a monochromatic wave, the second-order quantities vary with only a double-harmonic frequency. However, in the multi-frequency waves, the quadratic characteristics dictate the second-order quantities so that each component induces the sum- and difference-frequency terms through the interaction with other frequency waves.

A time signal of the second-order quantity can be written as the following generalized form :

$$f(t) = \sum_{i=1}^{N}\sum_{j=1}^{N} A_i A_j \; [\; f^{+}_{i,j} cos\{(\omega_i + \omega_j)t + \psi^{+}_{i,j})\} + f^{-}_{i,j} cos\{(\omega_i - \omega_j)t + \psi^{-}_{i,j})\} \;] \quad (4.1)$$

where $A_i$ is the amplitude of incident wave and $f^{+}_{i,j}, f^{-}_{i,j}$ are the sum and difference quadratic transfer functions. In addition, $\psi^{+}_{i,j}$ and $\psi^{-}_{i,j}$ are the phases. The difference-frequencies contribute to the mean and slowly-varying components. On the other hand, the sum-frequencies don't provide the mean value but generate high-frequency response.

For example, in the bichromatic wave, a second-order quantity is written with a mean value and four frequencies, $2\omega_1, 2\omega_2, |\omega_1 - \omega_2|$, and $\omega_1 + \omega_2$, such that

$$\begin{aligned} f(t) \;=\; & A_1 A_2 \; [\; f_o + f^{+}_{1,1} \cos(2\omega_1 t + \psi^{+}_{1,1}) + f^{+}_{2,2} \cos(2\omega_2 t + \psi^{+}_{2,2}) \\ & + 2 f^{+}_{1,2} \cos\{(\omega_1 + \omega_2)t + \psi^{+}_{1,2}\} + 2 f^{-}_{1,2} \cos\{(\omega_1 - \omega_2)t + \psi^{-}_{1,2}\} \;] \end{aligned} \quad (4.2)$$

Figure 4-20 and 4-21 show the time-histories of the second-order surge force on a bottom-mounted cylinder when the incident waves are bichromatic. Since the

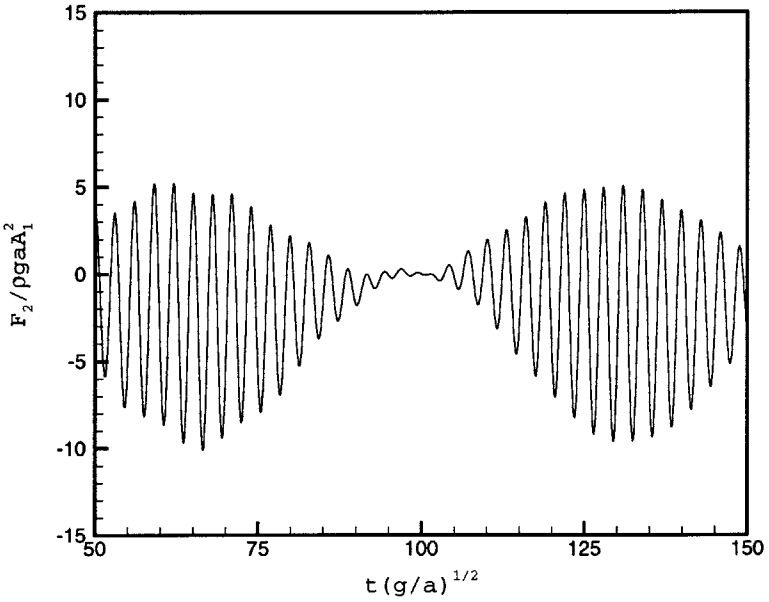


Figure 4-20: Time-history of the second-order surge force on the cylinder at bichromatic waves : a bottom-mounted cylinder, $h/a = 4, k_1a = 1.0, k_2a = 1.2, A_{1,2}/a = 0.1, \beta_{1,2} = 180^o$

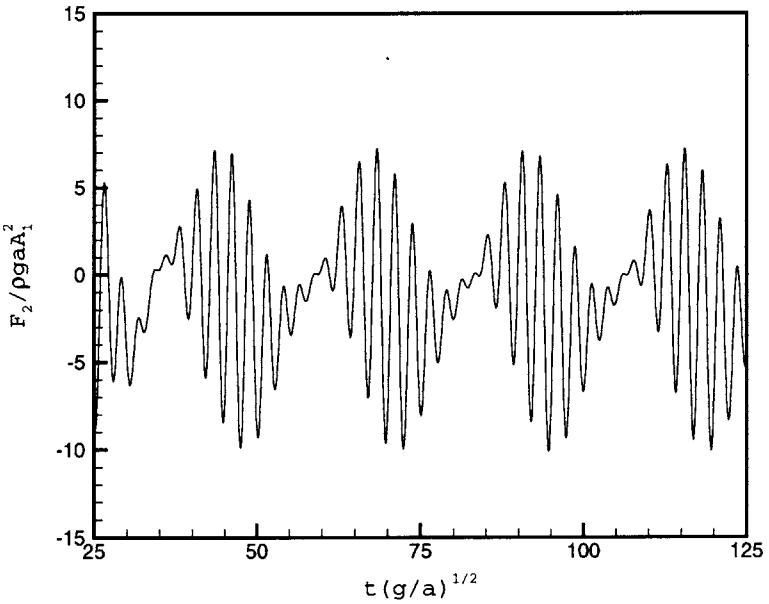


Figure 4-21: Time-history of the second-order surge force on the cylinder at bichromatic waves : a bottom-mounted cylinder, $h/a = 4, k_1a = 1.0, k_2a = 1.6, A_{1,2}/a = 0.1, \beta_{1,2} = 180^o$

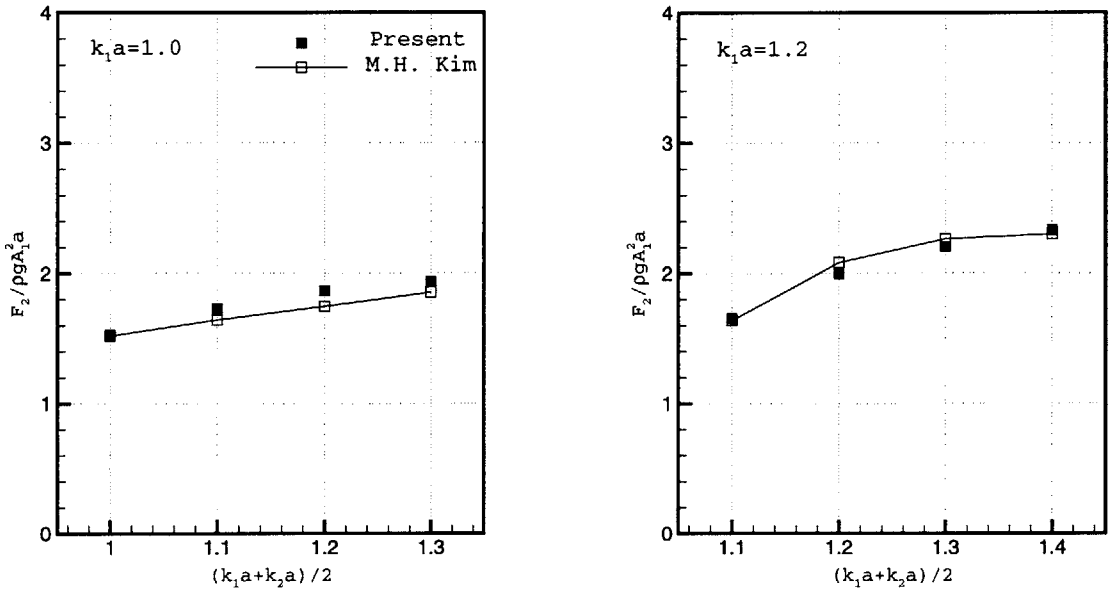


Figure 4-22: Surge QTF obtained from the force signal of bichromatic waves : the same cylinder with Figure 4-20, $k_1a = 1.0, 1.2$(fixed), $A_{1,2}/a = 0.1, \beta_{1,2} = 180^o$

difference-frequencies of two cases are different, two signals show very different modulations. Using the Fourier transform described in section 3.2, five components in equation (4.2) can be extracted from each signal. Figure 4-22 shows the sum-frequency surge QTF obtained from the signals. The results are compared with M.H. Kim's [27], and the agreement is very favorable.

When the linear incident wave contains more than two components, the numerical computation and time-signal analysis become more complicated. For the numerical computation, the largest frequency, i.e. the shortest wave length, influences on the time step and panel size. On the other hand, the smallest frequency, i.e. the longest wave length dictates the maximum simulation time and computational domain. In the second-order problem, in general, the minimum frequency is the smallest difference-frequency. Furthermore, the maximum frequency is always twice of the largest linear frequency.

Since the present study concentrates on the sum-frequency contribution, the computational domain is not extended far enough to cover the whole difference-frequency

waves. The study on the difference-frequency problem can be found in the work of Kim, Sclavounos, Nielson [29]. According to numerical experiences, in general, the accuracy of the difference-frequency quantities is better than that of the sum-frequency quantities.

Figure 4-23 shows the time histories of the wave elevation, the linear and second-order surge forces on the cylinder when four linear frequencies are imposed. The wave elevation is at $x = 0$. In the case of linear force, the corresponding frequency-domain result contains four components which have the same frequencies with the incident waves. While the second-order force signal consists of 16($4\times4$) sum-frequency components and 16($4\times4$, including diagonals which contribute on the mean value) difference-frequency components.

The diagonal double-frequency QTF obtained from the single signal shown in Figure 4-23 is plotted in Figure 4-24, comparing the magnitude of QTF of a monochromatic wave computation at each frequency. The agreement is quite good.

In the numerical simulation of multi-component waves, the computational parameters should be carefully selected since the different time and length scales may be mixed in a single run. In the present study, a thorough study was carried out in order to observe the sensitivity on the computational parameters. The case with $k_1a = 1.0, 1.2, 1.4, 1.6$, shown above, was tested since the accurate QTF's are given by M.H. Kim [27]. The considered parameters are as follows :

(1) Computational Domain

The computational domain is related to wavelength. Particularly, if the difference-frequency component is supposed to be observed, the computational domain must be extended far enough to cover the long wave generated by the difference-frequency. The linear wavelength of this case varies from $3.9a$ $2\pi a$ and the second-order wavelength varies approximately from $a$ (the shortest sum-frequency wave) to $150a$ (the longest difference-frequency wave). In this parametric study, four different domains are considered such that $R/a = 20, 40, 80, 140$ where $R$ is the maximum domain radius. The

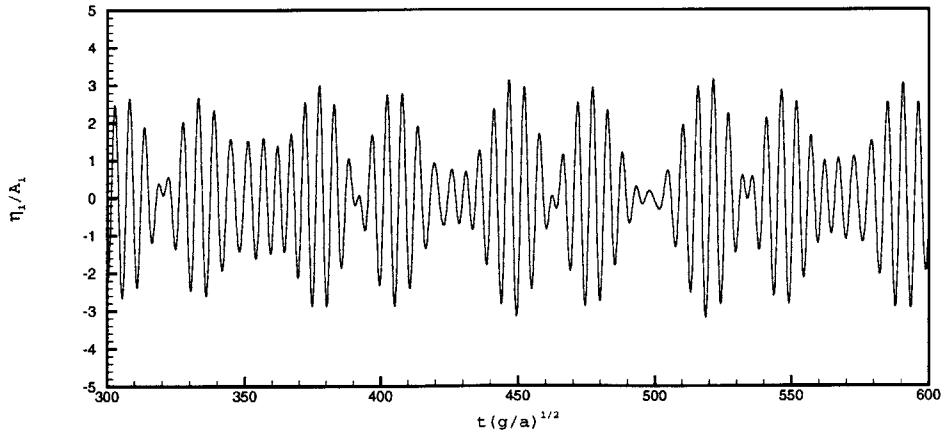


(a) Wave elevation

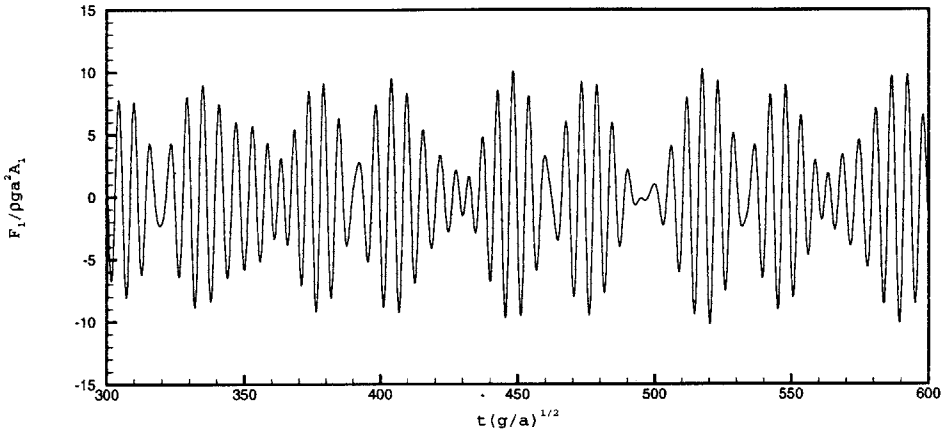


(b) Linear force

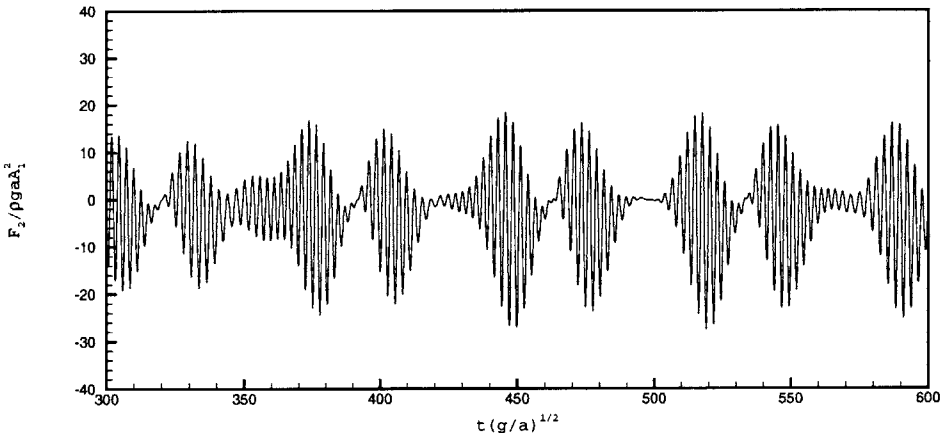


(c) Second-order force

Figure 4-23: Time-history of the wave elevation, the linear and second-order surge force on the cylinder at multi waves : $k_1 a = 1.0, 1.2, 1.4, 1.6, A_{1,2,3,4}/a = 0.1, \beta_{1,2,3,4} = 180^o$, no phase difference

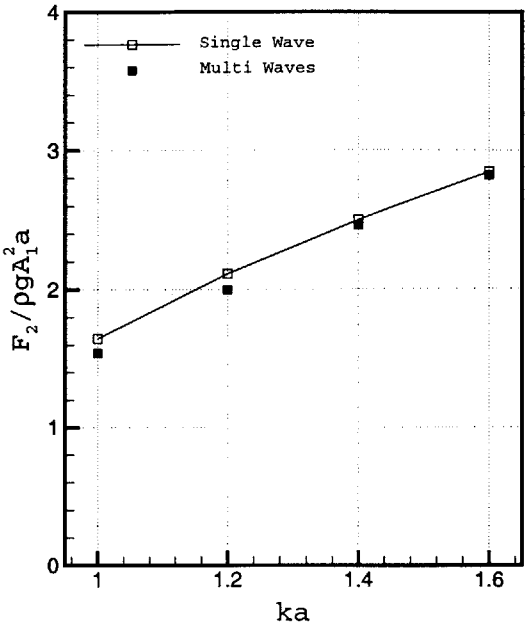


Figure 4-24: Comparison of the diagonal sum-frequency surge QTF between monochromatic wave and multi waves : the same cylinder with Figure 4-23

reason that the truncation domains are less than the longest difference-frequency wave length is because the present study concentrates on the sum-frequency component. Here, the panel resolution is the same.

Figure 4-25(a) compares 4×4 sum-frequency surge QTF matrices of four domains with M.H. Kim's results. The discrepancy of these QTF's is not significant, thus it means that the broad range of the computational domain can be applied. An interesting fact found in this study is that the difference-frequency QTF matrices, shown in Figure 4-25(b), are also very close to M.H. Kim's result. In spite of small domains which are much less than the difference-frequency wave length, the difference-frequency QTF's show quite favorable agreement.

(2) Grid Resolution

The grid resolution is an important parameter for the short waves, i.e. the sum-frequency components. It is related to the numerical damping and the accuracy of

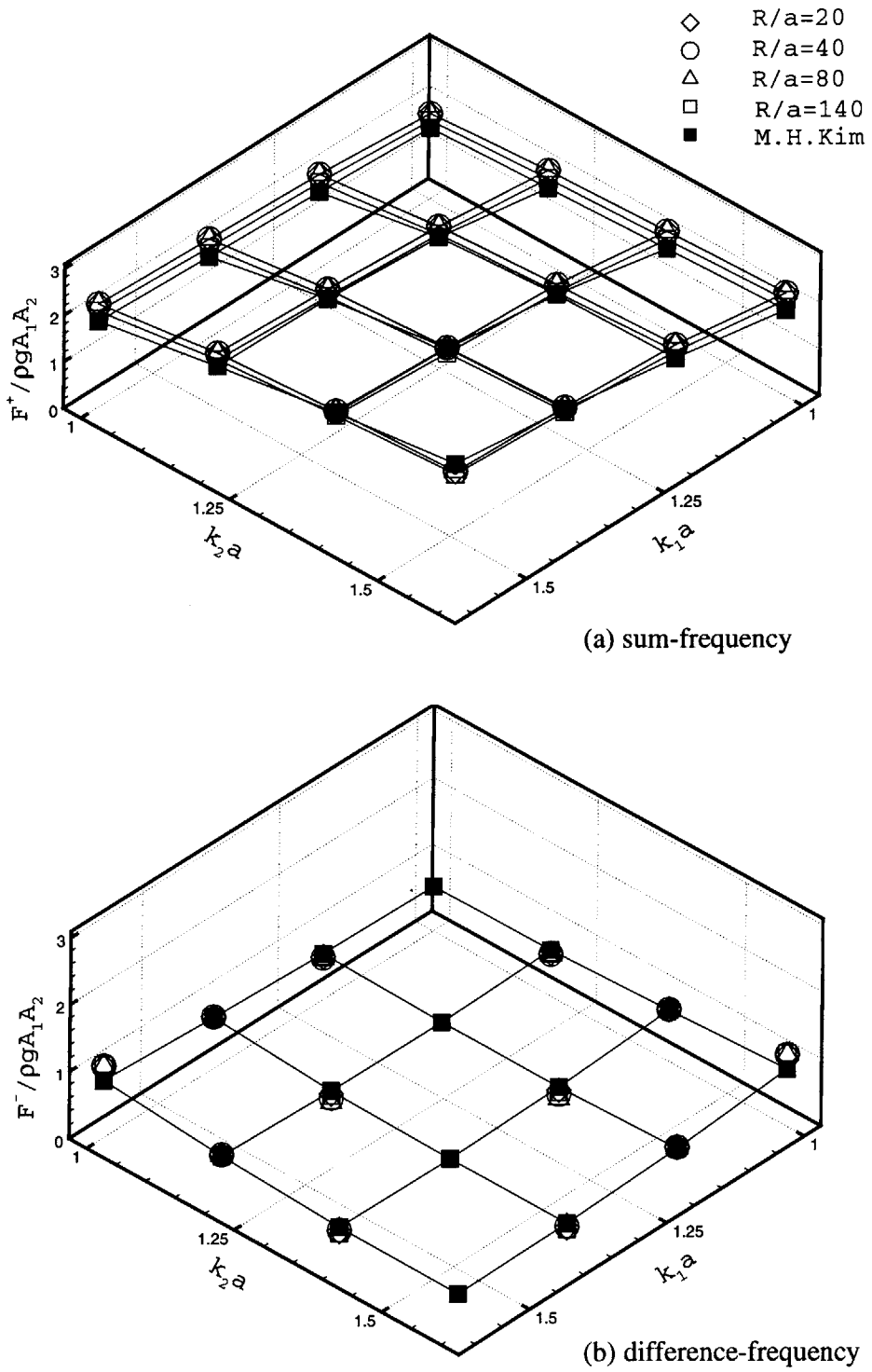


Figure 4-25: Four by four surge QTF matrix obtained from a single time history at multi waves : the same cylinder with Figure 4-23, different computational domain, (a) sum-frequency (b) difference-frequency

hydrodynamic forces on a body. Moreover, in the viewpoint of computational efficiency, it is also important to find the optimum number of panels within an acceptable tolerance of accuracy.

In the present study, the computational domain is fixed to $R/a = 80$, while the numbers of panels are changed in order to get different grid resolutions. Figure 4-26 shows the QTF matrices for the different numbers of panels. In all cases, more than 8 panels are distributed within the shortest wavelength near the body. The computational results don't show any significant discrepancy, meaning these solutions are converged.

According to numerical experiences, the most critical parameter in the panel resolution is a grid size near the body. Since the sum-frequency contribution is very localized near the body, the grid should be fine enough to resolve the shortest wave near the body. Based on the present study, it is recommended to distribute at least 7 or 8 panels within the shortest wave length around the body. However, too fine grid will result in a computational inefficiency since it requires too much small time segment and a lot of CPU time.

(3) Time Segment

The time segment is related to the temporal stability and computational efficiency. A good parameter in the selection of the time segment is the smallest wave period, i.e. the largest wave frequency. The present study was carried out for $\Delta t = T_{min}/N$ with $N = 150, 300, 500$. Here, $T_{min}$ indicates the smallest linear wave period within four components.

The computed QTF matrices are shown in Figure 4-27. The results are a little more sensitive than the space discretization parameters, in particular in the sum-frequency values. However, even for $N = 150$, the accuracy is quite favorable.

(4) Sampling Time for Fourier Transform

Since the time signal must be transformed into the frequency domain in order to

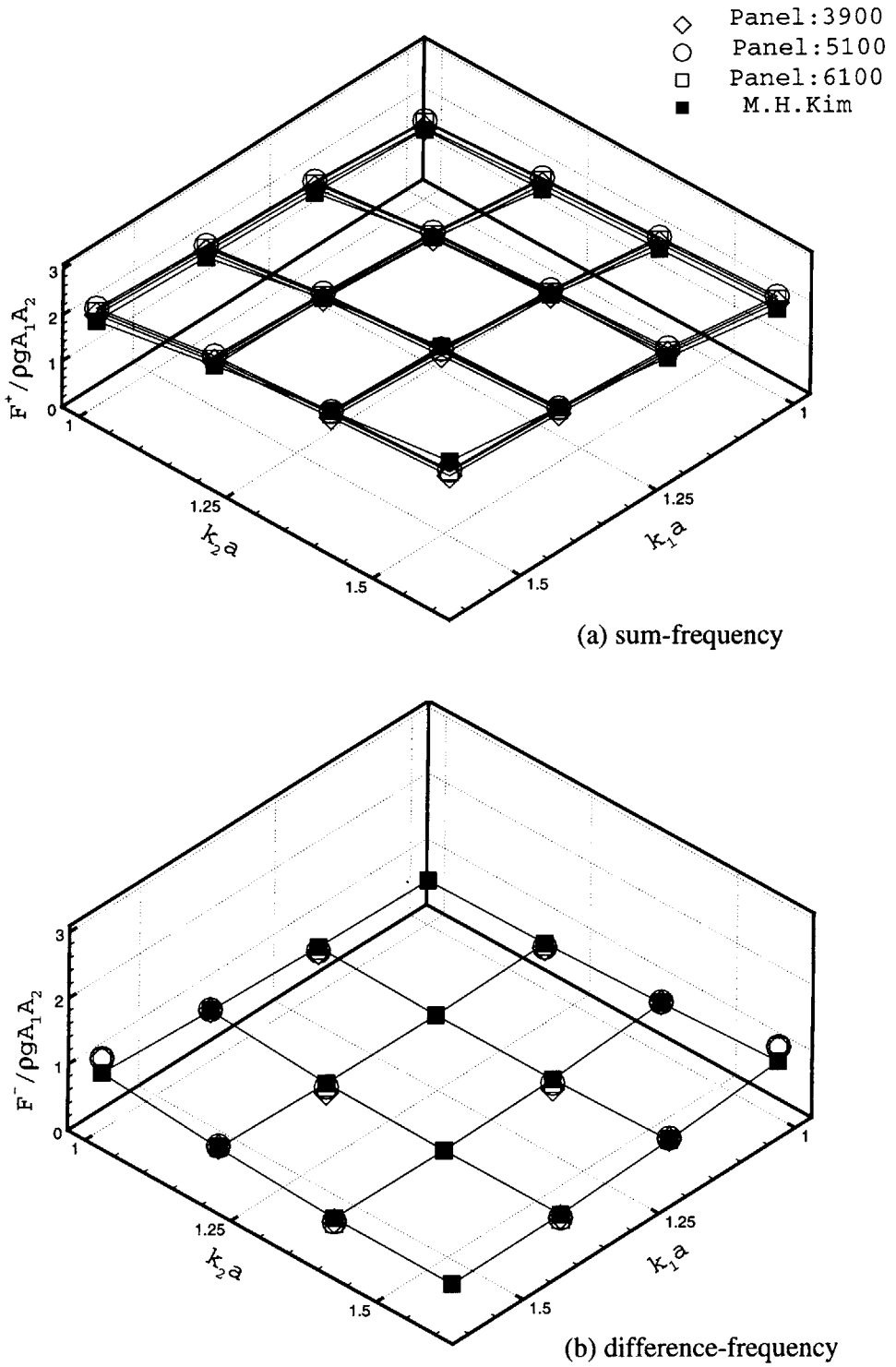


Figure 4-26: Four by four surge QTF matrix obtained from a single time history at multi waves : the same cylinder with Figure 4-23, different numbers of panels, (a) sum-frequency (b) difference-frequency

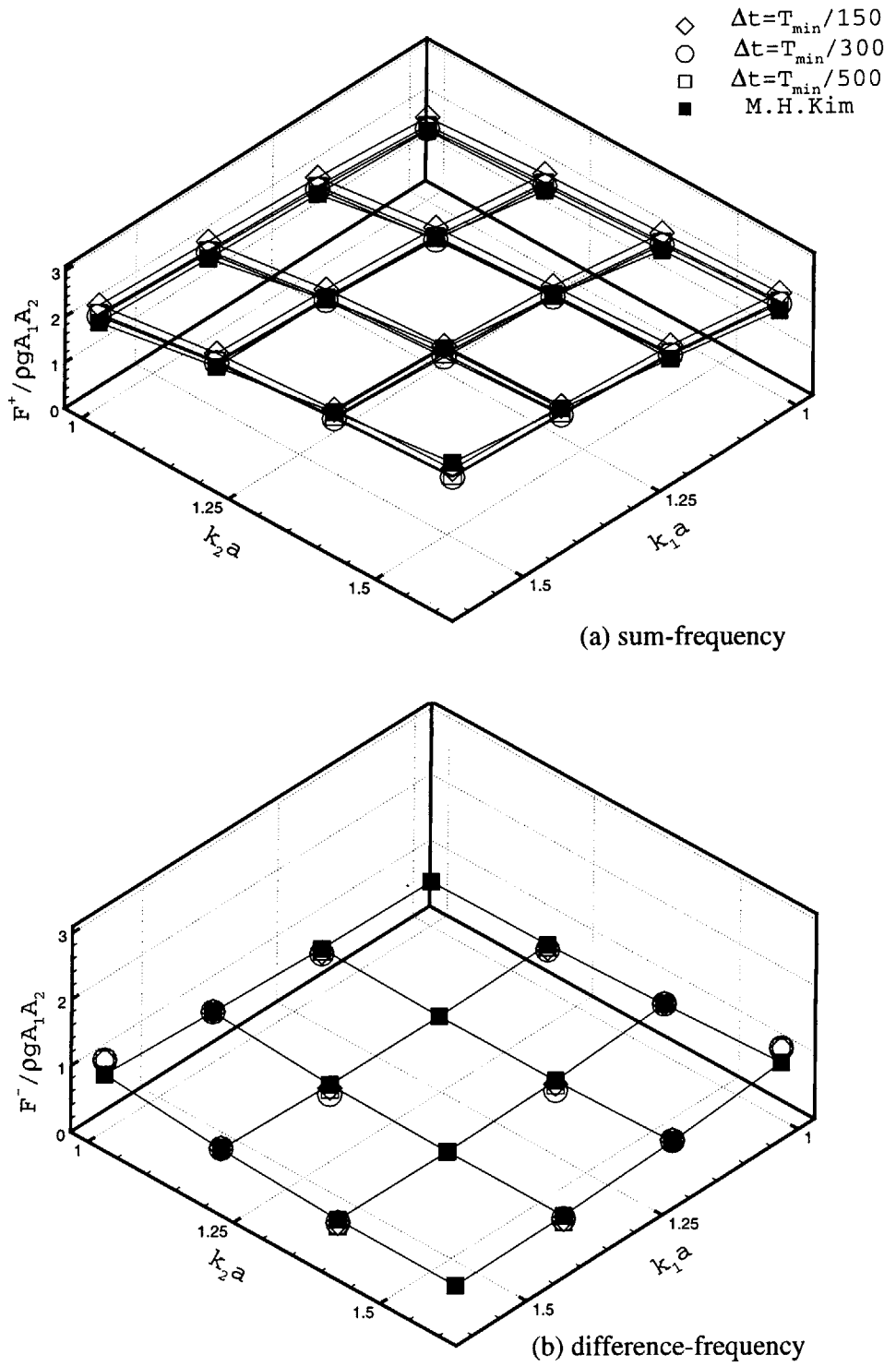


Figure 4-27: Four by four surge QTF matrix obtained from a single time history at multi waves : the same cylinder with Figure 4-23, different time segments, (a) sum-frequency (b) difference-frequency

get a QTF matrix, a proper amount of sampling data must be selected for the Fourier transform. A good parameter to choose the amount of sampling data is the largest wave period,

Figure 4-28 shows the QTF matrices for different sampling times, $T_{FT}$. The upper figure is when $T_{FT}$ is the same with the largest wave period, $T_{max}$, and the below is when $T_{FT} = 2, 3, 4 \times T_{max}$. In this case, $T_{max}$ comes from the smallest difference frequency, i.e. $T_{max} = 1/2\pi|\omega_i - \omega_j|_{min}$ with $i \neq j$.

It is obvious that $T_{FT} = T_{max}$ is not enough. In particular, despite $T_{max}$ is much longer than any sum-frequency wave period, this time range is not enough to get a reasonable accuracy of the sum-frequency result. The aliasing error in the discrete Fourier transformation may be the reason. That is, the sampling time is not sufficient for the difference-frequency components so that the aliasing error may affects all other components. Hence, the sampling time for the Fourier transform can be a critical parameter. The difference-frequency QTF matrices are shown in Figure 4-29, and the same trend is shown. Based on the present result, it recommended to apply the sampling time more than twice of the longest wave period in order to get an accurate QTF matrix.

(5) Damping Zone

The sensitivity of the computational result on the artificial damping zone was observed since the artificial beach is enforced on long and short waves at the same time. As shown already, the sensitivity on the damping parameters was not significant for the radiation and monochromatic-wave diffraction problems, and it is valid in the multi-frequency diffraction problem. Figure 4-30 shows the QTF matrices for two different sizes of the artificial beach with the same computational domain. A major roll of the damping zone in this problem is to damp long difference-frequency waves. Since the panels on free surface expands toward the truncation boundary, the panel size at far from the body is not fine enough to resolve the short wave length, so that short waves are eliminated by numerical damping before they reach to the truncation

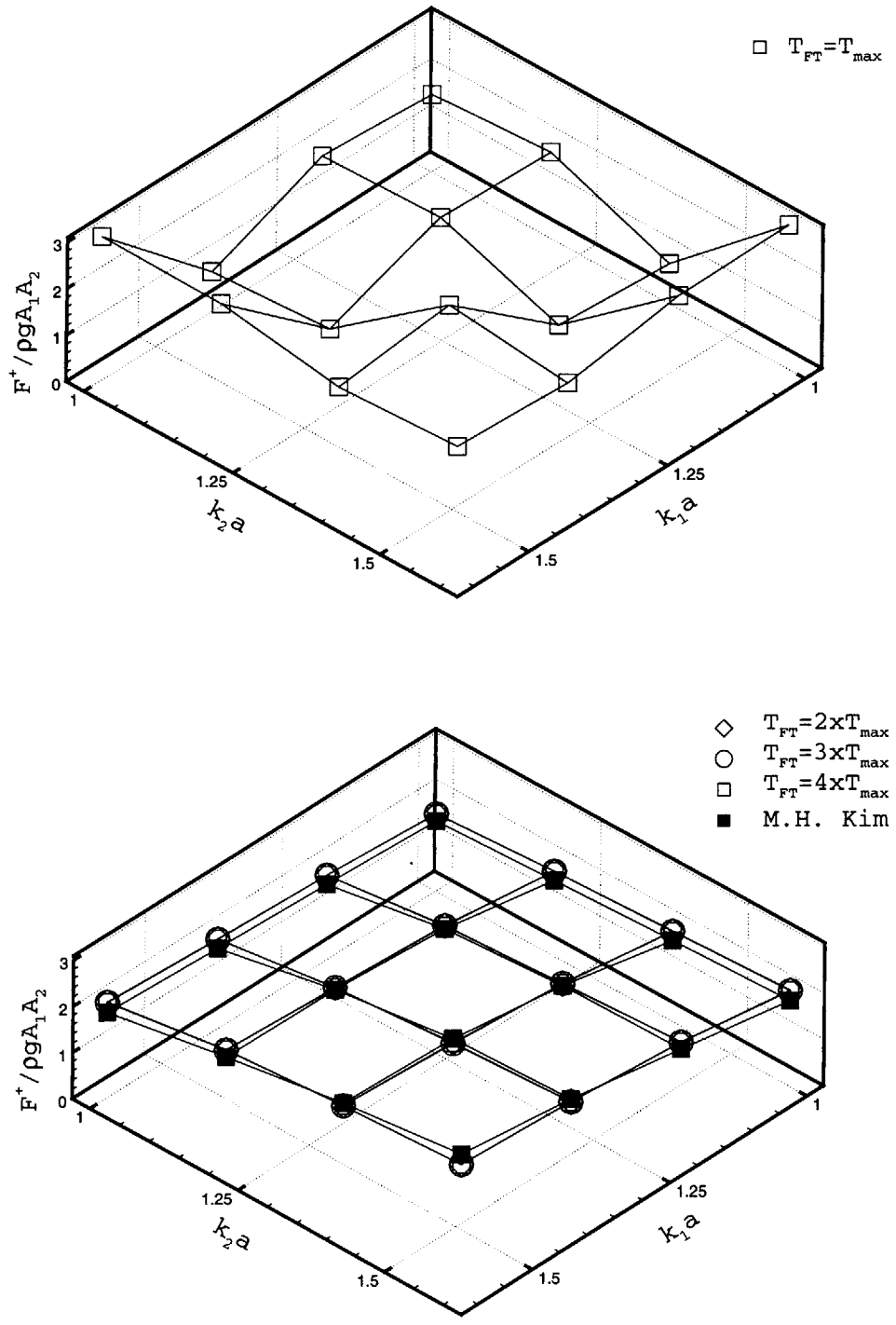


Figure 4-28: Four by four sum-frequency surge QTF matrix obtained from a single time history at multi waves : the same cylinder with Figure 4-23, different sampling time for the Fourier transform, above;$T_{FT} = T_{max}$, below;$T_{FT} = 2, 3, 4 \times T_{max}$

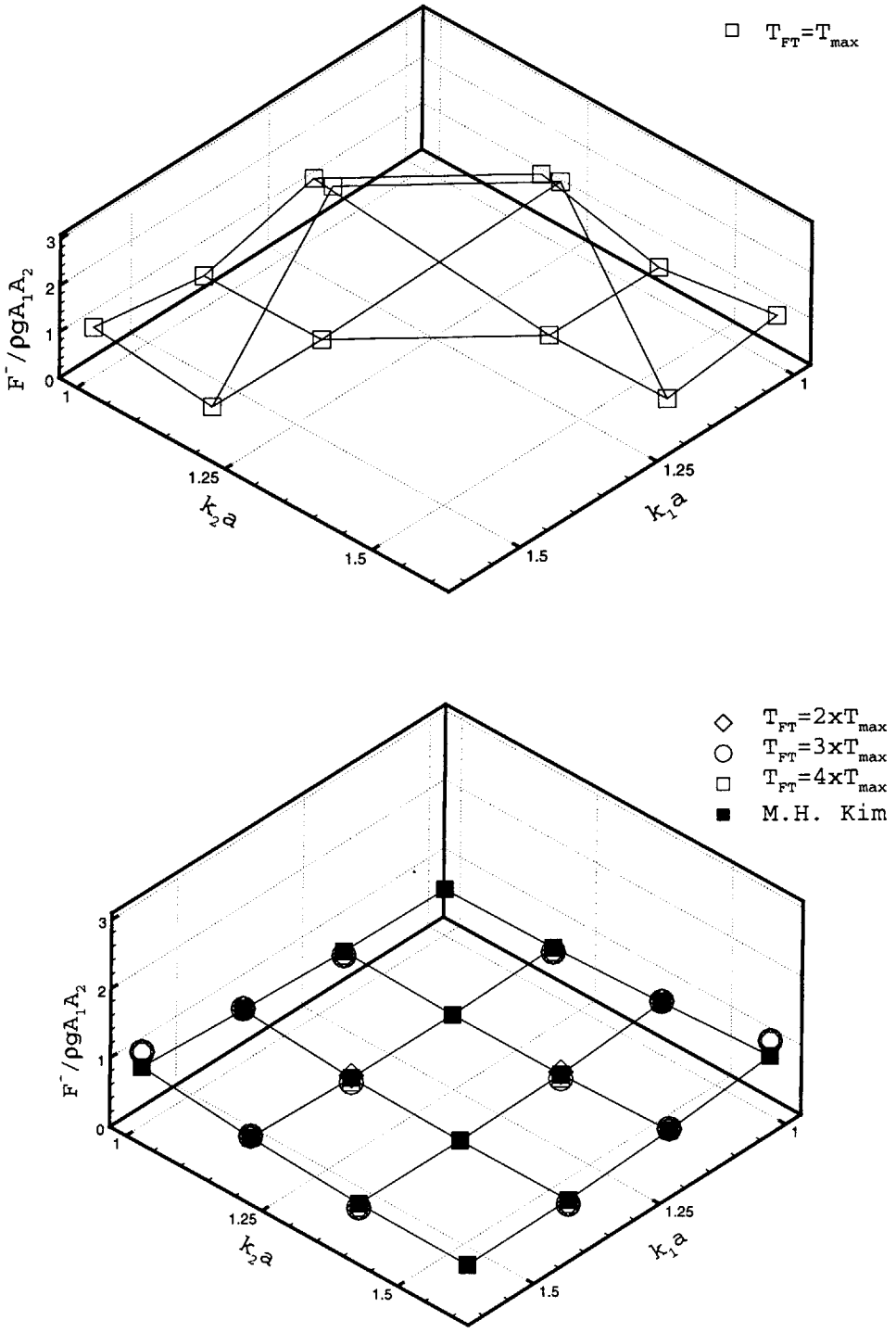


Figure 4-29: Four by four difference-frequency surge QTF matrix obtained from a single time history at multi waves : the same cylinder with Figure 4-23, different sampling time for the Fourier transform, above;$T_{FT} = T_{max}$, below;$T_{FT} = 2, 3, 4 \times T_{max}$

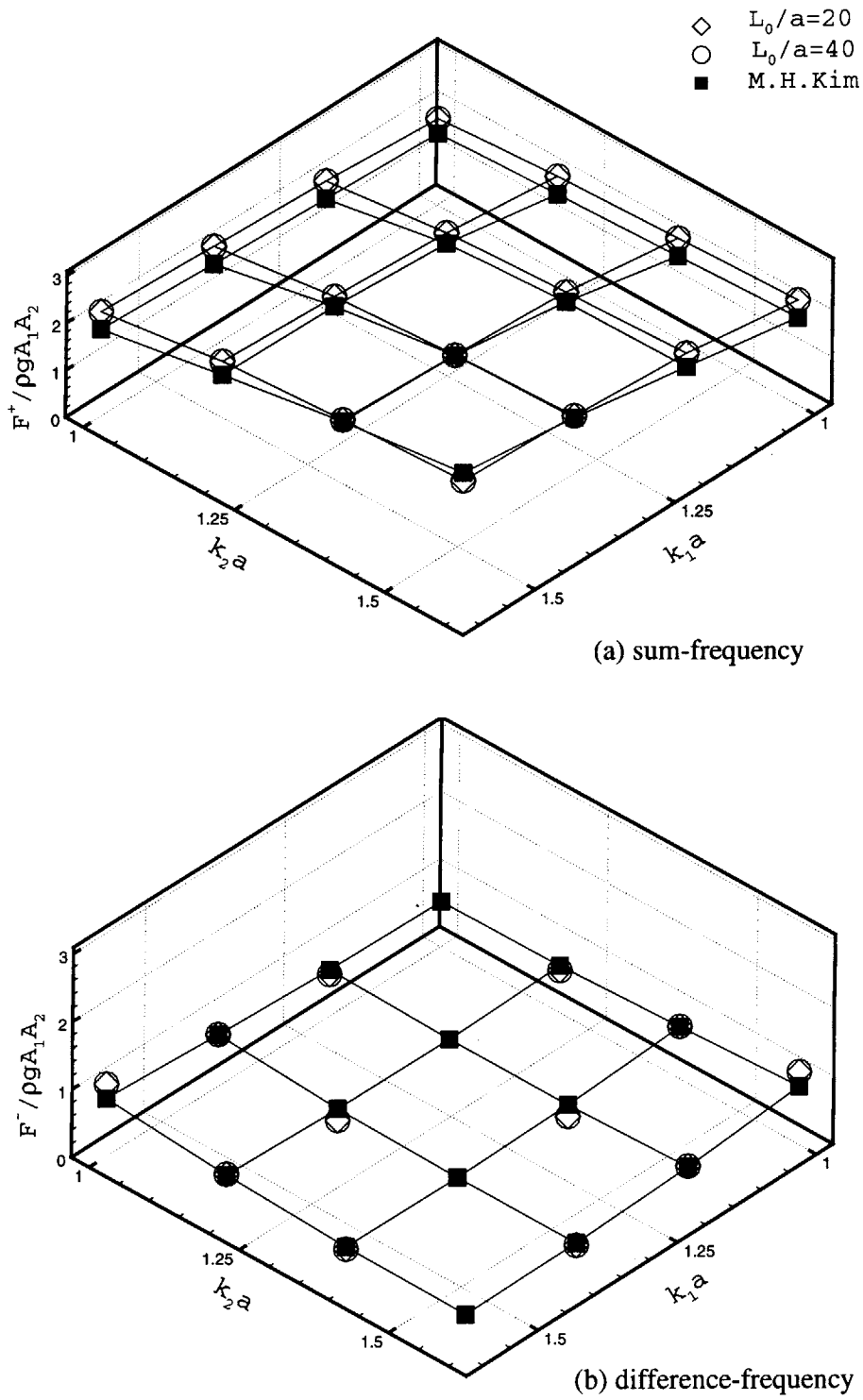


Figure 4-30: Four by four sum-frequency surge QTF matrix obtained from a single time history at multi waves : the same cylinder with Figure 4-23, different size of the artificial damping zone, (a) sum-frequency (b) difference-frequency

edge. Hence, the beach size is more important than the beach strength in this case.

The application to a realistic ocean spectrum is the most difficult part in this study. In the theoretical point of view, there is no significant difference in its application. However, in the viewpoint of computational effort, there is a big difference between previous cases and ocean spectra. For example, in the North Atlantic and Pacific Oceans, the $\omega$ values of the ocean-wave spectra vary between 0.2 and 2.0 rad/sec [16]. It should be noticed that this range is valid in the linear sense. Thus, for the second-order sum-frequency problem, the panel resolution must be fit up to $\omega = 4.0$. Furthermore, the different-frequency depends on the number of the discrete frequency, and it becomes very small if the number of considered frequency is a lot. In addition, the selection of a high cut-off frequency is not trivial since the ocean spectra have long tail at high frequency where the wave energy is not ignorable, particularly for the sum-frequency.

Figure 4-31 and 4-32 show the ITTC spectra and their discretizations for sea sate 5 and 6 in the North Atlantic Sea. The significant wave heights $H_s$ are 3.25m and 5.0m, and the modal wave periods $T_m$ are 9.7sec and 12.4sec, respectively. The one-sided ITTC spectrum takes the following form:

$$S(\omega) = 0.11 H_s^2 \frac{1}{2\pi} (\frac{2\pi}{\omega})^5 T_m^{-4} \; e^{-0.44(\omega T_m/2\pi)^{-4}} \tag{4.3}$$

It is well known that the incident wave amplitude $A_m$ of equation (2.13) becomes $\sqrt{2S(\omega_m)\Delta\omega}$ and the phase is arbitrary between 0 and $2\pi$. Figure 4-33 shows the instantaneous linear waves and the corresponding second-order wave profiles near a truncated cylinder with $d/a = 4.0$, A ITTC spectrum with sea state 5 was applied, and the spectrum was discretized into 20 frequencies. Like a monochromatic wave problem, the second-order high-frequency waves are very localized near the body.

Figure 4-34 shows the time signals of the wave amplitude at $(x, y) = (0, 0)$, the linear and second-order wave loads on the cylinder. The difference of these signals

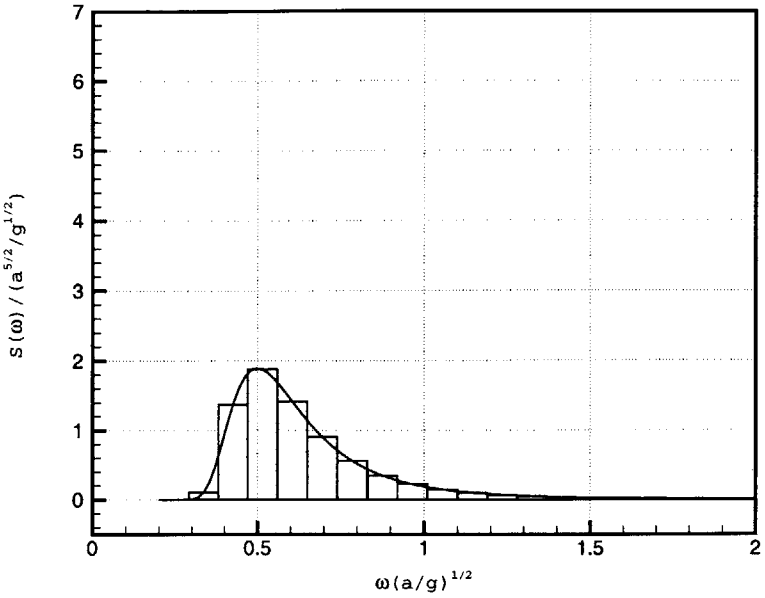


Figure 4-31: Discretization of ITTC spectrum at sea state 5 in the North Atlantic Sea : $H_s = 3.25m, T_m = 9.7sec$, 20 components

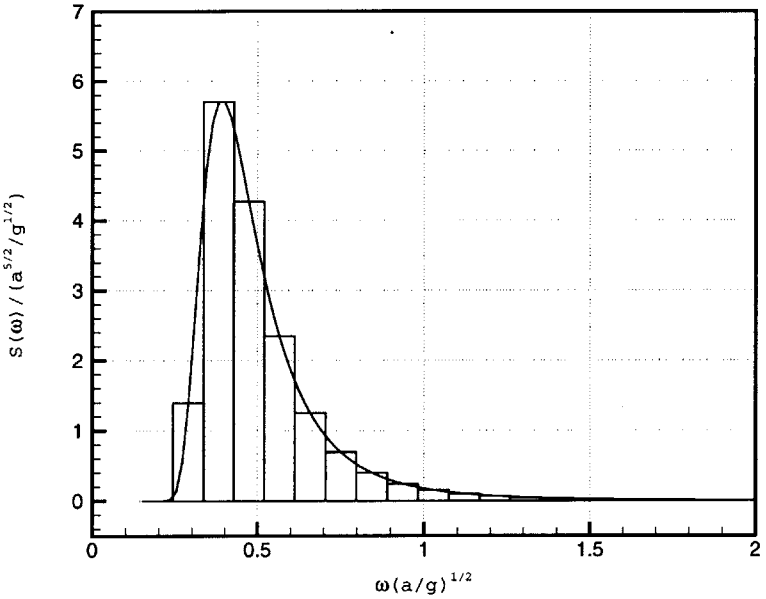


Figure 4-32: Discretization of ITTC spectrum at sea state 6 in the North Atlantic Sea : $H_s = 5.0m, T_m = 12.4sec$, 20 components

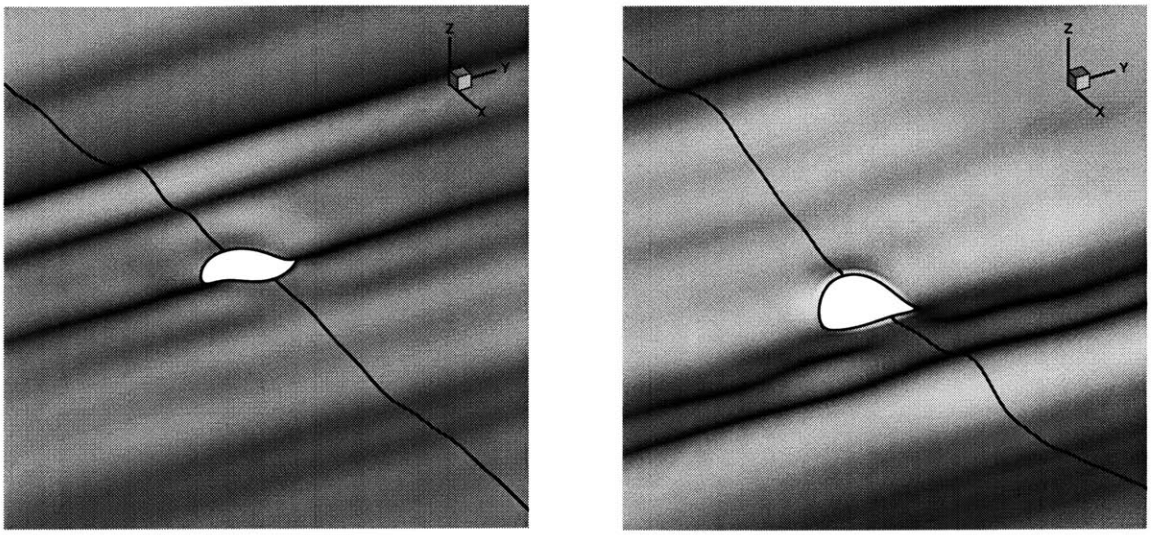

(a) Linear wave profiles

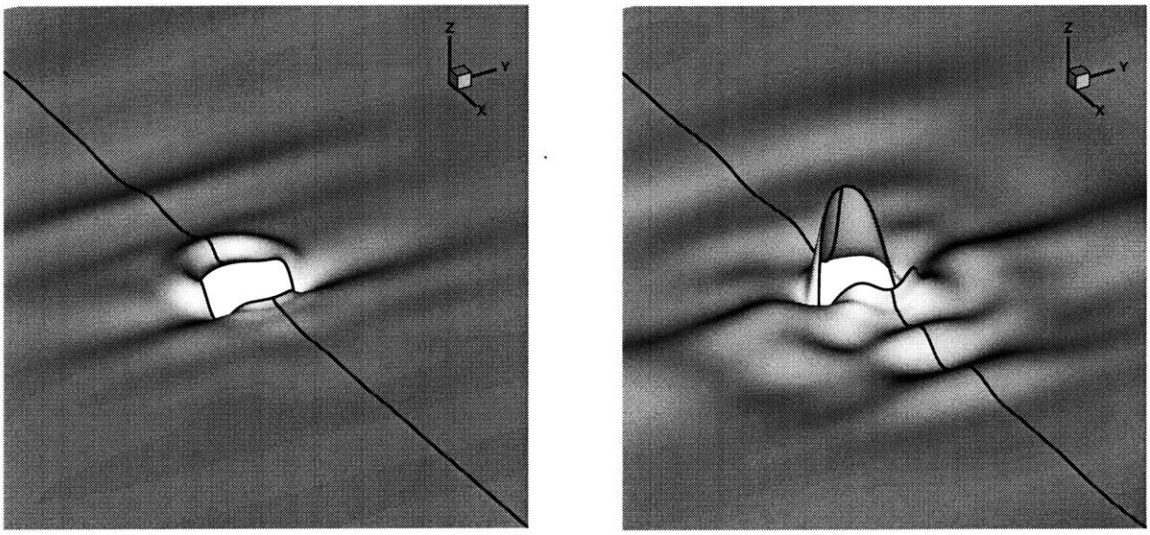

(b) Second-order wave profiles

Figure 4-33: The instantaneous linear and second-order wave profiles near a truncated cylinder : ITTC spectrum at sea state 5, $d/a = 4.0$

is the phase of the incident waves, and the phases are decided by a random number generator [78]. Therefore, three signals come from the same spectrum with the different phases of wave components. Particularly the time signals of the second-order forces are the mixtures of the sum- and difference-frequencies of 800($20\times20$ sum- and $20\times20$ difference-frequencies) components. From the comparison between the linear and second-order signals, it can be known that the second-order signals contribute more at high frequencies, as pointed by Sclavounos [70].

Figure 4-35 shows the time signals for the ITTC spectrum at sea state 6 with the different numbers of discretization. When the a spectrum is discretized, in general, the cut-off frequencies dictate the time segment and grid resolution. On the other hand, the number of frequencies influences on the simulation time and computational domain since the difference-frequency depends on the number of wave components. As shown in this figure, when the number of components becomes larger, the signal becomes more irregular.

If many computation results are collected for a given ocean spectrum, the second-order statistic characteristics can be observed, using some signal-processing techniques. This issue is a challenging topic, which can be extended from the present study, and eventually it may replace an expensive experiment. The numerical time-domain approach for the realistic ocean spectra is in a poorly mature state. However, under the basis of the greatly fast development of computational environment, a full simulation of the nonlinear wave loads in the realistic random ocean wave will be getting popular. The present computation was carried out as a bench-mark test of such simulation.

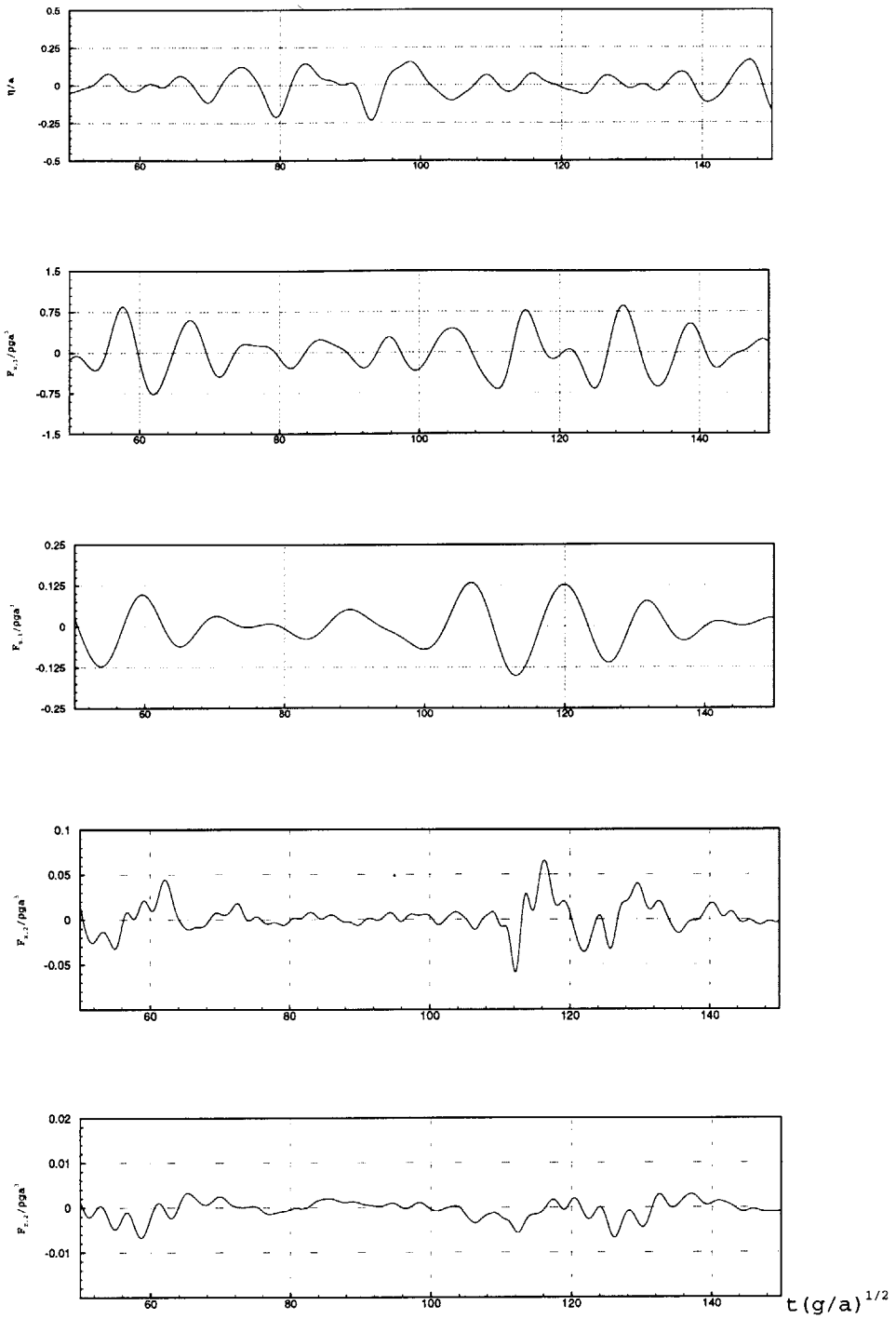


(a) case 1

Figure 4-34: Time signals of the linear wave elevation, linear and second-order forces : ITTC spectrum in Figure 4-31, from top ; wave elevation, the linear surge and heave forces, the second-order surge and heave forces

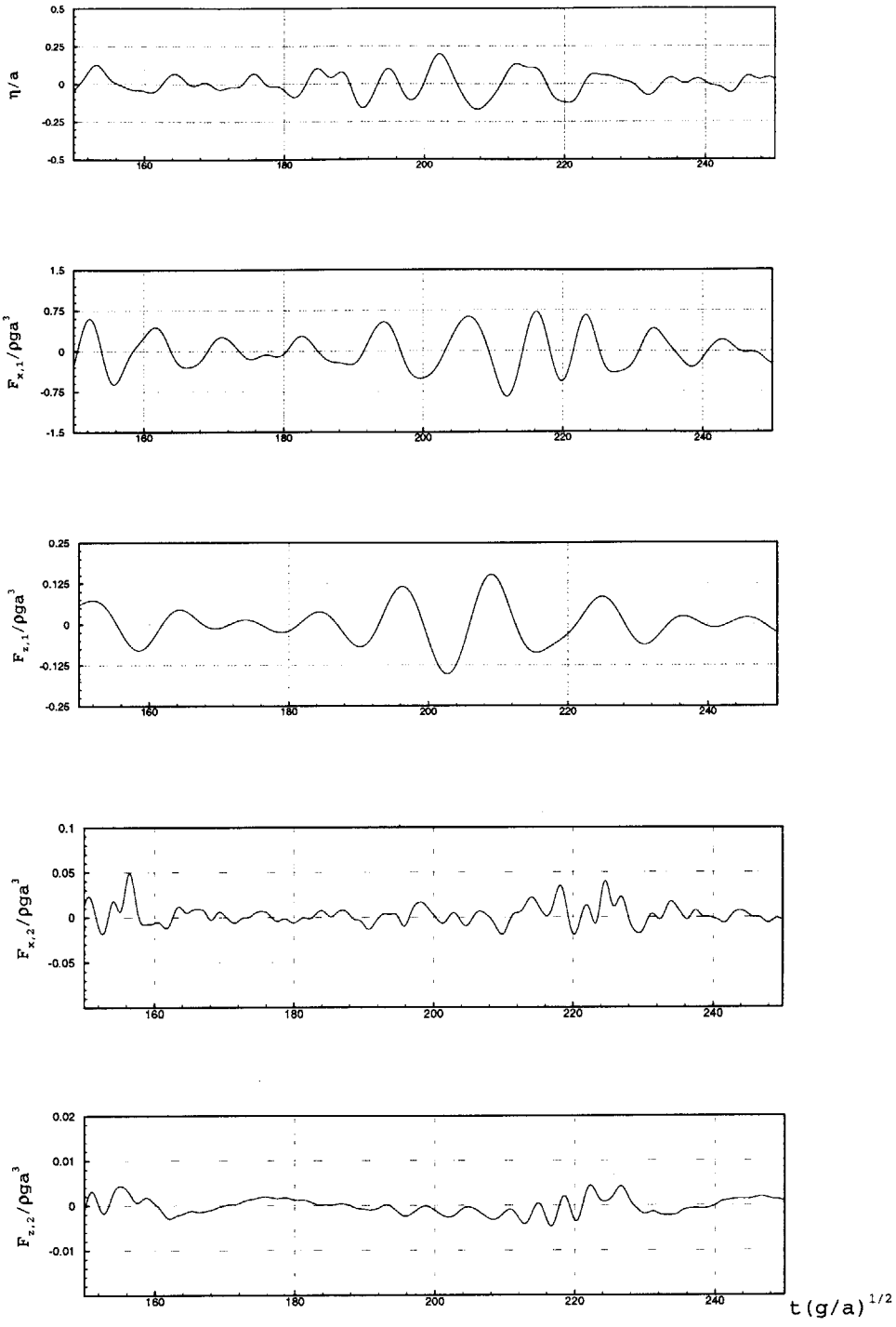


(b) case 2
Figure 4-34 (continued)

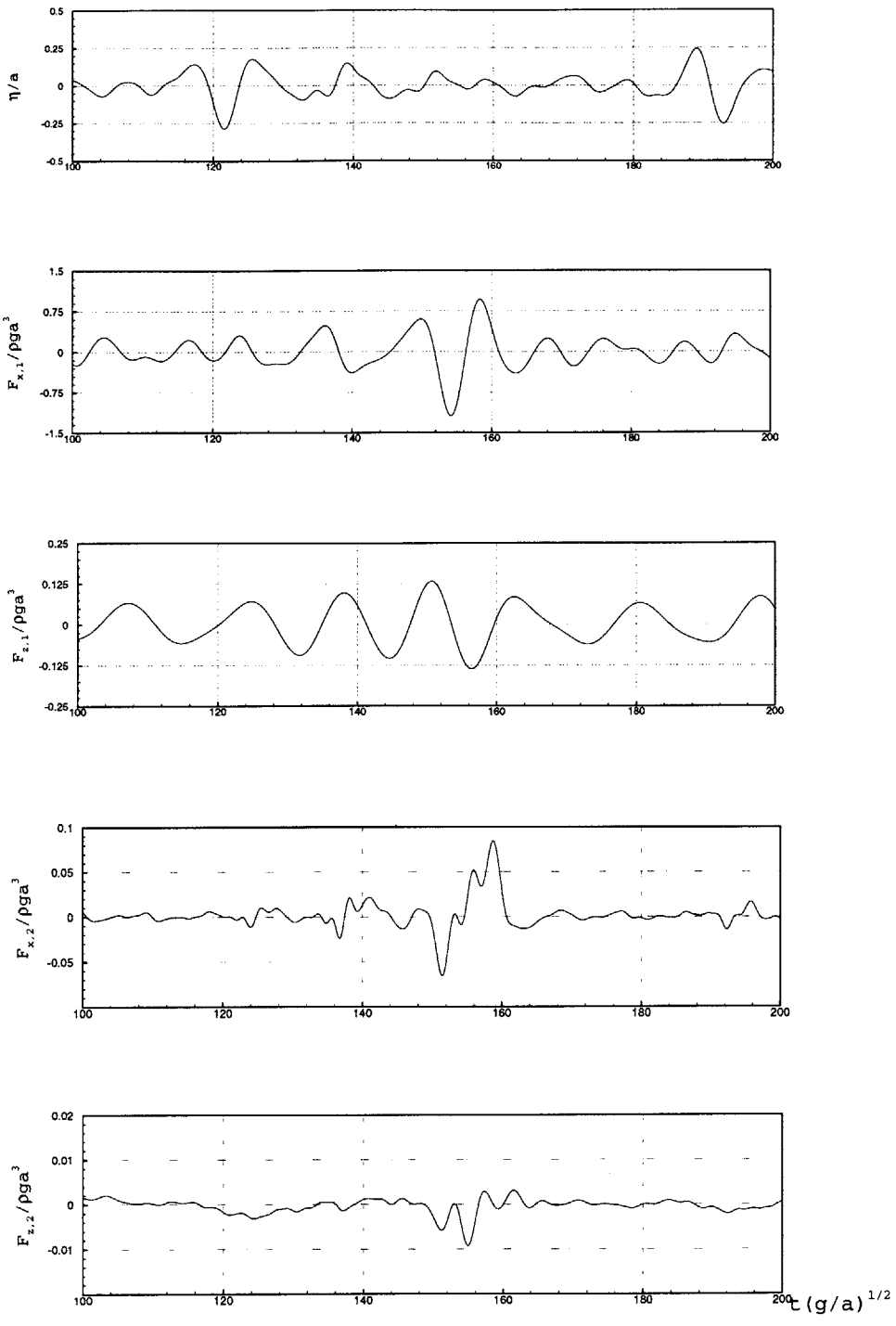


(c) case 2
Figure 4-34 (continued)

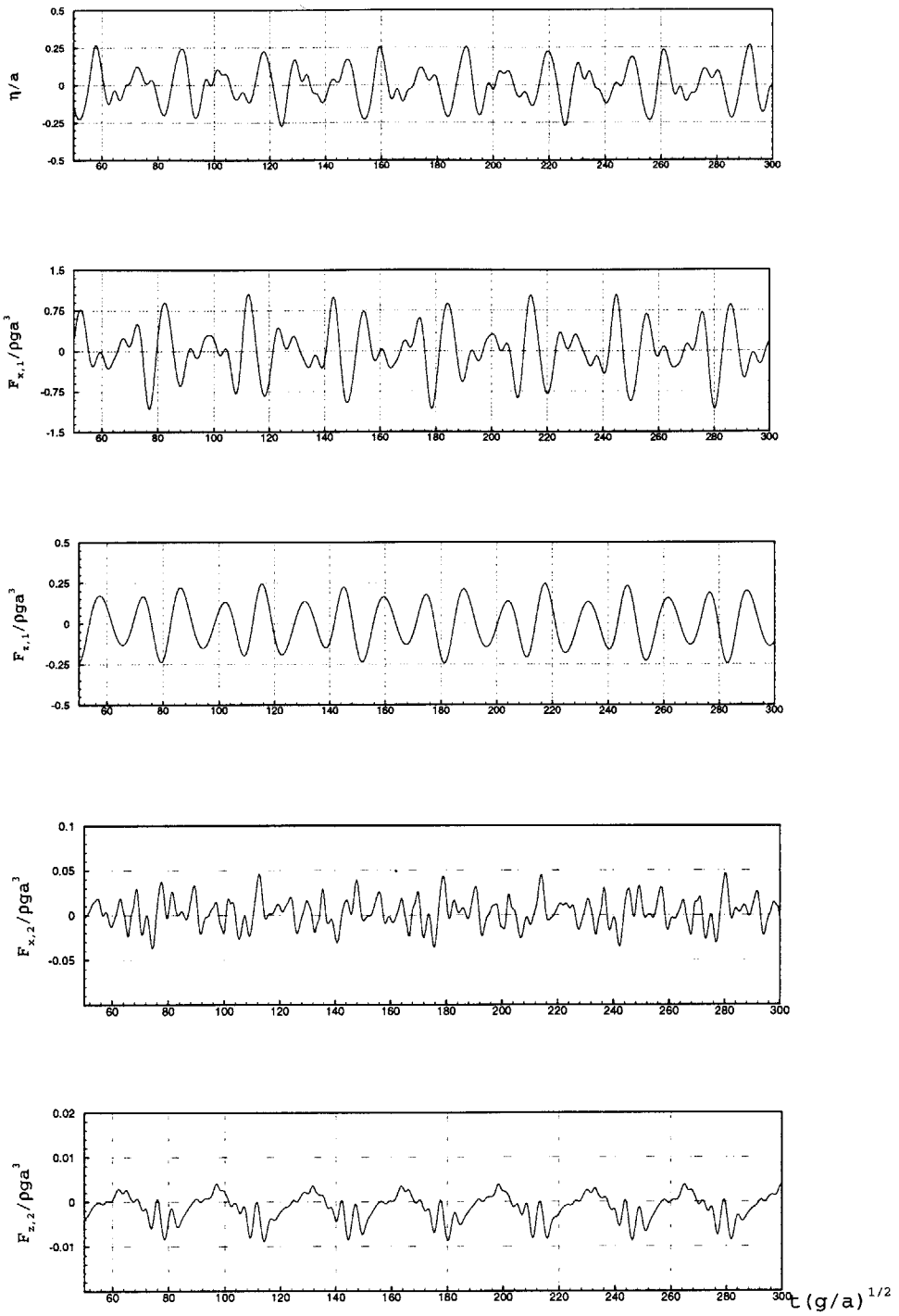


(a) 10 frequencies

Figure 4-35: Time signals of the linear wave elevation, linear and second-order forces : ITTC spectrum in Figure 4-32, from top ; wave elevation, the linear surge and heave forces, the second-order surge and heave forces

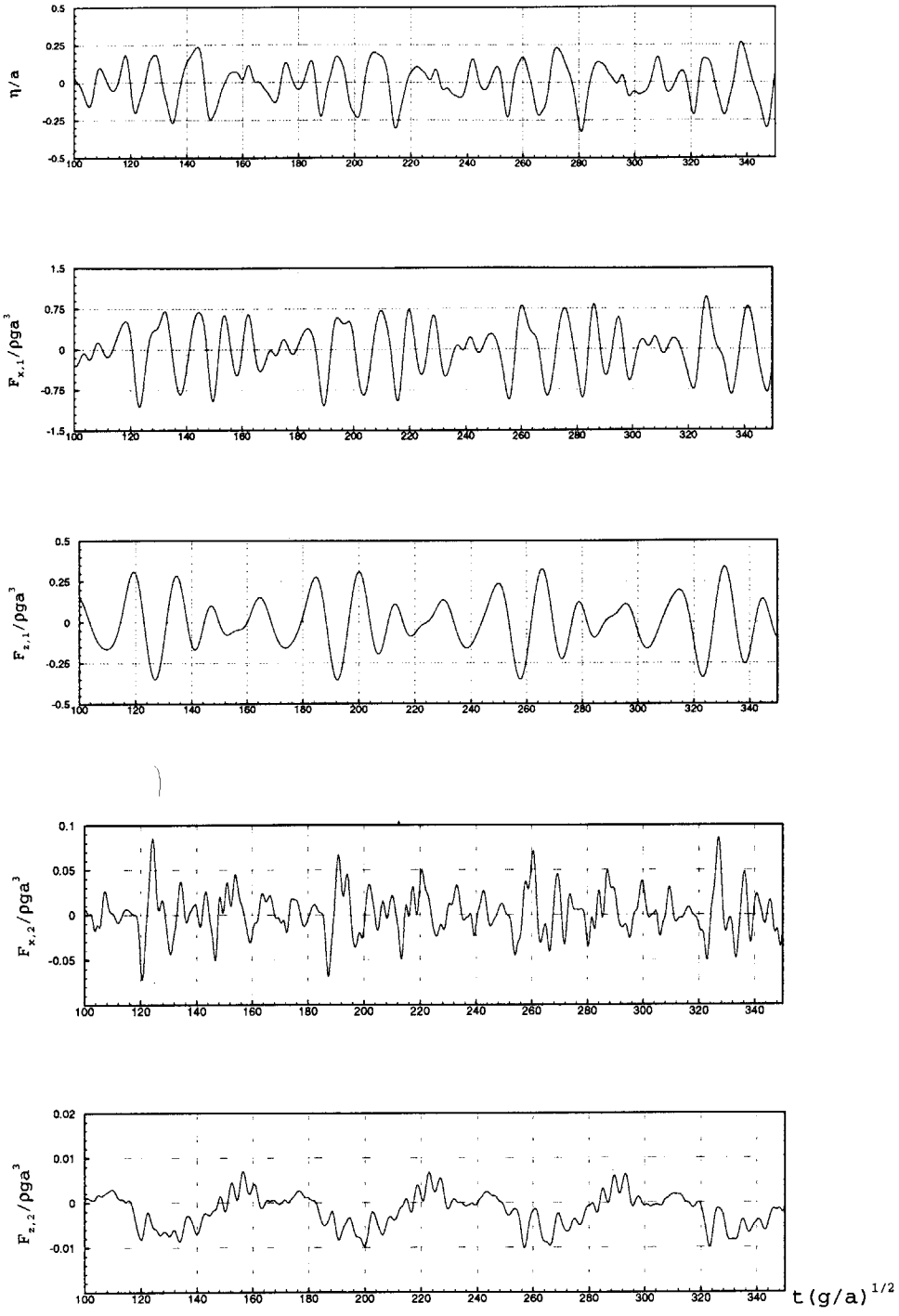


(b) 20 frequencies
Figure 4-35 (continued)

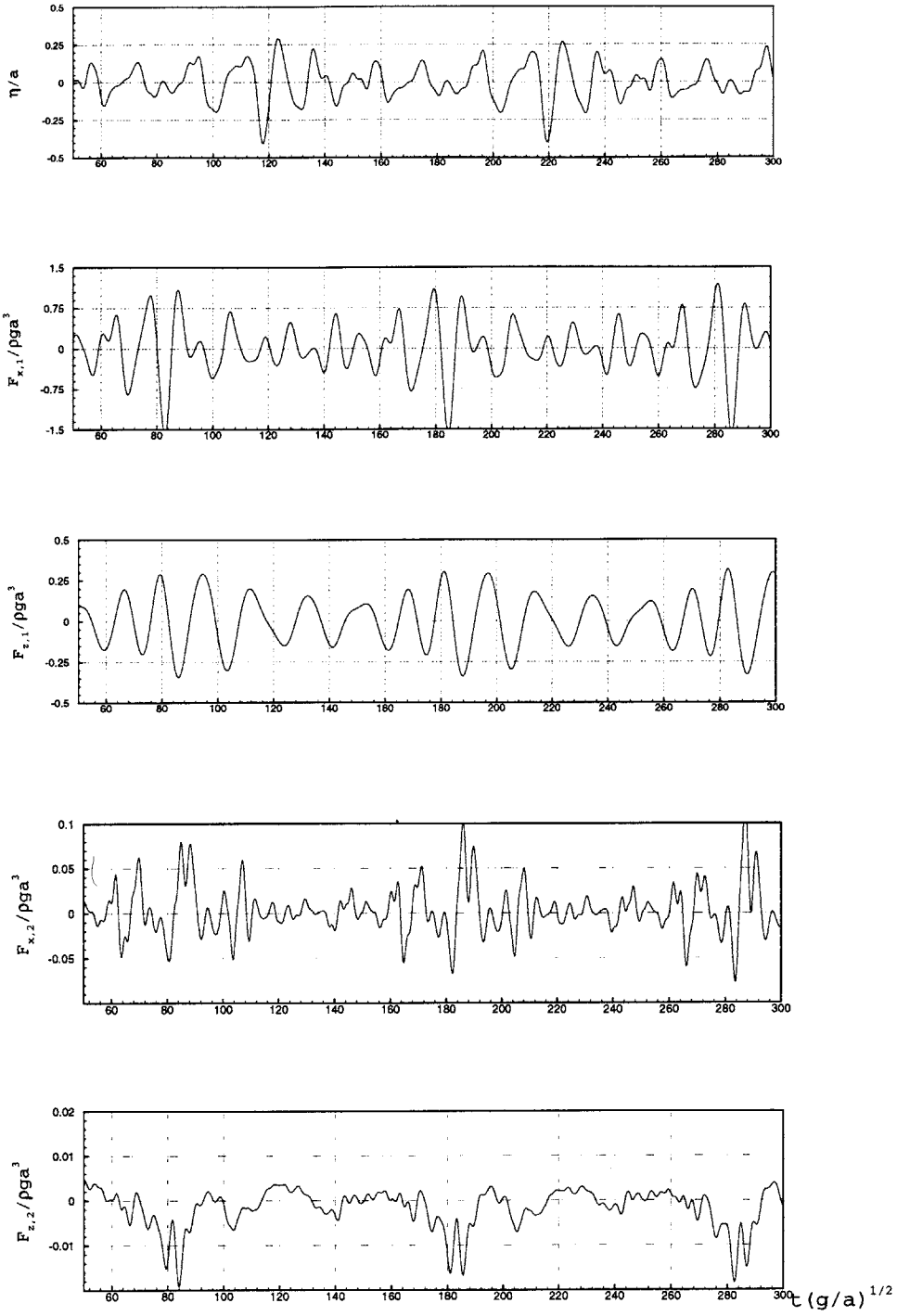


(c) 30 frequencies
Figure 4-35 (continued)

# Chapter 5

# Conclusions & Contributions

A three-dimensional time-domain Rankine panel method has been applied to solve the linear and second-order free-surface problems around the truncated or bottom-mounted circular cylinders and cylinder array. The present method applies the bi-quadratic B-spline function for the discrete representation of the velocity potential, wave elevation, and normal flux on the fluid boundaries. For the time integration, a modified Euler scheme is used.

One of the important contributions in the present part is the thorough theoretical study on the numerical scheme. Using the discrete Fourier transform, it was proved that the present numerical method has the consistency which ensures that the wave disturbance propagates over the free surface panel mesh with proper dispersion. Furthermore, the temporal stability condition was derived to offer a stable computation.

An artificial beach is applied in order to impose the radiation condition. The kinematic free-surface boundary condition is modified in the artificial beach to damp the normal flux without a significant change of wave system. This thesis introduces a deep investigation on the damping parameters. It is found that the sensitivity of the damping parameters is not significant in a wide range. In addition, a low-pass filter is applied to eliminate saw-tooth waves which may prevent stable time-marching.

The linear radiation problem is solved in order to test the accuracy and efficiency of the developed computer code. The time-domain solution is converted to the frequency

domain using the Fourier transformation, which is based on an integral method. The hydrodynamic forces are compared with WAMIT, and a nice agreement was shown.

The major contribution of the present part is to compute the linear and second-order diffraction forces on the truncated and bottom-mounted cylinders, particularly for the sum-frequency. The results are compared with other benchmark computations, and a very encouraging agreement was shown. The same is found to be the case with the wave elevation computed around the waterline of a bottom-mounted cylinder for which experimental measurements are available. Furthermore, the local second-order standing waves generated by interference of the scattered and incoming wave are well simulated using the present method.

To aim the realistic wave spectra, the computation was carried out for random wave with multi frequencies. It is found that the present computer code simulates all the components of the linear and second-order forces with good agreement. Based on a thorough parametric study, some bench-mark computations were performed for the realistic ITTC spectra. Therefore, the method emerges as a promising candidate for the study of second and higher order wave interactions with realistic offshore structures in a monochromatic or random ambient wave records.

# APPENDIX

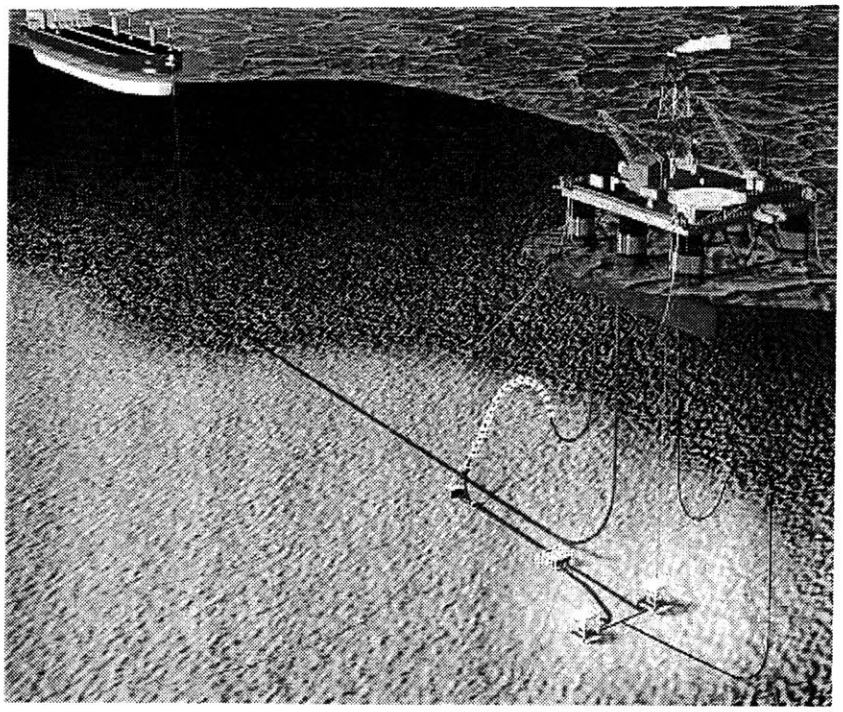

# Appendix A

# Fourier Transformation of A Finite-Depth Green Function

Consider a line distribution of the three-dimensional wave source along $x$ axis at $y = 0$ and $z = z_0$, and put $Q(x,t)$ is the strength which is a function of $x$ and time. The depth is assumed finite and constant. Focusing on the stationary problem, $Q(x,t)$ and the velocity potential is put as

$$Q(x,t) = \Re\{q(x)e^{i\omega t}\} \tag{A.1}$$

$$\Phi(x,t) = \Re\{\phi(x)e^{i\omega t}\} \tag{A.2}$$

Here, all notations are same with Part I.

In the realm of linear potential theory, the velocity potential $\phi(x,y,z)$ is given by the following equations :

$$\nabla^2\phi(x,y,z) = q(x)\delta(y)\delta(z-z_o) \qquad \text{in fluid domain,} \tag{A.3}$$

$$-\omega^2\phi + g\frac{\partial\phi}{\partial z} = 0 \qquad \text{on } z = 0, \tag{A.4}$$

$$\frac{\partial\phi}{\partial z} = 0 \qquad \text{on } z = -h. \tag{A.5}$$

Now consider the double Fourier transform to above equations with respect to $x$

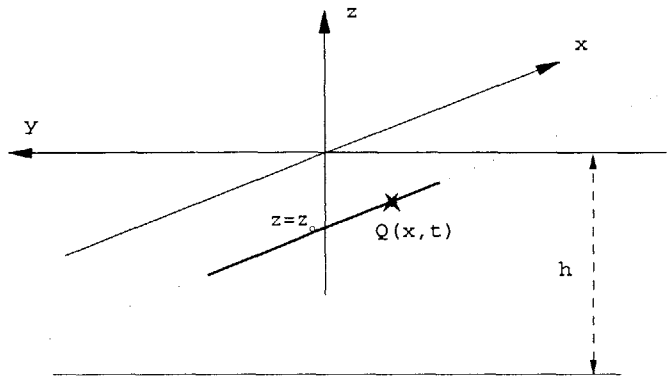


Figure A-1: Line source along $x$ axis at $z = z_o$

and $y$. The first equation is written in the Fourier domain as

$$\{\frac{\partial^2}{\partial z^2} - (u^2 + v^2)\}\phi^{**}(u, v; z) = q^*(u)\delta(z - z_o) \tag{A.6}$$

Moreover, other two equations become

$$(-\omega^2 + g\frac{\partial}{\partial z})\phi^{**} = 0 \tag{A.7}$$

$$\frac{\partial \phi^{**}}{\partial z} = 0 \tag{A.8}$$

When $z \neq z_o$, the solution of an ordinary differential equation (A.6) has a form,

$$\phi^{**} = Ae^{sz} + Be^{-sz} \tag{A.9}$$

where $s = \sqrt{u^2 + v^2}$, and $A$ and $B$ are the coefficients which are supposed to be obtained from other two boundary conditions.

Substituting equation (A.9) to (A.7) and (A.8), we can get

$$\phi^{**} = \begin{cases} B(\frac{\omega^2+gs}{-\omega^2+gs}e^{sz} + e^{-sz}) & z_o < z < 0 \\ C\cosh\{s(z+h)\} & -h < z < z_o \end{cases} \tag{A.10}$$

where $C$ is a constant.

Now, consider the integral of equation (A.6) such that

$$\int_{z_o-\epsilon}^{z_o+\epsilon}\{\frac{\partial^2}{\partial z^2}-(u^2+v^2)\}\phi^{**}(u,v;z)dz=\int_{z_o-\epsilon}^{z_o+\epsilon}q^*(u)\delta(z-z_o)dz \tag{A.11}$$

or

$$\frac{\partial}{\partial z}\phi^{**}|_{z_o-\epsilon}^{z_o+\epsilon}=q^*(u) \tag{A.12}$$

Therefore $\phi^{**}$ is continuous on $z=z_o$. From equation (A.10), the continuity condition produces

$$C=\frac{\frac{\omega^2+gs}{-\omega^2+gs}e^{sz_o}+e^{-sz_o}}{\cosh\{s(z_o+h)\}}B \tag{A.13}$$

Substituting this result to equation (A.11), we can get

$$B=-\frac{q^*}{s}\frac{1}{K[\tanh\{s(z_o+h)\}-1]e^{sz_o}+[\tanh\{s(z_o+h)\}+1]e^{-sz_o}} \tag{A.14}$$

with

$$K=\frac{\omega^2+gs}{-\omega^2+gs}, \tag{A.15}$$

and it leads to the explicit form of $\phi^{**}$.

Our interest is when $z_o\to 0$. In this case, it can be written as

$$\phi^{**}(u,v;z)=-q^*\frac{\cosh\{s(z+h)\}}{s\cosh(sh)\{\tanh(sh)+\frac{K-1}{K+1}\}}. \tag{A.16}$$

Using

$$\frac{K-1}{K+1}=-\frac{\omega^2}{g}, \tag{A.17}$$

we can write $\phi^{**}$ with the following form :

$$\phi^{**}(u,v;z) = -q^* \frac{\cosh\{\sqrt{u^2+v^2}(z+h)\}}{\sqrt{u^2+v^2}\cosh\{\sqrt{u^2+v^2}h\}[\tanh\{\sqrt{u^2+v^2}h\} - \frac{\omega^2}{g}]} \tag{A.18}$$

and thus

$$\phi(x,y,z) = \frac{1}{(2\pi)^2}\int_{-\infty}^{\infty}\int_{-\infty}^{\infty} \phi^{**}(u,v;z)\, e^{i(ux+vy)}\, dudv \tag{A.19}$$

Recalling equation (3.2) of Part I, we can conclude that the Fourier transformation of $G(x,y,z)$ with respect to $x$ is

$$\begin{aligned} G^*(u;y,z) &= -\frac{1}{2\pi}\int_{-\infty}^{\infty} dv\, e^{ivy} \times \\ &\quad \frac{1}{\cosh\{\sqrt{u^2+v^2}h\}} \frac{\cosh\{\sqrt{u^2+v^2}(z+h)\}}{[\sqrt{u^2+v^2}\tanh\{\sqrt{u^2+v^2}h\} - \frac{\omega^2}{g}]} \end{aligned} \tag{A.20}$$

This result was derived by Borresen [6] including forward speed. When there is a forward speed $U$, $\omega$ should be replaced with $\omega - Uu$. This recovers the deep water limit when $h \to \infty$.

# Appendix B

# Singularities on the Kernel

Consider a series which is defined as follows :

$$G_{2D,S}(y) = -\sum_{n=1}^{\infty} \frac{m_n}{hm_n^2 + h\nu^2 - \nu}\, e^{-m_n|y|} \tag{B.1}$$

When $y = 0$, the last term of equation (3.30) of Part I is recovered. That is to say, $G_{2D,S}(y)$ is the local wave component of a two-dimensional Green function with $z = 0$. When $n \to \infty$, $m_n$ becomes approximately $n\pi/h$. Then $G_{2D,S}(y)$ can be written as

$$G_{2D,S} = -\sum_{n=1}^{\infty} \{\frac{m_n}{hm_n^2 + h\nu^2 - \nu}\, e^{-m_n|y|} - \frac{1}{n\pi}\, e^{-\frac{n\pi}{h}|y|}\} + I \tag{B.2}$$

where

$$\begin{aligned} I &= -\sum_{n=1}^{\infty} \frac{1}{n\pi} e^{-\frac{n\pi}{h}|y|} \\ &= \frac{1}{\pi} \ln|1 - e^{\frac{i\pi y}{h}}| \\ &= \frac{1}{\pi} \ln(\frac{\pi y}{h}) + \frac{1}{\pi} \ln|\frac{1 - e^{-\frac{n\pi}{h}|y|}}{-\frac{\pi}{h}|y|}| \end{aligned} \tag{B.3}$$

Hence, when $y \to 0$, $G_{2D,S}$ can be approximated as

$$G_{2D,S} \approx -\sum_{n=1}^{\infty}\{\frac{m_n}{hm_n^2+h\nu^2-\nu}-\frac{1}{n\pi}\}+\frac{1}{\pi}\{\ln\pi-\ln h+\lim_{\epsilon\to 0}\ln|\epsilon|\} \tag{B.4}$$

The last term is a logarithmic singularity of interest.

The singularities in the three-dimensional Green function are in $Y_o(x)$ and the series of $K_o(x)$. As we know, an asymptotic value of $Y_o(x)$ for small $x$ is $\ln(x)/2$, and this is one singularity in the kernel of the integral equation of Part I. The other singularity is in the series with $K_o(x)$. In order to observe the singularity, define a series term, $G_{3D,S}$, as

$$G_{3D,S} = -\frac{1}{\pi}\sum_{n=1}^{\infty}\frac{m_n^2}{hm_n^2+h\nu^2-\nu}K_o(m_n|x|) \tag{B.5}$$

This term is a part of the last term in equation (3.30) in Part I.

Recalling the fact that $m_n$ approaches $n\pi/h$ if $n$ becomes large, the series can be rewritten as

$$\begin{aligned} G_{3D,S} &= -\frac{1}{\pi}\sum_{n=1}^{\infty}\{\frac{m_n^2}{hm_n^2+h\nu^2-\nu}K_o(m_n|x|)-\frac{1}{h}K_o(\frac{n\pi}{h}x)\} \\ &\quad -\frac{1}{2\pi}\{\frac{1}{x}+\frac{1}{h}(\gamma+\ln\frac{x}{4h})+\frac{2}{h}\sum_{n=1}^{\infty}[\frac{1}{\sqrt{4n^2+(\frac{x}{h})^2}}-\frac{1}{2n}]\} \end{aligned} \tag{B.6}$$

where $\gamma$ is the Euler constant. This is derived using the following formula (Prudnikov & et al [60], pp 698),

$$\begin{aligned} \sum_{n=1}^{\infty}\cos(na)K_o(nx) &= \frac{\pi}{2\sqrt{x^2+a^2}}+\frac{1}{2}(\gamma+\ln\frac{x}{4\pi}) \\ &\quad +\frac{\pi}{2}\sum_{n=1}^{\infty}\{\frac{1}{\sqrt{(2n\pi-a)^2+x^2}}-\frac{1}{2n\pi}\} \\ &\quad +\frac{\pi}{2}\sum_{n=1}^{\infty}\{\frac{1}{\sqrt{(2n\pi+a)^2+x^2}}-\frac{1}{2n\pi}\} \end{aligned} \tag{B.7}$$

There is a $1/r$ singularity in equation (B.7). This singularity has to be observed

in the integral sense since the line distribution is applied. The integral of $1/x$ is $\ln x$, and it is canceled out with the logarithmic singularity of equation (B.4) as $x \to 0$. Therefore the kernel of integral equation (3.30) in Part I is finite at any $x$.

# Appendix C

# The Extension of NIIRID to Finite Depth

Slender-body theory requires the solution of the sectional boundary value problem. There have been many studies for two-dimensional wave problems, but Frank's closed-fit method [17] is the most popular for strip theory. The present computation was carried out using the extended version of NIIRID. NIIRID [68] was developed at MIT for infinite depth. The method of solution of NIIRID is based on Green's theorem, which is used to obtain a Fredholm integral equation of the second kind for the velocity potential on the body boundary. The body section is approximated by the connection of straight segments, and the midpoint of each segment is selected as the collocation points.

Consider the line segments on a certain section, shown in Figure C-1. The following equation is supposed to be solved,

$$\phi_i + \sum_{j=1}^{N} \phi_j \int_j \frac{\partial}{\partial n} G_{2D}(x_i, y_i; \xi, \eta) ds = \sum_{j=1}^{N} (\frac{\partial \phi}{\partial n})_j \int_j G_{2D}(x_i, y_i; \xi, \eta) ds \qquad \text{(C.1)}$$

where the subscript indicates the panel index. Since we knows the body boundary conditions, equation (C.1) leads to a linear matrix equation for unknown $\phi_j$. In most cases, the half domain is enough for geometric input because of its symmetry with

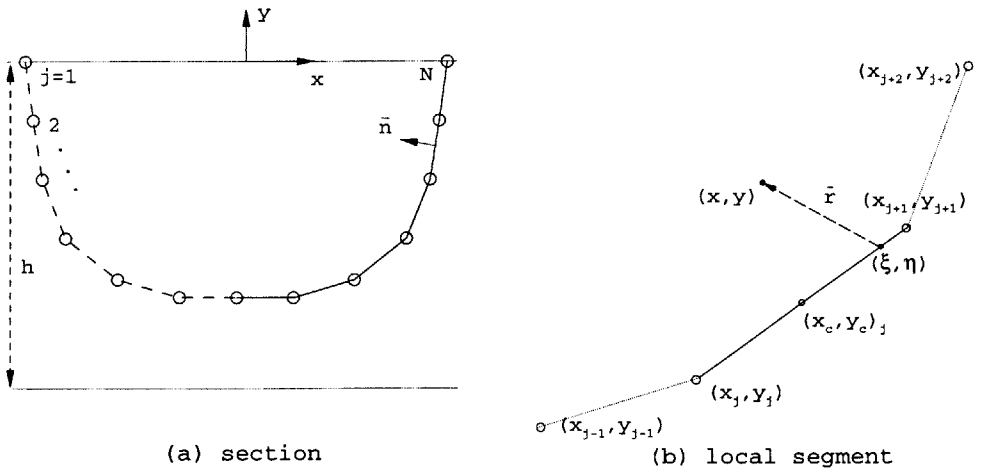


Figure C-1: Local coordinate system for a two-dimensional segment

respect to the center-plane.

The major task in assembling the matrix equation is the numerical integrals of $G_{2D}$ and $\frac{\partial}{\partial n}G_{2D}$. A two-dimensional finite-depth wave Green function can be written with a series form,

$$G_{2D}(x, y, t; \xi, \eta) = \Re(G_o e^{i\omega t}) \tag{C.2}$$

with

$$\begin{aligned} G_o &= G_1 + G_2 + G_3 \\ &= \frac{i}{m_o}\frac{m_o^2 - \nu^2}{hm_o^2 - h\nu^2 + \nu}\cosh\{m_o(y+h)\}\cosh\{m_o(\eta+h)\}e^{-im_o|x-\xi|} \\ &\quad -\frac{1}{2}\sum_{n=1}^{\infty}\frac{1}{m_n}\frac{m_n^2 + \nu^2}{hm_n^2 + h\nu^2 - \nu}\cos\{m_n(y+\eta+2h)\}e^{-m_n|x-\xi|} \\ &\quad -\frac{1}{2}\sum_{n=1}^{\infty}\frac{1}{m_n}\frac{m_n^2 + \nu^2}{hm_n^2 + h\nu^2 - \nu}\cos\{m_n(y-\eta)\}e^{-m_n|x-\xi|} \end{aligned} \tag{C.3}$$

where $(\xi, \eta)$ is a source point, and all other notations are the same with Part I.

The line integral of $G_{2D}$ is required for the application of Green's second identity. Since $G_{2D}$ has a logarithmic singularity, it is desirable to integrate analytically this

singularity over a segment. The singularity is in $G_3$ term which can be rewritten as

$$\begin{aligned} G_3 &= -\frac{1}{2}\sum_{n=1}^{\infty}\{\ \frac{1}{m_n}\frac{m_n^2+\nu^2}{hm_n^2+h\nu^2-\nu}\cos\{m_n(y-\eta)\}e^{-m_n|x-\xi|} \\ &\quad -\frac{1}{n\pi}\cos\{\frac{n\pi}{h}(y-\eta)\}\ e^{-\frac{n\pi}{h}|x-\xi|}\ \} \ +\ J \end{aligned} \tag{C.4}$$

where

$$J = -\sum_{n=1}^{\infty}\frac{1}{2n\pi}\cos\{\frac{n\pi}{h}(y-\eta)\}e^{-\frac{n\pi}{h}|x-\xi|} \tag{C.5}$$

Like Appendix B, we can write $J$ as

$$\begin{aligned} J &= \frac{1}{2\pi}\ln|1-e^{\frac{\pi}{h}\{-|x-\xi|+i(y-\eta)\}}|the \\ &= \frac{1}{2\pi}\ln|-|x-\xi|+i(y-\eta)|+\frac{1}{2\pi}\ln|\frac{1-e^{\frac{\pi}{h}\{-|x-\xi|+i(y-\eta)\}}}{-|x-\xi|+i(y-\eta)}| \end{aligned} \tag{C.6}$$

$J$ has a logarithmic singularity which an analytic integration is possible. However, the regular wave part is hard to integrate analytically. Gaussian quadrature is applied in the present study, and the integral is approximated as

$$\int_{(x_1,y_1)}^{(x_2,y_2)}\{G_{2D}(r)-\ln|r|\}dS \approx \sum_{k=0}^{N}W_k\{G_{2D}(r_k)-\ln|r_k|\} \tag{C.7}$$

where $W_k$ is a weight and $r_k$ is the distance between a field point and the point which Gaussian quadrature is applied(Figure C-1).

The analytic treatment of the velocity components induced by a line distribution of wave source is more delicate than that of the velocity potential. Especially when a field point approaches the singularity line, the convergence of series is very slow. For example, let's consider a term,

$$\frac{1}{m_n}\frac{m_n^2+\nu^2}{hm_n^2+h\nu^2-\nu}\cos\{m_n(y-\eta)\}e^{-m_n|x-\xi|} \tag{C.8}$$

The derivative with respect to $x$ is

$$-sgn(x-\xi)\ \frac{m_n^2+\nu^2}{hm_n^2+h\nu^2-\nu}\cos\{m_n(y-\eta)\}e^{-m_n|x-\xi|} \tag{C.9}$$

When $n$ is large, $m_n$ approach $\frac{n\pi}{h}$ and $\frac{m_n^2+\nu^2}{hm_n^2+h\nu^2-\nu}$ approach to $\frac{1}{h}$. If $x-\xi$ is very small, then equation (C.8) has a convergence of $1/n$, while equation (C.9) has much slower convergence.

Therefore, in the extension of NIIRID, the velocity components are obtained by numerical difference. Since the convergence of the velocity potential is much faster than the velocity computation, the numerical difference is much faster than the direct computation of derivatives. In the present work, a central difference is adapted.

# Appendix D

# Body-Fitted Grid on Free Surface

A grid system influences on solution accuracy. So a systematic study for grid resolution, aspect ratio, and skewness is necessary in panel method. The stability analysis performed in this study helps to predict some effects of the grid system, but that information is very limited and difficult to analyze. In most cases, the grid dependency is observed by computational experience.

One of issues in grid generation is how to distribute panels on free surface near a body. A circular cylinder is a simple model in this viewpoint. However, it is not simple to generate a proper grid system near a offshore structure or a ship. A nice grid system minimizes computer storage and computational time, and it makes it possible to reduce numerical error and instability. Furthermore it resolves physical details near the body.

In the present computation, a differential coordinate system is used in order to generate a body-fitted grid system, in particular near the body. The differential coordinate system is popular in Finite Difference Method (FDM) for viscous flow. In this method, the physical coordinates are mapped on a new pseudo coordinate system. The transformation between two coordinate systems may be any kind of differential operator, elliptic, hyperbolic or parabolic. However, the transformation should be unique. The present study applies Poisson equation, a well-known elliptic equation.

Define a new coordinate system, $(\xi, \eta)$. Assume $(\xi, \eta)$ satisfies

$$\nabla^2 \xi = P(\xi) \tag{D.1}$$

$$\nabla^2 \eta = Q(\eta), \tag{D.2}$$

where $\nabla$ is the gradient with respect to the physical coordinates, $(x, y)$. $P(\xi)$ and $Q(\eta)$ is the forcing terms, so called control functions. Then we can rewrite above Poisson equations with $(\xi, \eta)$ as independent variables,

$$\alpha \frac{\partial^2 x}{\partial \xi^2} - 2\beta \frac{\partial^2 x}{\partial \xi \partial \eta} + \gamma \frac{\partial^2 x}{\partial \eta^2} = -J^2 (\frac{\partial x}{\partial \xi} P + \frac{\partial x}{\partial \eta} Q) \tag{D.3}$$

$$\alpha \frac{\partial^2 y}{\partial \xi^2} - 2\beta \frac{\partial^2 y}{\partial \xi \partial \eta} + \gamma \frac{\partial^2 y}{\partial \eta^2} = -J^2 (\frac{\partial y}{\partial \xi} P + \frac{\partial y}{\partial \eta} Q) \tag{D.4}$$

where

$$\alpha = (\frac{\partial x}{\partial \eta})^2 + (\frac{\partial y}{\partial \eta})^2 \tag{D.5}$$

$$\beta = \frac{\partial x}{\partial \xi} \frac{\partial x}{\partial \eta} + \frac{\partial y}{\partial \xi} \frac{\partial y}{\partial \eta} \tag{D.6}$$

$$\gamma = (\frac{\partial x}{\partial \xi})^2 + (\frac{\partial y}{\partial \xi})^2 \tag{D.7}$$

$$J = \frac{\partial x}{\partial \xi} \frac{\partial y}{\partial \eta} - \frac{\partial x}{\partial \eta} \frac{\partial y}{\partial \xi} \tag{D.8}$$

Boundary conditions are necessary, and the $x, y$ coordinates on boundary grids must be enforced. The $x, y$ coordinates along the waterline of the body are given, while the coordinates along other edge grids should be decided properly.

Now these equations can be solved to obtain the physical coordinates, $x$ and $y$, which are mapped on a regular rectangular grid of $\Delta\xi = \Delta\eta = 1$ (Figure D-1). Taking the advantage of a rectangular grid, the finite difference method is used to solve the equations. For example,

$$\frac{\partial^2 x}{\partial \xi^2} = x_{i+1,j} - 2x_{i,j} + x_{i-1,j} \tag{D.9}$$

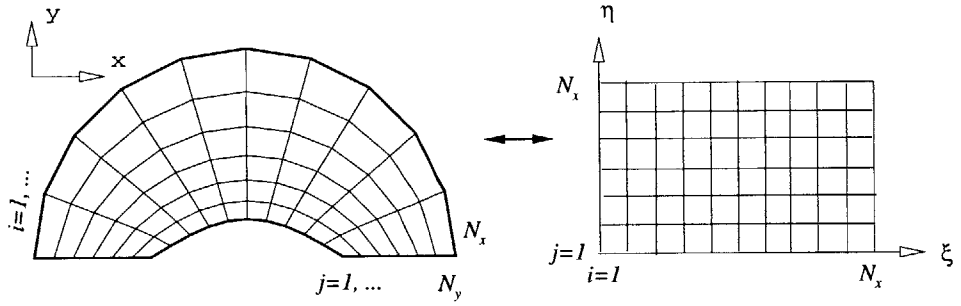


Figure D-1: Coordinate transformation for grid generation

$$\frac{\partial^2 y}{\partial \xi \partial \eta} = y_{i+1,j+1} - y_{i+1,j-1} + y_{i-1,j-1} - y_{i-1,j+1} \tag{D.10}$$

Two matrix equations are assembled with the boundary conditions, and an iterative scheme avoids solving a full matrix of equation (D.3) and (D.4). In addition, a over-relaxation factor can be used in order to accelerate the convergence.

The forcing functions, $P(\xi)$ and $Q(\eta)$, are related with grid stretching. These functions is used to contract and/or expand grid spaces. There are many ways to choose $P(\xi)$ and $Q(\eta)$, and the present computation adopts exponential functions with the form

$$P(\xi) = \sum_{i=1}^{n} p_i \; sgn(\xi - \xi_i) e^{-r_i|\xi - \xi_i|} \tag{D.11}$$

$$Q(\eta) = \sum_{j=1}^{m} q_j \; sgn(\eta - \eta_j) e^{-r_j|\eta - \eta_i|} \tag{D.12}$$

where $p_i$ and $q_j$ are attraction amplitudes and $r_i$ is decaying constant. If $p_i$ and $q_j$ are negative, the grids will be contracted. Otherwise the grids will be expanded.

Figure D-2 shows three different cases of $p_i$. In this case, $q_j$ is set to be zero. When $p_i$ is negative(left), the grids around body contract to body. If $p_i$=0, equation (D.1) becomes Laplace equation, and the generated grids are uniform. While, if $p_i$

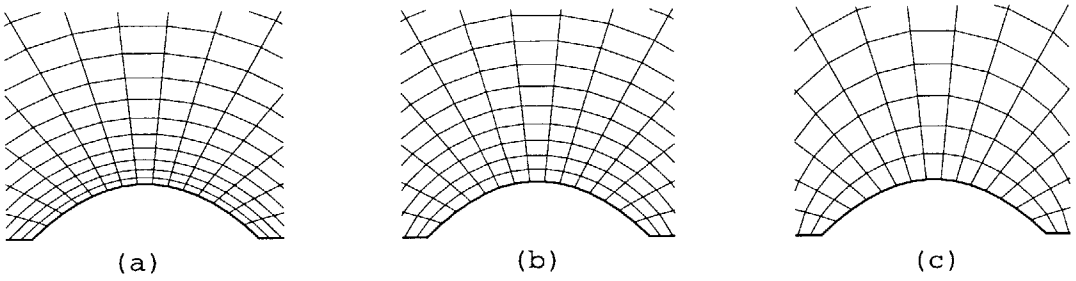


Figure D-2: The effect of forcing terms, (a) $P(\xi) < 0$, (b) $P(\xi) = 0$, (c) $P(\xi) > 0$

is positive(right), the grids expand. Detailed description about the effects of forcing term can be found in Ref.[74].

# Appendix E

# Artificial Wave Absorbing Zone

A proper treatment of the radiation condition is critical in the computation with a finite domain for a unbounded boundary value problem. In some field equation solvers, like FDM, in particular without free boundary, the zero velocity-gradient condition is efficient and effective. However, in the free-boundary value problems, it is not so simple to treat numerically the open boundary condition.

There are a few popular numerical techniques to treat the radiation condition of wave problem. Faltinsen [14], Dommermuth and Yue [12], Aarnesland [1] have matched the linear or nonlinear near-field velocity potential with the far-field asymptotic and/or linear solution. Vinje [77] used a periodic condition on the incoming and outgoing boundaries for the numerical simulation of ship motion. For Finite Element method, Bai [4] introduced a localized matching scheme.

One of the popular scheme is Orlanski's method. Since the Sommerfeld's radiation condition should be satisfied in the far field, this condition may be applied numerically at the truncated boundaries. Orlanski [59] applied this method for unbounded hyperbolic flows, and Chan [7], Yen and Hall [82] have applied this method for water wave problems. In particular, this method is effective on long waves.

Outgoing waves can be eliminated using an artificial damping zone applied in the present study. This concept is introduced by Israeli & Orszag [24] for a simple wave equation, and Baker, Meiron and Orszag [5] applied similar method to water wave

problems. Besides Cointe [10] proved its efficiency in the two-dimensional problems. Recently Clements [9] combined this method with Orlanski's method, taking both advantages.

Most of existing study for wave absorbing zone adopts the following kinematic free-surface boundary condition.

$$\frac{\partial \eta_1}{\partial t} - \frac{\partial \phi_1}{\partial z} + \mu_1(r)\eta_1 = 0. \tag{E.1}$$

This recovers equation (3.30) of Part II if $\mu_2$ is zero. When $\mu_2$ is zero and $\mu_1$ is a constant, the critical damping coefficient which doesn't allow oscillatory motion becomes

$$\mu_1 = 2\omega. \tag{E.2}$$

This can be easily proved using equation (3.32) of Part II. Faltinsen [15] used this concept to include damping effects in sloshing problem. In the sloshing problem with potential theory, transient effect doesn't decay if a proper damping mechanism is not supplied.

Nakos [51] added a $\mu_2$ term which was originally used by Israeli & Orszag [24]. The roll of $\mu_2$ is to keep wave characteristics, and it is sort of stiffness control. Therefore, if $\mu_1$ and $\mu_2$ are constant, there is no change of the linear dispersion relation inside of the zone. Furthermore it is possible to predict the decay rate of wave amplitude. Assume a single wave component, which can be written as $\eta(x,t) = \Re\{A(x)e^{i\omega t}\}$, we can find

$$\frac{\eta(x,t+T)}{\eta(x,t)} = e^{-\frac{\mu_1}{2}T} = e^{-\frac{\pi\mu_1}{\omega_o}} \tag{E.3}$$

where $T = \frac{2\pi}{\omega_o}$. Hence, after one oscillating, the wave amplitude decays exponentially proportional to $\frac{\pi\mu_1}{\omega_o}$. To keep the same damping effect for a higher frequency wave, the magnitude of $\mu_1$ should be linearly larger.

As described in Part II, it is not desirable to keep $\mu_1$ and $\mu_2$ as constants. In this case, the theoretical aspect is much more complicated and it is difficult to predict optimum or critical quantities of $\mu_1$ and $\mu_2$. However, based on computation experience, the similar damping mechanism is expected.

To maximize the efficiency of wave absorbing zone, a thorough study is necessary. There are several parameters which dictates the efficiency, the the size of zone, the magnitude of $\mu_1$, the variation of $\mu_1$ and $\mu_2$, so on. In order to observe the effects of these parameters, consider a two-dimensional pulsating pressure problem as shown in Figure E-1.

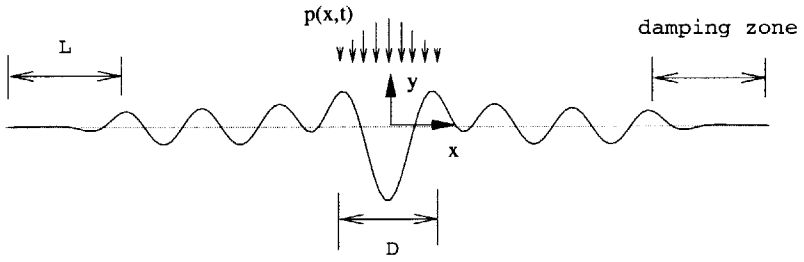


Figure E-1: A pulsating pressure patch problem

A pulsating pressure patch takes the form as follows:

$$p(x,t) = P_0 \cos^2(\frac{2\pi}{D}|x|) \sin(\omega_p t) \tag{E.4}$$

where $P_0, D, \omega_p$ are the amplitude, length, and frequency of the pressure patch. This two-dimensional problem was solved using source distribution method.

Figure E-2 shows the evolution of wave as time marches. Here, $\mu_o/\omega_p = 2\pi$ is applied and $\mu_1$ has a linear variation,

$$\mu_1 = 2\mu_o \frac{(x - x_o)}{L^2} \tag{E.5}$$

where $x_o$ is the coordinate where the wave absorbing zone begins. Israeli and Orszag used a polynomial form of n-th order for $\mu_1$ such that

$$\mu_1 = (n+1)\mu_o \frac{(r-x_o)^n}{L^{n+1}} \tag{E.6}$$

which satisfies $\int_{x_o}^{L} \mu_1 dx = \mu_o$. Therefore $\mu_o$ may be a good parameter to indicate the strength of the zone. In this case, $\mu_2$ is also included. Figure (a) and (b) are for $L/D = 1$ and 2, respectively. $L/D = 1$ means that the size of zone is one wavelength. From this figure, it is obvious that a linear variation seems not a proper choice.

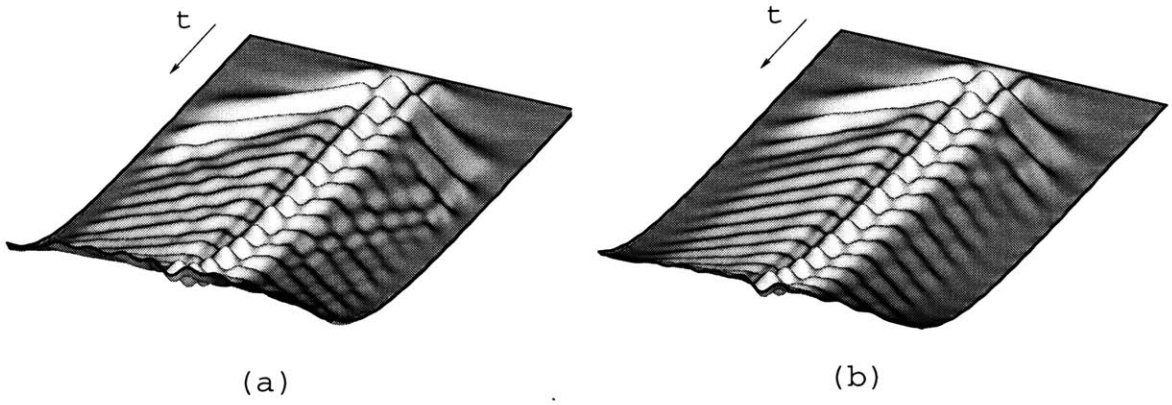


Figure E-2: Evolution of free surface near a pulsating pressure patch : $\mu_o/\omega_p = 2\pi$, linear variation, (a) $L/D = 1$, (b) $L/D = 2$

Figure E-3 shows the evolution of waves when $\mu_2$ is excluded, i.e. equation (E.1) is applied. A quadratic variation of $\mu_1$ is used. Bad results are obtained when the size of zone is short and the strength is weak. It is interesting that transient wave may pass the damping zone since it contains the low frequency components.

Figure E-4 shows the evolution of waves when both $\mu_1$ and $\mu_2$ are applied with a quadratic variation of $\mu_1$. It is obvious that this case provides the best results. When the variation of $\mu_1$ is more than quadratic, the damping effect is concentrated in too localized area, i.e. near the end of zone, and it is not desirable.

According these results, it is important to eliminate transient waves. The transient

waves are generated when a computation starts, and many components are mixed. Therefore, if the damping mechanism is weak, some long waves may not be eliminated so that they reflect on the edge of truncated boundary.

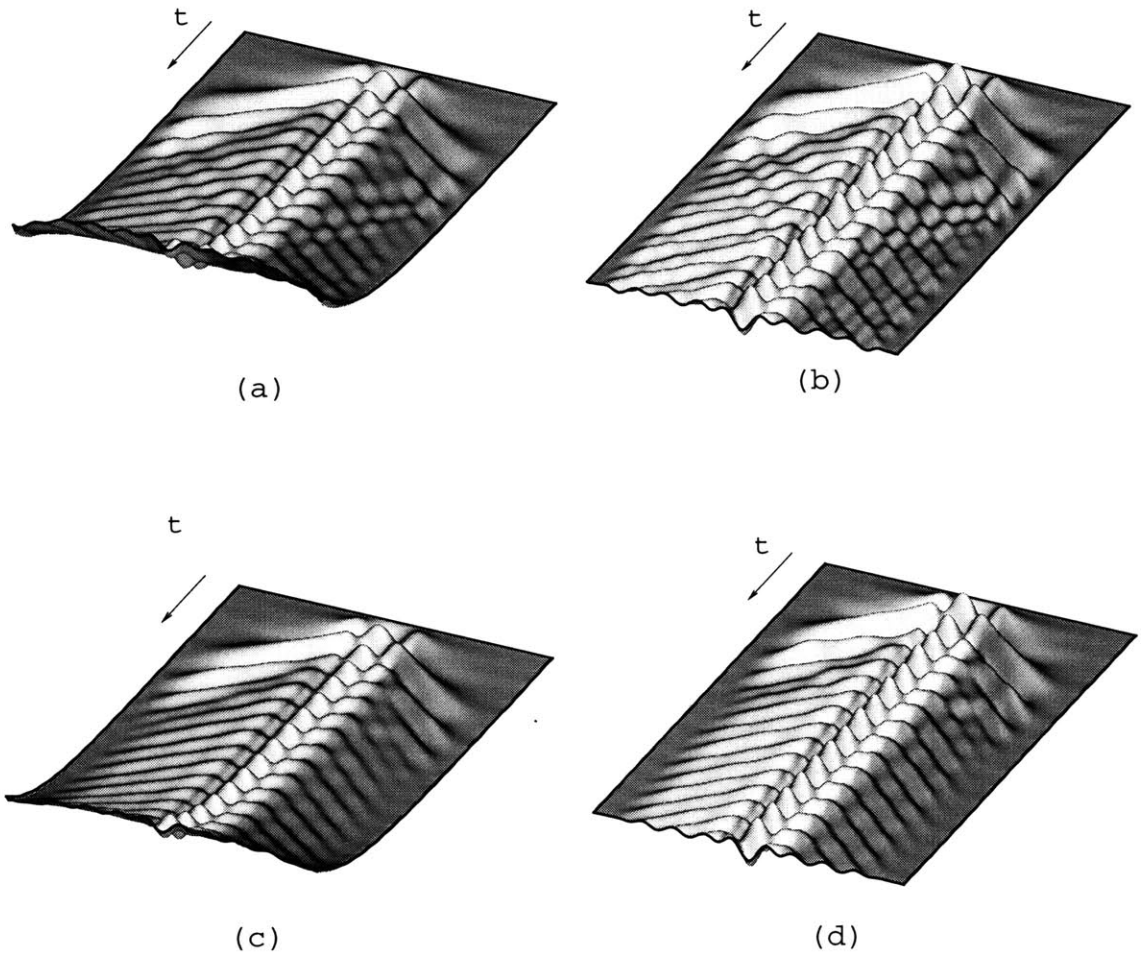


Figure E-3: Evolution of free surface near a pulsating pressure patch : quadratic variation without $\mu_2$ term (a) $\mu_o/\omega_p = 2\pi, L/D = 1$, (b) $\mu_o/\omega_p = 4\pi, L/D = 1$, (c) $\mu_o/\omega_p = 2\pi, L/D = 2$, (d) $\mu_o/\omega_p = 4\pi, L/D = 2$

In a three-dimensional problem, the sensitivity on the parameters is less significant than the two-dimensional case. It is because the velocity potential decays with the order of $1/\sqrt{r}$. According to the present study, the half of wavelength provides a reasonable result with stable time-marching. Figure E-5 is the results of an axis-

symmetric pulsating pressure patch problem. The same form with equation (E.4) is applied, but $x$ is replaced to $r$. According Figure E-5, it is obvious that the size and strength of wave absorbing zone is not as much important as two-dimensional case, but too weak and too short damping is not desirable.

When more than one component are mixed in the propagating waves, the wave absorbing zone has to be tuned to the longest wave. This is a disadvantage of the damping zone since the computation domain should be extended in order to include the zone. However, this method is simple to apply and quite effective, even for nonlinear problems.

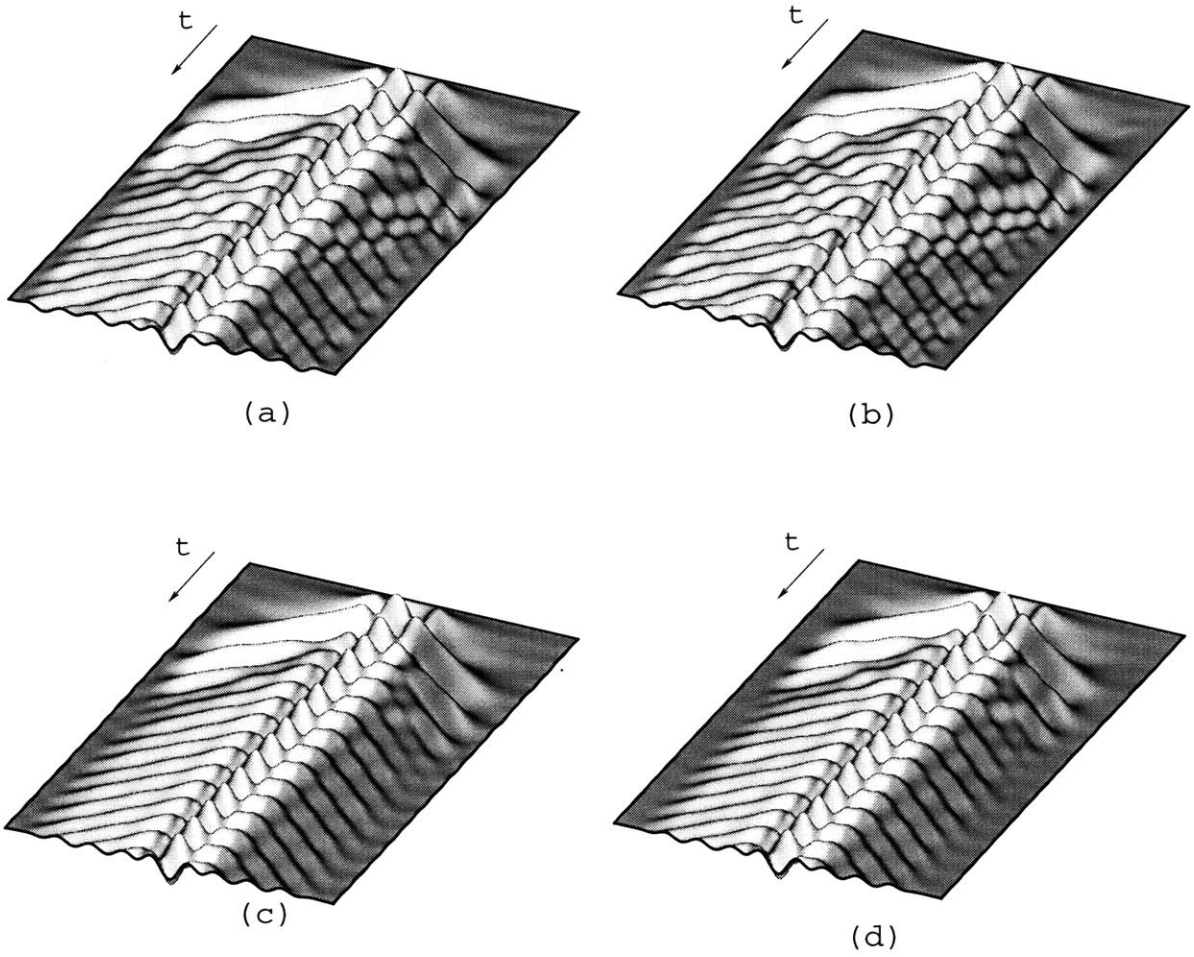


Figure E-4: Evolution of free surface near a pulsating pressure patch : quadratic variation, (a) $\mu_o/\omega_p = 2\pi, L/D = 1$, (b) $\mu_o/\omega_p = 4\pi, L/D = 1$, (c) $\mu_o/\omega_p = 2\pi, L/D = 2$, (d) $\mu_o/\omega_p = 4\pi, L/D = 2$

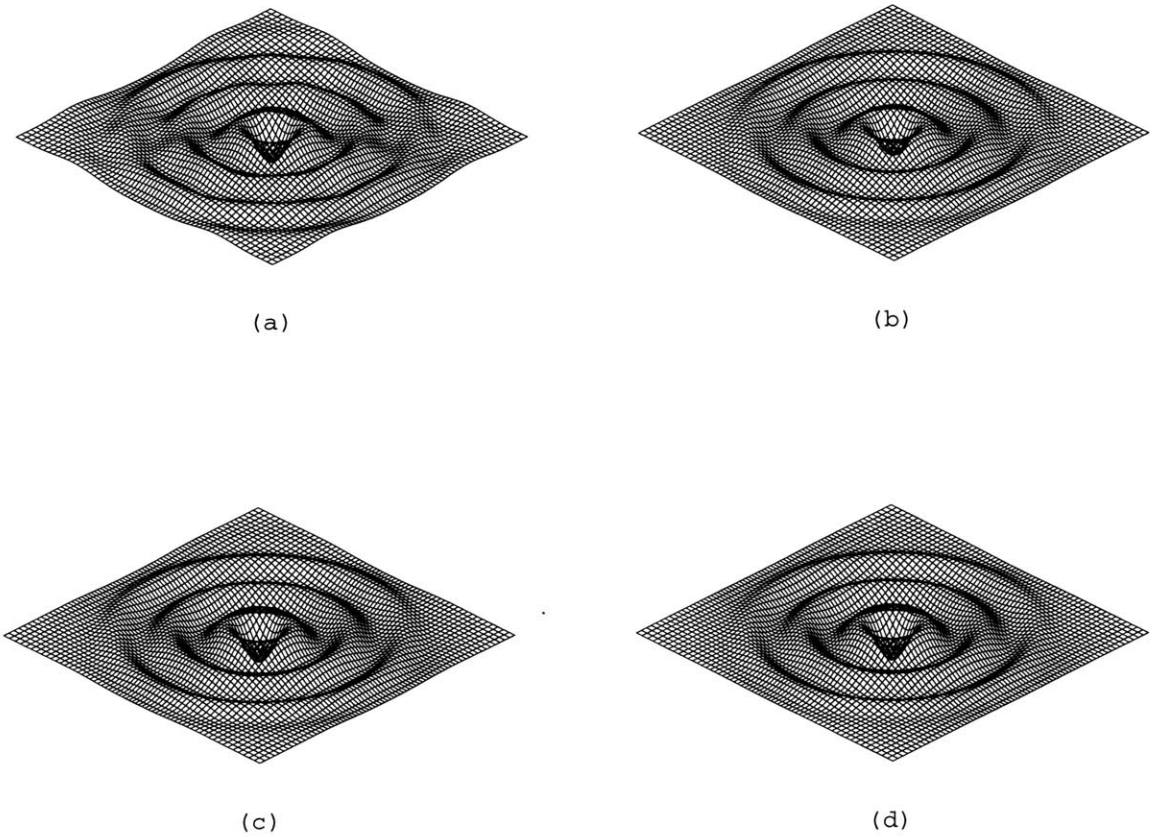


Figure E-5: Evolution of free surface near a pulsating pressure patch : quadratic variation with $\mu_2$ term (a) $\mu_o/\omega_p = 1, L/D = 0.5$, (b) $\mu_o/\omega_p = 2, L/D = 0.5$, (c) $\mu_o/\omega_p = 1, L/D = 1$, (d) $\mu_o/\omega_p = 2, L/D = 2$

# Appendix F

# Spatial Filters for Free-Surface Wave Problems

Filtering is one of the basics in signal processing. Since usually there is some noise in the measured signal, a proper filtering is essential. In a time domain approach for wave problem, it is difficult to avoid the generation of numerical noise, and a proper filter is required to eliminate this noise. As described in the stability analysis of Part II, the discrete group velocity of the possible shortest wave becomes zero. This shortest wave, i.e. two-grid-interval wave, doesn't disperse and grows up as time marches. Therefore, the purpose of filtering in water wave problem is the elimination of these saw-tooth waves.

Since a spatial filter is needed, it is not desirable to use as many points as a temporal filter in signal processing. In particular, near the edge of boundary, the available neighbor points are limited. When the number of neighbor points for the filter is not many, the smoothing effects cannot be ignored so that the repeated application can cause significant loss of energy. Usually the number of points is related with the order of filter, i.e. the order of error which decides the amount of a reason of energy loss/gain. Therefore it is required to find a filter which has minimum energy change and is expressed with a few points.

Shapiro [63] designed a linear filtering scheme in order to eliminate a saw-tooth

wave. He approximated a quantity of interest as a Fourier series, and suggested a higher order filter,

$$\bar{\eta}_j = c_0\eta_j + \sum_{k=1}^{K} c_k(\eta_{j-k} + \eta_{j+k}). \tag{F.1}$$

where $c_k$ is the coefficient which dictates the amount of smoothing and phase change. The decision of a proper value of $c_k$ is the key of filter design.

In order to predict the smoothing effect after filtering, express $\eta_j$ in terms of a sum of Fourier components, $A_n \cos\{n(x_j + \theta_n)\}$. Then, it is easy to find

$$R_K(n) \equiv \frac{\bar{A}_n}{A_n} = 1 - \sin^{2K}(\frac{n\Delta x}{2}) \tag{F.2}$$

where $R_k(n)$ is called the amplification factor or amplitude response function of k-th order. When $\lambda = 2\Delta x$, this filter eliminates the wave without phase change. The coefficients, $c_k$, are shown in Table F.1.

| K | C | $c_0/C$ | $c_1/C$ | $c_2/C$ | $c_3/C$ | $c_4/C$ | $c_5/C$ | $c_6/C$ | $c_7/C$ |
|---|---|---|---|---|---|---|---|---|---|
| 1 | $1/2^2$ | 2 | 1 | | | | | | |
| 2 | $1/2^4$ | 10 | 4 | -1 | | | | | |
| 3 | $1/2^6$ | 44 | 15 | -6 | 1 | | | | |
| 4 | $1/2^8$ | 186 | 56 | -28 | 8 | -1 | | | |
| 5 | $1/2^{10}$ | 772 | 210 | -120 | 45 | -10 | 1 | | |
| 6 | $1/2^{12}$ | 3172 | 792 | -495 | 220 | -66 | 12 | -1 | |
| 7 | $1/2^{14}$ | 12952 | 3003 | -2002 | 1001 | -364 | 91 | -14 | 1 |

Table F.1: The coefficients of Shapiro's filter

Longuet-Higgins and Cokelet [45] obtained $c_k$ using a different concept. They decomposed free surface profile into smoothing part and noise, and the second- or third-order polynomial was used to approximate the surface profile. They proposed two filtering formulae, which are very popular in the numerical simulation of water

wave,

$$\bar{\eta}_i = \frac{1}{16}(-\eta_{i-2} + 4\eta_{i-1} + 10\eta_i + 4\eta_{i+1} - \eta_{i+2}) \quad \text{(F.3)}$$

$$\bar{\eta}_i = \frac{1}{32}(-\eta_{i-3} + 9\eta_{i-1} + 16\eta_i + 9\eta_{i+1} - \eta_{i+3}) \quad \text{(F.4)}$$

whose the amplification factors are

$$R(n) = 1 - \sin^4(\pi\Delta x/\lambda_n) \quad \text{(F.5)}$$

$$R(n) = \frac{1}{16}\{-\cos(6\pi\Delta x/\lambda_n) + 9\cos(2\pi\Delta x/\lambda_n) + 8\} \quad \text{(F.6)}$$

The first filter of Longuet-Higgins and Cokelet is based on the second-order polynomial approximation and it is the same with Shapiro's filter of $K = 2$.

| n | 3-pt. | 5-pt.(A) | 5-pt.(B) | 7-pt.(A) | 7-pt.(B) |
|---|---|---|---|---|---|
| 2 | 0.0000 | 0.0000 | 0.0000 | 0.0000 | 0.0000 |
| 3 | 0.2500 | 0.4375 | 0.1562 | 0.5781 | 0.6100 |
| 4 | 0.5000 | 0.7500 | 0.5000 | 0.8750 | 0.9024 |
| 5 | 0.6545 | 0.8806 | 0.7244 | 0.9588 | 0.9751 |
| 6 | 0.7500 | 0.9375 | 0.8438 | 0.9844 | 0.9936 |
| 7 | 0.8117 | 0.9646 | 0.9070 | 0.9933 | 0.9986 |
| 8 | 0.8536 | 0.9786 | 0.9419 | 0.9969 | 0.9999 |
| 9 | 0.8830 | 0.9863 | 0.9621 | 0.9984 | 1.0002 |
| 10 | 0.9045 | 0.9909 | 0.9744 | 0.9991 | 1.0002 |
| 11 | 0.9206 | 0.9937 | 0.9821 | 0.9995 | 1.0001 |
| 12 | 0.9330 | 0.9955 | 0.9871 | 0.9997 | 1.0000 |
| 13 | 0.9427 | 0.9967 | 0.9905 | 0.9998 | 1.0000 |
| 14 | 0.9505 | 0.9975 | 0.9929 | 0.9999 | 0.9999 |
| 15 | 0.9568 | 0.9981 | 0.9946 | 0.9999 | 0.9999 |

Table F.2: The comparison of the amplification factors : Shapiro(3-pt.5-pt(A).7-pt.(A)), L.-H. & Cokelet(5-pt.(A),(B)), Nakos(7-pt.(B))

Recently Nakos [51] used a filter whose the amplification factor is written as equation(3.38) in Part II. This filter also eliminates the saw-tooth wave completely and produces less damping than other filters.

The side effect of filter is smoothing effect. The amount of smoothing depends on the choice of filter. For a single wave, the loss of energy is proportional to $\{1-R(n)\}^2$. Table F.2 compares the amplification factors for different filters. It is obvious that 3-point filter results in too much energy loss, while others are generally good.

# Bibliography


[1] Aanesland, V., 'A hybrid model for calculating wave-making resistance' *Proc. of 5th International Conference on Numerical Ship Hydrodynamics*, Hiroshima, 1989.

[2] Aranha, J.A.P., 'A formula for wave damping in the drift of a floating body', *Jour. of Fluid Mechanics*, Vol.272, 1994.

[3] Aranha, J.A.P., 'Slender body approximation for yaw velocity terms in the wave drift damping matrix', *Proc. International Workshop on Water Waves and Floating Bodies*, Marseille, 1997.

[4] Bai, K.J., Yeung, R.W., 'Numerical solutions to free-surface flow problems', *Proc. 10th Symposium in Naval Hydrodynamics*, 1981.

[5] Baker, G.H., Meiron, D.I., and Orszag, S.A., 'Application of a generalized vortex method to free surface flows',*Proc. 3rd International Conference on Numerical Ship Hydrodynamics*, Paris, 1981.

[6] Borresen, R., *The unified theory of ship motions in water of finite depth*, PhD.Thesis, The Norwaigian Institute of Technology, 1984.

[7] Chan, R.K.C., 'Finite difference simulation of the planar motion of a ship', *Proc. 2nd International Conference on Numerical Ship Hydrodynamics*, Berkeley, 1977.

[8] Chen, X.B., Molin, B., & Petitjean, F., 'Faster evaluation of resonant exciting loads on tension leg platforms', *Offshore Engineering*, Vol.8, 1992.

[9] Clements, A. Domgin, J.F., 'Wave absorption in a 2D numerical wave basin by coupling two methods', *Proc. International Workshop on Water Waves and Floating Bodies*, Oxford, 1995.

[10] Cointe, R., 'Nonlinear simulations of transient free surface flows', *5th International Conference on Numerical Ship Hydrodynamics*, Hiroshima, 1989.

[11] Dawson, C.W., 'A practical computer method for solving ship-wave problems', *Proc. 2nd International Conference on Numerical Ship Hydrodynamics*, Berkeley, 1977.

[12] Dommermuth D.G., Yue, D.K.P., 'The nonlinear three dimensional waves generated by a moving surface disturbance', *Proc. 17th Symp. Naval Hydrodynamics*, Hague, 1988.

[13] Emmerhoff, O.J., & Sclavounos, P.D., 'The slow-drift motion of arrays of vertical cylinders', *Jour. of Fluid Mechanics*, Vol.242, 1992.

[14] Faltinsen, O.M., 'Numerical solutions of transient nonlinear free surface motion outside or inside moving bodies', *Proc. 2nd International Conference on Numerical Ship Hydrodynamics*, Berkeley, 1977.

[15] Faltinsen, O.M., 'Numerical nonlinear method of sloshing in tanks with two dimensional flow', *Jour. of Ship Research*, Vol.22, 1978.

[16] Faltinsen, O.M., 'Sea loads on ships and offshore structures', *Cambridge Ocean Technology Series*, Cambridge University Press, 1990.

[17] Frank, W., *Oscillation of cylinders in or below the free surface of deep fluids*, N.S.R.D.C. Report No. 2375, Washington D.C., 1967.

[18] Grue, J. & Palm, E., 'The mean drift force and yaw moment on marine structures in waves and current', *Jour. of Fluid Mechanics*, Vol.250, 1993.

[19] FINNE, S., GRUE, J. 1997 'On the complete radiation-diffraction problem and wave-drift damping of marine bodies in the yaw mod of motion', submitted for publication, 1997.

[20] Gadd, G.E., 'A method of computing the flow and surface wave pattern around full forms', *Trans. Royal Asoc. Naval Arch.*, Vol.113, 1976.

[21] Hess, J.L., Smith, A.M.O., 'Calculation of nonlinear potential flow about arbitrary three-dimensional bodies', *Jour. of Ship Research*, Vol.8, 1964.

[22] Himeno, Y., *Prediction of Ship Roll Damping - State of the Art,* Univ. of Michigan, Report No.239, 1981.

[23] Huang, Y.F., *Nonlinear ship motions by a Rankine panel method*, PhD. Thesis, MIT, 1997.

[24] Israeli, M., and Orszag, S.A., 'Approximation of radiation boundary conditions', *Jour. of Computational Physics*, Vol.41, 1981.

[25] John, F., 'On the motion of floating bodies : II' *Comm. Pure Applied Mathematics*, Vol.3, 1950

[26] Kim, C.H., 'The influence of water depth on the midship bending moments of a ship moving in longitudinal regular head waves', *Jour. of the Ship Technology Society*, Vol.18, 1969

[27] Kim, M.H., 'The complete second-order diffraction solution for an axisymmetric body : Part 1. Monochromatic incident waves', *Jour. of Fluid Mechanics* Vol.200, 1989

[28] Kim, M.H., 'Second-harmonic vertical wave loads on arrays of deep-draft circular cylinder in multi-directional waves', *BOSS 92*, 1992

[29] Kim, S., Sclavounos, P.D., & Nielsen, F.G., 'Slow-drift response of moored platforms', *BOSS 97*, Hague, 1997.

[30] Kim, Y., Sclavounos, P.D., *Users manual of SWIM V4.0*, MIT Report, 1996.

[31] Kim, Y., Sclavounos, P.D., *Users manual of SWIM V4.1*, MIT Report, 1997.

[32] Kim, Y., Sclavounos, P.D., *Users manual of SWIM V4.2*, MIT Report, 1998.

[33] Kim, Y., Sclavounos, P.D., 'The computation of the second-order hydrodynamic forces on a slender ship in waves', *Proc. International Workshop on Water Waves and Floating Bodies*, Marseuille, 1997.

[34] Kim, Y., Sclavounos, P.D., 'A finite-depth unified theory for the linear and second-order problem of slender ships', submitted for the publication, 1998.

[35] Kim, Y., Kring, D.C., Sclavounos, P.D., 'Linear and nonlinear interactions of surface waves with bodies by a three-dimensional Rankine panel method', *Applied Ocean Research* Vol.19, 1997.

[36] Kim, Y., Sclavounos, P.D., 'A finite-depth unified theory for ship motion', *Proc. International Workshop on Water Waves and Floating Bodies*, Alphen a/d Rijn, 1998.

[37] Kim, Y., 'A study on the treatment of open boundary in the two-dimensional free-surface wave problems', *Trans. of the Society of Naval Architectures of Korea*, Vol.29, No.3, 1992.

[38] Kim Y., 'A study on the treatment of open boundary in the free-surface wave problems', *Proc. of 5th Asian Congress of Fluid Dynamics*, Taejon, 1992.

[39] Korsmeyer, F.T., Lee, C.H., Newman, J.N., & Sclavounos, P.D., 'The analysis of wave interactions with tension leg platforms', *OMAE conference*, 1988.

[40] Korvin-Kroukovsky, B.V., 'Investigation of ship motion in regular waves', *SNAME Transactions*, Vol.63, 1955.

[41] Kriebel, D.L., 'Nonlinear wave interaction with a vertical circular cylinder, Part II : wave run-up', *Ocean Engineering*, Vol.19, 1992.

[42] Kring, D.C., 'Time domain ship motions by a three-dimensional Rankine panel method', PhD Thesis, MIT, 1994.

[43] Lee, C.H., & Newman, 'Second-order wave effects on offshore structures', *BOSS 94*, Cambridge, 1994.

[44] Lighthill, M.J., *Fourier Analysis and Generalized Functions*, Cambridge University Press, Cambridge, 1958.

[45] Longuet-Higgins, M.S., and Cokelet, E.D., 'The deformation of steep surface waves on water - I. A numerical method of computation', *Proc. Royal Society, London*, Vol.350, 1976.

[46] Maruo, H., 'The drift of a ship floating on waves', *Jour. of Ship Research*, Vol.4, 1960.

[47] Mei, C.C., *The applied dynamics of ocean surface waves*, Wiley Press, New York, 1983.

[48] Nakos, D.E., and Sclavounos, P.D., 'Steady and unsteady ship wave patterns',*Jour. of Fluid Mechanics*, Vol.215, 1990.

[49] Nakos, D.E., *Ship wave patterns by a three dimensional Rankine panel method*, PhD Thesis, MIT, 1990.

[50] Nakos, D.E., Kring, D.C., and Sclavounos, P.D.,'Rankine panel methods for transient free surface flows', *Proc. 6th International Conference on Numerical Ship Hydrodynamics*, Iowa City, 1993.

[51] Nakos, D.E., 'Stability of transient gravity waves on a discrete free surface', submitted for publication, 1993.

[52] Newman, J.N., 'The drift force and moment on ship in waves'. *Jour. of Ship Research*, Vol.11, 1967

[53] Newman, J.N., *Marine hydrodynamics*, The MIT Press, Cambridge, 1977.

[54] Newman, J.N., 'The theory of ship motions', *Advances in Applied Mechanics*, Vol. 18, 1978.

[55] Newman, J.N., Sclavounos, P.D., 'The unified theory for ship motions'. *Proc. 13th Symposium Naval Hydrodynamics*, Tokyo, 1980.

[56] Newman, J.N., 'Distribution of sources and normal dipoles over a quadrilateral panel', *Jour. of Engineering Mathematics*, Vol.20., 1986.

[57] Newman, J.N., 'Second-harmonic wave diffraction at large depths', *Jour. of Fluid Mechanics*, Vol.213, 1990.

[58] Ogilvie, T.F., and Tuck, E.O., *A rational strip theory for ship motions, Part 1*, The University of Michigan, 1969.

[59] Orlanski, L., 'A simple boundary condition for unbounded hyperbolic flows', *Jour. of Computational Physics*, Vol.21, 1976

[60] Prudnikov, A.P., Brychkov, Y.A., Marichev, O.I., *Integrals and series, Vol.1 & 2*, Gordon and Breach Science Publishers, New York, 1986.

[61] Romate, J.E., 'The numerical simulation of nonlinear gravity waves in three dimensions using a higher panel method', PhD Thesis, University of Twente, 1989.

[62] Salvesen, N., Tuck, E.O., and Faltinsen, O., 'Ship motions and sea loads', *SNAME Transactions*, Vol.78, 1970.

[63] Shapiro, R., 'Linear filtering', *Jour. of Mathematics of Computation*, Vol.29, 1975.

[64] Sclavounos, P.D., 'The interaction of an incident wave field with a floating slender body at zero speed', *Proc. 3rd International Conference on Numerical Ship Hydrodynamics*, Paris, 1981.

[65] Sclavounos, P.D., 'The diffraction of free-surface waves by a slender ship', *Jour. of Ship Research*, Vol.28, 1984.

[66] Sclavounos, P.D., 'The unified slender-body theory: ship motions in waves', *Proc. 15th Symposium on Naval Hydrodynamics*, Germany, 1984.

[67] Sclavounos, P.D., 'Forward-speed vertical wave exciting forces on ships', *Jour. of Ship Research*, Vol.29, 1985.

[68] Sclavounos, P.D., *Users manual of NIIRID*, MIT Report, MIT, 1985.

[69] Sclavounos, P.D., and Nakos, D.E.,'Stability analysis of panel methods for free-surface flows with forward speed', *Proc. 17th Symposium on Naval Hydrodynamics*, Hague, 1988.

[70] Sclavounos, P.D., 'On the quadratic effect of random gravity waves on a vertical boundary', *Jour. of Fluid Mechanics*, Vol.242, 1992.

[71] Sclavounos, P.D., Chapter 4 : Computation of Wave Ship Interactions, *Advances in Marine Hydrodynamics*, Computational Mechanics Publications, Southampton, 1996.

[72] Sclavounos, P.D., Kring, D.C., Huang, Y., Mantzaris, D.A., Kim, S., & Kim, Y., 'Computational method as an advanced tool of ship hydrodynamic design', *Trans. SNAME*, The Soc. Naval Architecture and Marine Engineering, 1997.

[73] Sclavounos, P.D., Kim, S., Kim, Y., 'Nonlinear loads and response of ships and offshore platforms in deterministic and random waves', *ASCE Conference on Ocean Wave Kinematics*, Houston, 1998.

[74] Thompson, J.F., Warsi, Z.U.A., Mastin, C.W., *Numerical grid generation*, North-Holland, Elsevier Science Publishing Co., 1985.

[75] Tuck, E.O.,'Ship Motions in Shallow Water', *Jour. of Ship Research*, Vol.14, 1970.

[76] Vada, T., and Nakos, D.E., 'Time-marching schemes for ship motion simulations', *Proc. 8th International Workshop on Water Waves and Floating Bodies*, 1993.

[77] Vinje, T., Brevig, P., 'Nonlinear ship motion', *Proc. 3rd International Conference on Numerical Ship Hydrodynamics*, 1981.

[78] Press W.H. and et al, *Numerical Recipes*, Cambridge University Press, 1986

[79] Wehausen, J.V., Laitone, E.V., 'Surface waves', *Handbuch der Physik*, Vol.9, Springer-Verlag, Berlin, 1960.

[80] Xü, H., 'Numerical study of fully nonlinear water waves in three dimensions', PhD Thesis, MIT, 1992.

[81] Xue, M., 'Three-dimensional fully-nonlinear simulations of waves and wave body interactions', PhD Thesis, MIT, 1997.

[82] Yen, S.M., Hall, D.R., 'Implementation of open boundary conditions for nonlinear free-surface wave problems', *Proc. 3rd International Conference on Numerical Ship Hydrodynamics*, Paris, 1981.